universität wien

DISSERTATION

Titel der Dissertation

Creating and manipulating higher-dimensional entangled photonic quantum systems using integrated optics

Verfasser

Christoph Schäff M.A. in Physics

angestrebter akademischer Grad

Doktor der Naturwissenschaften (Dr.rer.nat.)

Wien, 2014

Studienkennzahl lt. Studienblatt:	A 791 411
Dissertationsgebiet lt. Studienblatt:	Physik
Betreuerin / Betreuer:	Prof. Dr. Anton Zeilinger

Abstract

A general photonic platform for experiments in higher-dimensional entangled quantum systems is presented. A universal approach is taken aiming towards a high degree of flexibility. In contrast to a specific design corresponding to a particular experiment a system of great generality is obtained opening the possibility for a variety of different quantum optical experiments. The crucial concepts and steps leading to the final system are presented and discussed: a fully fiber-integrated source creating higher-dimensional path-encoded entangled photons is constructed and tested. In parallel, the so-called general Multiport, a complex device capable of realizing any unitary transformation in any dimension, has been realized using an on-chip integrated approach. Novel methods of testing and characterizing the Multiport have been developed and implemented. Furthermore, the process of interfacing and controlling the source and Multiport is presented, eventually leading to complete automated control of the full quantum system. By changing different parameters of the setup the created entangled state is adjusted while the Multiport allows for any desired local unitary transformation. For the first time, an entangled two qutrits system of this type in a $3 \times 3 = 9$ dimensional Hilbert space is implemented. Different experiments are realized, i.a. a full scan of the entangled two qutrit correlation space is performed and found in agreement with theoretic predictions. Extensions of the setup are presented and the path towards higher-dimensional systems is further developed offering great potential for future experiments pursuing the same direction.

Contents

Acknowledgment

This work would not have been possible without the help and support of many people around me. It is my pleasure to acknowledge those people.

Foremost, I would like to thank my supervisor Anton Zeilinger for all the guidance and support throughout the years. I am particularly grateful for all the trust and opportunities I received along the way. You always kept a good balance between freedom and advice creating an encouraging and fruitful working environment, probably unique to this group. It was a great pleasure working with you.

Especially, I would like to thank all the members of our group with which I have worked together closely:
Sven Ramelow for all his help and guidance especially at the beginning of this work
Robert Polster for all the work and effort he put into the experiment, many parts of the setup are due to his contribution
Robert Fickler and Bernhard Wittmann for a rememberable time at Documenta and beyond
Radek Lapkievicz for all the fruitful discussions
and all the other members of our subgroup including Mario Krenn, Marcin Wisniac, Pheize Li, and Javier Chesterking for all their help, support and friendship.

My special thank is further extended to all the countless members and students of our Institute and within the Vienna Center for Quantum Science and Technology. I am grateful for the former and current administrative staff of the IQOQI, ÖAW and the faculty research group Quantum optics, Quantum nanophysics and Quantum information for all their hard work behind the scenes.
My appreciation to the technical staff for all the good work over the years.

Furthermore, I would like to acknowledge the CoQuS and EMALI programs along with everyone involved, the Institute for Quantum Optics and Quantum Information (IQOQI), the Austrian Academy of Sciences (ÖAW), and the University of Vienna.

This work was supported by the ERC (Advanced Grant QIT4QAD, 227844), and the Austrian Science Fund FWF within the SFB F40 (FoQuS) and W1210-2 (CoQuS).

I owe my deepest gratitude to my family and friends for all their help throughout my life.
My loving thanks to Friederike for her patience and trust all over the years.
Finally, I would like to express my gratitude to everyone I did not mention and who supported me during the completion of this work.

It was a great time which I will always be grateful for,

Christoph
Vienna, Dec. 2013

1 Introduction

The goal of this thesis is to explore higher-dimensional entangled quantum systems and to build a platform enabling a certain degree of flexibility of the setup. Higher-dimensional quantum systems are expected to show a variety of novel interesting effects. They exhibit higher-order non-local perfect correlations [1], are more robust against noise [2, 3], offer a higher degree of security in quantum communication protocols [2], are related to the problem of finding a complete set of mutually unbiased bases [4], and allow more efficient quantum information tasks [5] compared to qubits. In fact, they allow quantum secret sharing schemes and error-correction codes which cannot be realized with qubits [6]. Furthermore, it has been shown that a quantum computer using a higher-dimensional system, a quNit, as the basic unit is more efficient and requires less resources than a quantum computer based on qubits [7, 6]. In addition, understanding higher-dimensional quantum states most likely leads to a deeper understanding of the fundamentals of quantum physics.

Notwithstanding the opportunities lying in higher-dimensional quantum systems, little is actually known about Hilbert spaces which are not composed out of multiple qubits [8]. Thus, one goal is to develop a setup allowing for experiments on higher-dimensional systems.

At the beginning of the project there was the opportunity technology of integrated optics has already been developed for centuries but has only started to step into the interest of the quantum optics community. In 1997 a paper by M. Zukowski, A. Zeilinger, and M. Horne [1] has been published presenting a novel device, the Multiport. Due to its construction the Multiport allows an experimenter to realize any unitary transformation of any dimension while at the same time it is only composted out of beam splitters and phase shifters, arguably, one of the two most basic devices in the area of photonics. However, since then, little advancements towards a general Multiport have been made. Today, integrated optics offers the technology. The so-called Multiport would be of great appeal to an experimenter. Instead of building different independent setups for a particular set of experiments one could use the Multiport (once constructed) to realize different experiments at an instance by simply changing its parameters.

The Multiport itself has some interesting applications: it can be used for creating entangled multi-photon states such as the W-state [9] [10] and other entangled states [11–13], it allows for observation of GHZ-type paradoxes of N maximally entangled N-dimensional quantum systems [14], the circuit could be used for the factorization of numbers [15], serves as an analyzer of the input state of light [16], or as a simulator of quantum logic though the use of the Multiport's linear optics [17].

Naturally, a general approach is more complicated compared to building a specific non-general experiment. On the other hand a general platform has more to offer due to its flexibility. Designing, building, controlling, and characterizing the Multiport will be one of the main objectives.

The Multiport is not the only bottle neck towards a platform realizing an N-dimensional quantum system. There are two main steps: building a source producing entangled quNits, and building the $N \times N$ Multiport realizing any desired unitary transformation.

Often a photonic qubit is encoded in the polarization degree of freedom forming a 2-dimensional system extendible only through the use of additional degrees of freedom or multiple particles

[18, 19]. Here, path-encoding is chosen. A photon in a superposition of N spatially separated paths is a realization of a quNit system. In some ways, the path is the most basic degree of freedom since most optical experiments, to some extent, involve the separation and combination of spatial quantum physical objects or modes. Furthermore, path-encoding intrinsically offers perfect separation and extinction of two modes via spatial separation. Additionally, the two basic operations, a beam splitter and a phase shifter are well-known standard optical devices ubiquitously used in free-space and integrated optics. There is no direct physical constraint of some type in the number of paths. Light guiding waveguides are the basic component of any integrated photonic circuit making path-encoding compatible with most state-of-the-art integrated photonic devices. Thus, path-encoding will be the starting point.
Initially, a source for entangled quNits needs to be constructed. It should be compatible with the integrated Multiport and thereby with path-encoding. The source should be scaling with the dimension at an experimentally controllable scale and ultimately allow for on-chip integration as well. Often, an entangled photon pair is produced via the process of spontaneous parametric down conversion (SPDC) . As already suggested by Zukowski, Zeilinger, and Horne [1] one could utilize the momentum entanglement inherent to the two SPDC photons for an in principle infinite dimensional space. However, I view this as an indirect realization of a quNit system, where a detour over the geometric shapes of the SPDC process is used. Here, a different approach will be taken. An N-dimensional quantum system, a quNit, is characterized by the superposition of N modes. Extending the scheme to N separated SPDC events in a superposition can lead to two entangled quNits. Ultimately, every quNit will enter a Multiport performing any local unitary transformation onto each quNit of the entangled two quNit N^2-dimensional system.
Part of the same authors of the initial Multiport proposal [1, 20] have realized a non-general Multiport. An in-fiber 3×3 fused coupler of fixed splitting ratio has been utilized for observing two photon interference by Weihs, Reck, Weinfurter, and Zeilinger [21]. Using the same type of coupler a three-path Mach-Zehnder interferometer has been constructed and the corresponding three-path interference pattern has been observed using a classic, continuous wave laser [22]. Eventually, the same interference pattern will become visible in the coincidence detection signal of a two photon entangled qutrit state. However, the origin is a non-classical effect: only in coincidence detection will a pattern be visible.
Although qutrit-qutrit correlations have already been partly observed, a complete characterization is missing. The reason mainly is due to missing control of the system. A fixed ratio splitter represents only a particular unitary transformation and thus only corresponds to one element of $SU(N)$. An integrated realization of the general Multiport covering the full $SU(N)$ space has not been demonstrated.

The thesis is organized as follows:
First, in **section 2** the necessary **theoretic background** will be reviewed.
Then, the main experimental part is divided into three parts:
(1) Section 3 presents the first part of **building a source for a higher- dimensional system**. An in-fiber path-encoded entangled qubit source was built and its feasibility was tested.

The results have been published [23]. The extension of the source towards higher-dimensions will then be described.
(2) Section 4 will deal with the **development of the Multiport**. Due to the complexity of the device an on-chip integrated realization has been chosen. The experimental performance of the fundamental devices will be presented in section 4.4 and is to be published. In order to couple light in and out of the integrated Multiport circuit a fully featured coupling setup has been developed in section 4.5.
(3) Section 5 deals with the process of interfacing the source and the Multiport after they have been individually characterized.
Eventually, **section 6** will present **results** obtained from the fully assembled experiment. The performance of more complex functions of the Multiport will be estimated. Measurements within all possible (two qubit) subspaces are described and eventually, the full entangled qutrit space will be measured and analyzed.
Section 7 will give an **outlook** of this particular experiment and will also present **proposals** towards future experiments. Especially, a newly developed Multiport realization seems promising towards higher dimensions due to its close similarity to current commercial integrated devices.
Eventually, **Section (9)** will **conclude** the work.

2 Theory

In the following important theoretical tools and methods necessary within this thesis will be reviewed. The basic details of the fundamentals of quantum optics and quantum information may be found in numerous introductory text books [24–27].

2.1 Preliminary

An N-dimensional quantum system (NQS) in Dirac notation is given by an vector Ψ in Hilbert space H_N

$$|\Psi_N\rangle = \sum_{i=1}^{N} |i\rangle \,. \tag{2.1}$$

$|i\rangle$ can be realized as any degree of freedom of the system. Here, path-encoding will exclusively be used meaning a NQS is realized by a particle being in a superposition of N spatially separated paths. Two particles in mode i and j will be written as $|i\rangle \otimes |j\rangle = |ij\rangle$. An NQS $|\Psi_N\rangle$ thus can be realized by a particle in a superposition of N spatially separated modes. Generally, this will be illustrated by N horizontal lines. The input of the state will always be to the left, will evolve though some path-encoded system and eventually exit to the right.

Every pure state Ψ of a composite bipartite quantum system $H = H_A \otimes H_B$ can be expressed by a sum of biorthogonal terms:

$$|\Psi\rangle = \sum_{i,j=1}^{n} \alpha_i |u_i\rangle \otimes |v_j\rangle \tag{2.2}$$

with $|u_i\rangle \in H_A$, $|v_j\rangle \in H_B$, $n = min\left(\dim(H_A), \dim(H_A)\right)$ and $\alpha_i \in R$ with $\sum |\alpha_i|^2 = 1$. Eq. 2.2 is commonly referred to as the Schmidt decomposition. The number of real non-zero values α_i is called the Schmidt rank S [28]. The Schmidt rank S serves as a measure of entanglement [24] and corresponds to the entanglement dimensionality. Thus, for $S = 1$ the state $|\Psi\rangle$ is a product state, for $S > 1$ the state is entangled.

The Schmidt rank is preserved under a unitary transformation on the subsystem A or B alone [24]. The Schmidt number cannot be increased under local unitary transformations and classic communication [24]. Due to the construction of the experiment, the following entangled bipartite state will be of main interest:

$$|\Psi_N\rangle \propto \sum_{i=1}^{N} |ii\rangle \,. \tag{2.3}$$

The Schmidt rank is $S = N$. Thus, the entanglement of a state $|\Psi_N\rangle$ of the form given in eq. 2.3 is of dimension N. In the experiment this state will enter two Multiports performing a local unitary transformation U on each subsystem of the bipartite state. This cannot increase the Schmidt rank.

N will always either refer to the dimension of a single particle system (eq. 2.1) or an entangled bipartite system of the form of eq. 2.3.

2.2 Unitary transformation

A state in Hilbert space $\langle\Psi|$ is transformed by an unitary operator U: $\langle\Psi| \longrightarrow \langle\Psi'| = \langle\Psi|U$.
The special unitary group $SU(N)$ in dimension N is the subset of $N \times N$ unitary matrices with determinant one. The generators λ_i with $i = 1...N^2 - 1$ of $SU(N)$ are traceless hermitian operators and form the basis of $SU(N)$. Any point in $SU(N)$ can be described by the $N^2 - 1$ dimensional real parameter unit vector $\vec{v}$ as a linear combination $\sum_{i=0}^{N^2-1} v_i\lambda_i$ with λ_0 being the diagonal 1 matrix. The generators of $SU(2)$ are (up to a factor) connected to the Pauli matrices σ_i. In dimension 3 to the 8 Gell-Mann matrices.
Sometimes it is convenient to displaying a unitary transformation as a $N \times N$ unitary matrix with N^2 complex or $2N^2$ real parameters. Because it will be helpful for understanding the functioning of the Multiport in future sections the number of free parameters can quickly be derived. Taking dimension $N = 3$, for example, consider a 3×3 unitary matrix with $3 \times 3 = 9$ complex entries or 18 real entries.

$$\begin{pmatrix} a & b & c \\ d & e & f \\ g & h & i \end{pmatrix} \xrightarrow{(1)} \begin{pmatrix} a & b & c \\ b^\dagger & e & f \\ c^\dagger & f^\dagger & i \end{pmatrix} \xrightarrow{(2)} \begin{pmatrix} |a| & b & c \\ b^\dagger & |e| & f \\ c^\dagger & f^\dagger & |i| \end{pmatrix}$$

Not all $N^2 = 9$ entries are free parameters. Unitarity $U = U^\dagger$ requires $d = b^\dagger, g = c^\dagger, h = f^\dagger$ and therefore the number of free parameters is reduced by 6 (Step 1). Any unitary matrix can be rewritten with only real entries on its diagonal resulting in -3 free parameters (Step 2). Finally, normalization eliminates one further parameter -1. Therefore, an 3×3 unitary matrix has $18 - 6 - 3 - 1 = 8$ free parameters.

2.2.1 Generalized Pauli matrices in dimension N

For later reference the Pauli (σ) and Gell-Mann (λ) matrices will be explicitly stated:

$$\sigma_1 = \begin{pmatrix} 0 & 1 \\ 1 & 0 \end{pmatrix}, \sigma_2 = \begin{pmatrix} 0 & -i \\ i & 0 \end{pmatrix}, \sigma_3 = \begin{pmatrix} 1 & 0 \\ 0 & -1 \end{pmatrix}$$

$$\lambda_1 = \begin{pmatrix} 0 & 1 & 0 \\ 1 & 0 & 0 \\ 0 & 0 & 0 \end{pmatrix}, \lambda_2 = \begin{pmatrix} 0 & -i & 0 \\ i & 0 & 0 \\ 0 & 0 & 0 \end{pmatrix}, \lambda_3 = \begin{pmatrix} 1 & 0 & 0 \\ 0 & -1 & 0 \\ 0 & 0 & 0 \end{pmatrix}$$

$$\lambda_4 = \begin{pmatrix} 0 & 0 & 1 \\ 0 & 0 & 0 \\ 1 & 0 & 0 \end{pmatrix}, \lambda_5 = \begin{pmatrix} 0 & 0 & -i \\ 0 & 0 & 0 \\ i & 0 & 0 \end{pmatrix}$$

$$\lambda_6 = \begin{pmatrix} 0 & 0 & 0 \\ 0 & 0 & 1 \\ 0 & 1 & 0 \end{pmatrix}, \lambda_7 = \begin{pmatrix} 0 & 0 & 0 \\ 0 & 0 & -i \\ 0 & i & 0 \end{pmatrix}, \lambda_8 = \begin{pmatrix} 1 & 0 & 0 \\ 0 & 1 & 0 \\ 0 & 0 & -2 \end{pmatrix}. \tag{2.4}$$

When comparing the Pauli and Gell-Mann matrices of eq. 2.4 it becomes apparent that $\lambda_1, \lambda_4, \lambda_6$ ($\lambda_2, \lambda_5, \lambda_7$) are simply the two dimensional Pauli matrices σ_1 (σ_2) extended to all subspaces (i, j) in dimension 3: $(1, 2), (1, 3), (2, 3)$. Similar for $\sigma_3 \to \lambda_3$ in the subspace of the first two dimensions $(1, 2)$. λ_8 includes both $\sigma_3^{(1,3)}$ in the subspace $(1, 3)$ and $\sigma_3^{(2,3)}$ in $(2, 3)$.

The example shows what was stated by Thew, White, and Munro [29]: the generators λ_i of $SU(N)$ in any dimension can be easily constructed from elementary matrices:

$$1 \leq k < j < N :$$

$$\lambda_{(j-1)^2+2(k-1)} = \sigma_1^{(j,k)} \;,\; \lambda_{(j-1)^2+2k-1} = \sigma_2^{(j,k)}$$

$$\lambda_{j^2-1} = \sqrt{\frac{2}{j(j-1)}} = \sum_{i=1}^{j-1} e_i^i - (j-1)e_j^j, \tag{2.5}$$

with e_i^j being a $N \times N$ matrix with only the $(i, j)th$ entry being non-zero and equal to one. The last equation can be seen as a sum of σ_3 matrices from different subspaces.

2.2.2 Decomposition of a unitary transformation in any dimension

As seen in the previous section a unitary transformation in any dimension can be described by a linear combination of the generators λ_i. Any generator λ_i on the other hand can be constructed from combinations of Pauli matrices in a two dimensional subspaces (plus output phases, λ_8 in eq. 2.5). Therefore, assuming there exists an experimental device capable of realizing any transformation in $SU(2)$ it follows that any transformation in $SU(N)$ can be realized by simply combining multiple $SU(2)$ transformations. Every single $SU(2)$ transformation defines the interaction between two modes of the N-level quantum system. For a three dimensional quantum system three subspaces ((1,2),(1,3),(2,3)) exist and therefore $3 \times SU(2)$ rotations are required. Introducing an additional fourth mode requires another 3 qubit interactions leading to a four dimensional system. In general a transformation of an N level quantum system thus requires

$$1 + 2 + ... + (N-1) = \frac{1}{2}N(N-1) \tag{2.6}$$

$SU(2)$ transformations.

Assuming a certain unitary transformation U the decomposition into $SU(2)$ components is a straight forward iterative process similar to Gaussian elimination. The method has been developed and presented in detail by M. Reck et al. [30, 20] and will be applied regularly throughout this thesis.

2.2.3 Parametrization of the unitary group

Spengler, Huber, and Hiesmayr [31] have shown any element of $SU(N)$ can be parametrized in any dimension following a general scheme:

$$U_N = \prod_{m=1}^{N-1} \left[\prod_{n=m+1}^{d} e^{iZ_{m,n}\lambda_{n,m}} e^{iY_{m,n}\lambda_{m,n}} \right] \prod_{l=1}^{N-1} \left(e^{iZ_{l,d}\lambda_{l,l}} \right), \tag{2.7}$$

using the $d^2 - 1$ real parameter $\lambda_{m,n} \in [0, \pi]$ for $m > n$, $\lambda_{m,n} \in [0, \pi/2]$ for $m < n$ and $\lambda_{m,n} \in [0, 2\pi]$ for $m = n$ [31].

$$Z_{m,n} = |m\rangle\langle m| - |n\rangle\langle n|$$

is the generalized diagonal Pauli Matrix σ_z acting on different subspaces (m, n).

$$Y_{m,n} = -i\,|m\rangle\langle n| + i\,|m\rangle\langle n|$$

is an anti-diagonal operator similar to σ_y. The last product $\prod_{l=1}^{N-1}\left(e^{iZ_{l,d}\lambda_{l,l}}\right)$ represents output phase shifts which are not of interest in this particular application.
Following [31], using eq. 2.7 an infinitesimal volume element dU of the unitary group $SU(N)$ can be assigned:

$$dU_N = \frac{1}{N_N}\prod_{m=1}^{N-1}\prod_{n=m+1}^{N} Sin(\lambda_{m,n})Cos^{2(n-m)-1}(\lambda_{m,n})\prod_{k,l=1}^{d}\lambda_{k,l}, \tag{2.8}$$

with N_N being a normalizing factor such that $\int_{SU(N)} dU = 1$.
Some explicit results are [31]:

$$\begin{aligned} U_2 =& e^{iZ_{1,2}\lambda 2,1} e^{iY_{1,2}\lambda_{1,2}} e^{iZ_{1,2}\lambda 1,1} \\ dU_2 =& \frac{1}{\pi^2} Sin(\lambda_{1,2})Cos(\lambda_{1,2})d\lambda_{1,2}d\lambda_{2,1}d\lambda_{1,1}. \end{aligned} \tag{2.9}$$

$$\begin{aligned} U_3 =& e^{iZ_{1,2}\lambda 2,1} e^{iY_{1,2}\lambda_{1,2}} e^{iZ_{1,3}\lambda 3,1} e^{iY_{1,3}\lambda_{1,3}} e^{iZ_{2,3}\lambda 3,2} e^{iY_{2,3}\lambda_{2,3}} e^{iZ_{1,3}\lambda 1,1} e^{iZ_{2,3}\lambda 2,2} \\ dU_3 =& \frac{4}{\pi^5} Sin(\lambda_{1,2})Cos(\lambda_{1,2})Sin(\lambda_{1,3})Cos^3(\lambda_{1,3})Sin(\lambda_{2,3})Cos(\lambda_{2,3})\cdot \\ & \cdot d\lambda_{1,2}d\lambda_{2,1}d\lambda_{1,3}d\lambda_{3,1}d\lambda_{2,3}d\lambda_{3,2}d\lambda_{1,1}d\lambda_{2,2}. \end{aligned} \tag{2.10}$$

$$\begin{aligned} U_4 =& e^{iZ_{1,2}\lambda 1,2} e^{iY_{1,2}\lambda_{1,2}} e^{iZ_{1,3}\lambda 3,1} e^{iY_{1,3}\lambda_{1,3}} e^{iZ_{1,4}\lambda 4,1} e^{iY_{1,4}\lambda_{1,4}} \\ & e^{iZ_{2,3}\lambda 3,2} e^{iY_{2,3}\lambda_{2,3}} e^{iZ_{2,4}\lambda 4,2} e^{iY_{2,4}\lambda_{2,4}} e^{iZ_{3,4}\lambda 4,3} e^{iY_{3,4}\lambda_{3,4}} \\ & e^{iZ_{1,4}\lambda 1,1} e^{iZ_{2,4}\lambda 2,2} e^{iZ_{3,4}\lambda 3,3} \\ dU_4 =& \frac{96}{\pi^9} Sin(\lambda_{1,2})Cos(\lambda_{1,2})Sin(\lambda_{1,3})Cos^3(\lambda_{1,3})Sin(\lambda_{1,4})Cos^5(\lambda_{1,4}) \\ & Sin(\lambda_{2,3})Cos(\lambda_{2,3})Sin(\lambda_{2,4})Cos^3(\lambda_{2,4})Sin(\lambda_{3,4})Cos(\lambda_{3,4}) \\ & d\lambda_{1,2}d\lambda_{2,1}d\lambda_{1,3}d\lambda_{3,1}d\lambda_{1,4}d\lambda_{4,1}d\lambda_{2,3}d\lambda_{3,2} \\ & d\lambda_{2,4}d\lambda_{4,2}d\lambda_{3,4}d\lambda_{4,3}d\lambda_{1,1}d\lambda_{2,2}.d\lambda_{3,3} \end{aligned} \tag{2.11}$$

As mentioned above, $Z_{m,n}$ and $Y_{m,n}$ are similar to the Pauli matrices. The terms $e^{iZ_{m,n}\lambda_{m,n}}$ create a relative phase shift between the two modes (m,n) while every term of the form $e^{iY_{m,n}\lambda_{m,n}}$

creates a rotation between two modes. This can be seen by a Taylor expansion leading to:

$$e^{iZ\lambda} = 1 + i(Z\lambda) - \frac{(Z\lambda)^2}{2!} - i\frac{(Z\lambda)^3}{3!} + \frac{(Z\lambda)^4}{4!} + ...$$

$$\Rightarrow e^{iZ\lambda} = \sum_k (-1)^k \frac{(Z\lambda)^{2k}}{(2k)!} + i \sum_k (-1)^k \frac{(Z\lambda)^{2k+1}}{(2k+1)!}$$

and similar for Y (the indices (m,n) are ignored for simplicity). It can be easily verified that

$$Z^{2k} = \mathbf{1} \ , \ Z^{2k+1} = Z \ , \ \forall k \in Z$$

$$Y^{2k} = \mathbf{1} \ , \ Y^{2k+1} = Y \ , \ \forall k \in Z$$

with $\mathbf{1}$ being the diagonal one matrix. Using this relation it follows that

$$\begin{aligned} e^{iZ\lambda} &= \begin{pmatrix} 1 & 0 \\ 0 & 1 \end{pmatrix} \textstyle\sum_k \displaystyle (-1)^k \frac{(\lambda)^{2k}}{(2k)!} + i \begin{pmatrix} 1 & 0 \\ 0 & -1 \end{pmatrix} \sum_k (-1)^k \frac{(\lambda)^{2k+1}}{(2k+1)!} \\ \Rightarrow e^{iZ\lambda} &= \begin{pmatrix} e^{i\lambda} & 0 \\ 0 & e^{-i\lambda} \end{pmatrix} \end{aligned} \tag{2.12}$$

meaning Z is producing a relative phase shift of λ between the two modes (m,n). Similarly for Y one obtains

$$\begin{aligned} e^{iY\lambda} &= \begin{pmatrix} 0 & -i \\ i & 0 \end{pmatrix} \textstyle\sum_k (-1)^k \frac{(\lambda)^{2k}}{(2k)!} \displaystyle + i \begin{pmatrix} i & 0 \\ 0 & i \end{pmatrix} \sum_k (-1)^k \frac{(\lambda)^{2k+1}}{(2k+1)!} \\ \Rightarrow e^{iY\lambda} &= i \begin{pmatrix} Sin(\lambda) & Cos(\lambda) \\ Cos(\lambda) & Sin(\lambda) \end{pmatrix} \end{aligned} \tag{2.13}$$

being a rotation around the modes (m,n). Such a rotation can be realized using a beam splitter of arbitrary reflectivity ($r = 0...1$) presented in the following section (2.3.1).

2.3 The Multiport

The Multiport (MP) is an N input N output device capable of realizing any unitary transformation in $SU(N)$. As shown in section 2.2.2 one way of realizing a unitary transformation is by using multiple $SU(2)$ transformations as the basic unit.

2.3.1 The 2×2 Multiport: the beam splitter

A beam splitter is a 2×2 unitary device:

$$\begin{pmatrix} r & t\ e^{i\varphi} \\ t\ e^{-i\varphi} & r\ e^{i\delta} \end{pmatrix}, r^2 + t^2 = 1$$

with $r, t = 0..1$ and $\varphi, \delta = 0..2\pi$. φ and δ are defined by the experimental realization of the beam splitter (for example phase shift when reflected from surfaces of different refractive indices, etc...), r^2 (t^2) is the reflectivity (transitivity). In the case of a geometrically symmetric beam splitter the latter equation becomes

$$\begin{pmatrix} r & it \\ it & r \end{pmatrix}, r^2 + t^2 = 1. \tag{2.14}$$

Adding a phase shift of π to both input modes as well as to one of the output modes eq. 2.14 then becomes equivalent to eq. 2.13 with $r = Sin(\lambda)$. According to Eq.2.9, by adding a variable input phase to the beam splitter of eq. 2.14 the $SU(2)$ space is completely parametrized (up to an irrelevant output phase).
Therefore, a beam splitter of reflectivity r^2 with one input phase φ is a 2×2 Multiport (up to an output phase) capable of realizing any 2×2 unitary transformation. The reason for ignoring the output phase(s) (eq.2.7) is that light exiting the Multiport is directly guided to detectors. The modes therefore do not interact anymore and thus the phase is irrelevant. Generally, beam splitters have a fixed splitting ratio defined by the construction.
In order to change the reflectivity a Mach-Zehnder interferometer can be utilized.

2.3.2 Tunable beam splitter - Mach-Zehnder interferometer

A Mach-Zehnder Interferometer (MZI) consists out of two 50/50 beam splitter with phases in each arm resulting in a transformation equivalent to

$$\frac{1}{\sqrt{2}}\begin{pmatrix} 1 & i \\ -i & 1 \end{pmatrix}\begin{pmatrix} e^{i\varphi_1} & 0 \\ 0 & e^{i\varphi_2} \end{pmatrix}\frac{1}{\sqrt{2}}\begin{pmatrix} 1 & i \\ -i & 1 \end{pmatrix}$$

$$= ... \propto e^{i\frac{\Sigma}{2}}\begin{pmatrix} Cos(\Delta) & -iSin(\Delta) \\ -iSin(\Delta) & Cos(\Delta) \end{pmatrix}, \tag{2.15}$$

Σ (Δ) represents half the sum (difference) of the inner phases $\frac{1}{2}(\varphi_1 \pm \varphi_2)$. The term $e^{i\frac{\Sigma}{2}}$ is a global phase shift and is not of relevance in a two-mode system. Δ defines the reflectivity of the MZI. Σ and Δ are linearly independent combinations of φ_1 and φ_2. Thus, the reflectivity and global phase shift can be set independently. Together with one input and one output phase the MZI can realize any qubit unitary transformation (eq. 2.9). As will be discussed in the next section, due to experimental flaws the MZI might not be able to reach a reflectivity of $r = 0$ or $r = 1$ and thus not every region of the full $SU(2)$ space is reachable.

2.3.3 Characterization of a non-perfect Mach-Zehnder-Interferometer

Assuming a Mach-Zehnder-Interferometer (MZI) depicted in fig. 2.1 composed out of two beam splitter with an unbalanced reflectivity of $\sqrt{1/2+\Delta}$ $\left(\sqrt{1/2+\delta}\right)$, a phase shift φ, and an absorber $\Lambda = 10^{-\lambda/10dB}$ in on arm , the unitary transformation is given by:

$$U_{MZI}(\varphi) = \begin{pmatrix} \sqrt{\frac{1}{2}-\Delta} & -i\sqrt{\frac{1}{2}+\Delta} \\ i\sqrt{\frac{1}{2}+\Delta} & \sqrt{\frac{1}{2}-\Delta} \end{pmatrix}\begin{pmatrix} \Lambda e^{i\varphi} & 0 \\ 0 & 1 \end{pmatrix}\begin{pmatrix} \sqrt{\frac{1}{2}-\delta} & -i\sqrt{\frac{1}{2}+\delta} \\ i\sqrt{\frac{1}{2}+\delta} & \sqrt{\frac{1}{2}-\delta} \end{pmatrix}. \tag{2.16}$$

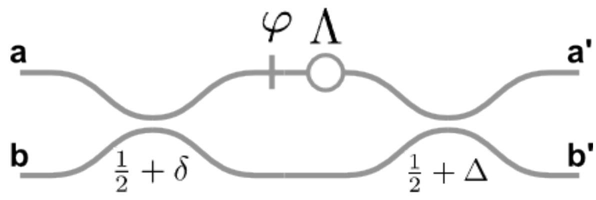

Figure 2.1: Illustration of a Mach-Zehnder-Interferometer (MZI).

During a characterization light is inserted at one input, the phase $\varphi = 0...2\pi$ is scanned and the intensity signal is recorded. The maximum (minimum) amplitudes will be given by

$$A^{max/min} = U_{MZI}^{\varphi=0/\varphi=\pi} \frac{1}{\sqrt{2}} \begin{pmatrix} 1 \\ 0 \end{pmatrix} = \sqrt{2} \begin{pmatrix} \delta^+\Delta^+ \mp \Lambda\delta^-\Delta^- \\ \delta^+\Delta^- \pm \Lambda\delta^-\Delta^+ \end{pmatrix} \tag{2.17}$$

with $\Delta^\pm = \sqrt{1/2 \pm \Delta}$ and $\delta^\pm = \sqrt{1/2 \pm \delta}$. As can be seen in the example of fig. 2.2 and from eq. 2.17 measuring the reflective output $(a \to a')$ of the MZI supplies the true maximum of the fringe and therefore enables one to calculate the true visibility. At the transmissive output $(a \to b')$ a reduced maximum would be measured which does not greatly contribute to a reduction of visibility. Therefore, always the reflective output arm relative to the input is measured during a characterization. Every MZI will be characterized in this way in the experimental sections.

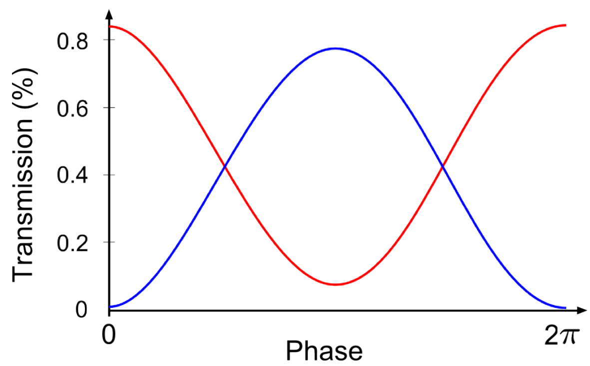

Figure 2.2: Example of the reflective (red) and transmissive (blue) output of the MZI depicted in fig. 2.1 using eq. 2.17 with $\Delta = +0.1, \delta = -0.1, \Lambda = 0.8$.. The reflectivity (red line) can be set to any value between $R = 100...9.3\%$. Calculating the visibility directly from the measured maximum/minimum of one fringe alone, one obtains: 97.6% and 83.0%.

The visibility V of each MZI is an important property of the Multiport. Every MZI should be set to any reflectivity $R = 0...1$. If the MZI is not perfect meaning $V \neq 1$ it becomes impossible to reach every R. In fig. 2.2, for example, the reflectivity can only be set in the range of $R = 100...9.3\%$. Following eq. 2.17 the visibility measured at both outputs when inserting light into mode 1 becomes

$$\begin{aligned} V_1 = & \tfrac{2\Lambda\delta^-\Delta^-\delta^+\Delta^+}{(\Lambda\delta^-\Delta^-)^2+(\delta^+\Delta^+)^2}, \\ V_2 = & \tfrac{2\Lambda\delta^-\Delta^+\delta^+\Delta^-}{(\Lambda\delta^-\Delta^+)^2+(\delta^+\Delta^-)^2}. \end{aligned} \tag{2.18}$$

The visibility depends on the three parameter $(\Lambda, \delta, \Delta)$. Given the experimentally measured visibilities V_1 and V_2, without further assumptions on the parameters, Λ, δ, and Δ cannot be calculated unambiguously. However, later it will become apparent that within first approximation zero loss difference $\Lambda = 0$ can be assumed between the two arms of the MZI. This allows to derive the other parameters δ, Δ. This will be of use for the characterization of the experimental realization of the Multiport.

Each MZI together with a phase shifter represents a qubit Multiport while a combination of three such qubit rotations allow any unitary transformation in SU(3). Using the parametrization of eq. 2.7 (section 2.2.3) one can estimate the coverage (cov_N) of an imperfect Multiport (imperfect MZI) using eq. 2.9 and eq. 2.10:

$$cov_N = \frac{\overbrace{\int\int ... \int}^{\lambda_{i,j}=min_{i,j}...max_{i,j}} \quad d\lambda_{1,2} d\lambda_{2,1} ... d\lambda_{N,N}}{\int_{SU(N)} dU_N} \tag{2.19}$$

with $max_{i,j}$ and $min_{i,j}$ representing the limits of each parameter due to a non-perfect extinction ratio of a MZI or phase shifter. A value of $cov_2 = 1$ would mean every unitary transformation can be reached, whereas $cov_2 < 1$ limits the reachable unitary space due to imperfections of the MZI and therefore limited range of the tunable parameters such as the reflectivity.

2.3.4 Trivial phase shift equivalences

For later reference two simple conversions of phases in a path-encoded system will be presented. As illustrated in the upper sketch of fig. 2.3 a phase φ acting onto mode $|0\rangle$ of a 2-dimensional quantum system $e^{i\varphi}|0\rangle + |1\rangle$ is equivalent to the negated phase $-\varphi$ acting on the other mode (up to a global phase of φ).

The lower sketch (fig. 2.3) shows how this equivalence together with the global phase $\Sigma/2$ (Eq.2.15) of a MZI can be used to eliminate φ (up to a global phase).

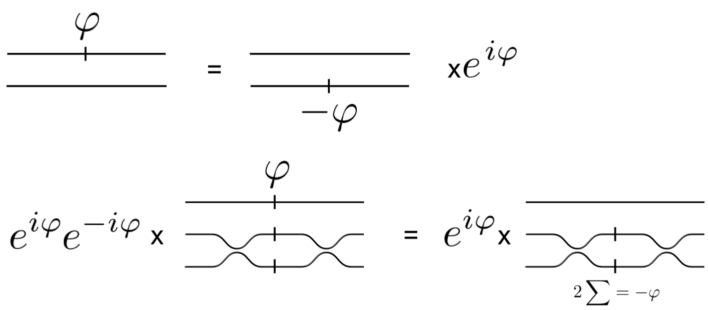

Figure 2.3: Two sketches of two trivially equivalent path-encoded circuits. **Top:** The quantum system $|0\rangle + |1\rangle$ enters from the left. Phase shifters φ are marked by small dashes crossing the wires. The term x$e^{-i\varphi}$ represents a global phase acting on both modes. **Bottom:** details see text (section 2.3.4). Beam splitters are displayed by the bend areas where two waveguides come close to each other.

The term "global phase" has been used already. The correct definition of a global phase is a phase which acts on the full quantum state $e^{i\varphi}|\psi\rangle$. However, later, especially in the case of the Multiport the input and output phases will also sometimes be called "global" depending on the context although they do not fulfill the above definition. The output phase of the Multiport directly enters the detectors. No interference takes place anymore. Therefore, any output phase is irrelevant to the system similar to a global phase. The reason for calling the input phase a global phase will become apparent in the later sections and is related to the fact that the system has to be characterized by the PID in any case eliminating thereby any initial phase offset.
Fig. 2.4 in section 2.3.5 shows a particular circuit which will be considered in the next section. Here the blue lines in the top image of Fig. 2.4 are only of interest. As will become important later, note, that a phase added to all modes along any blue line is a global phase and does not change the system.

2.3.5 The general $N \times N$ Multiport

In order to build the $N \times N$ Multiport we now have to combine $1/2N(N-1)$ (eq. 2.6) units consisting of one beam splitter and a phase shifter (eq. 2.15). Section 2.2.1 or reference [20] give the recipe on how to combine them. Two examples are illustrated in fig. 2.4.

2.3.6 The Multiport as a projective measurement

Inserting a detector into the i-th mode of an NQS result in a projective measurement

$$\langle P_j\rangle = |i\rangle\langle i|\,.$$

Inserting the quantum state into a Multiport displaying a certain unitary transformation U followed by detection leads to:

$$|i\rangle\langle i| \xrightarrow{U} U^\dagger |i\rangle\langle i| U = \langle P_i'\rangle\,. \tag{2.20}$$

Hence, any projective measurement $\langle P_i'\rangle$ can be realized using a Multiport choosing the appropriate transformation U and detection.

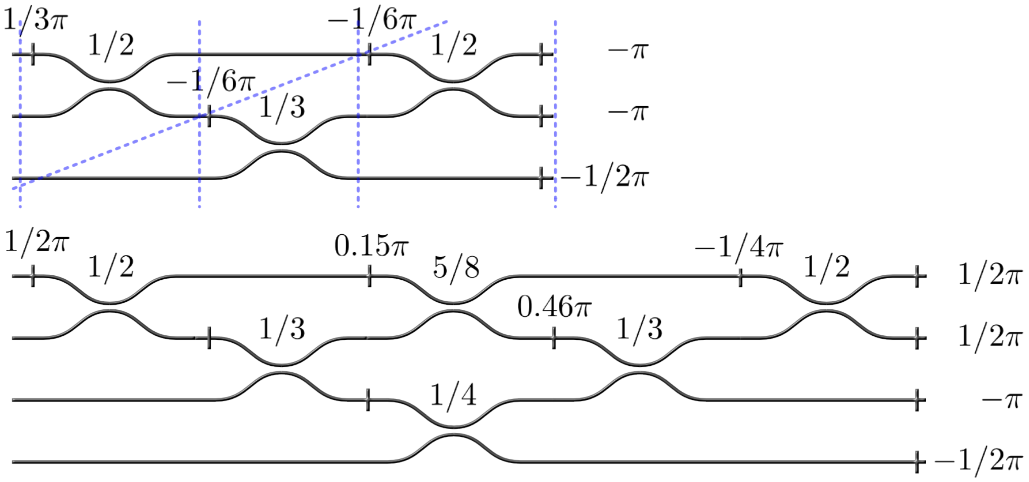

Figure 2.4: Examples of the general Multiport consisting of combinations of qubit operations realized using beam splitters and phase shifters. Beam splitters are illustrated by two bend modes close to each other. Dashes represent phase shifters. Upper image: 3×3 MP. Lower image: 4×4 MP. Changing each beam splitter reflectivity and phase any unitary transformation can be realized. Numerical values correspond to phases and reflectivities of a particular Multiport setting called Bellport (see section 2.3.7). The blue lines are used in section 2.3.4.

2.3.7 Bellport and Fast Fourier Transformation

Because of its importance a special kind of Multiport is presented: the symmetric Multiport or Bellport (BP). The $N = 3$ ($N = 4$) Bellport is called Tritter (Quarter) . All elements are the N-th roots of unity meaning the (i,j)-th matrix element is of the form

$$BP_{ij} = \frac{1}{\sqrt{d}}\, e^{2\pi i/N(i-1)(j-1)} = \frac{1}{\sqrt{d}}\, \omega^{(i-1)(j-1)}. \tag{2.21}$$

The above transformation can be viewed as the direct Fourier transformation of the direct basis. The BP is a higher-dimensional beam splitter, if one particle enters at one input, there is an $1/N$ probability of finding it at any output. The BP can be generalized to any dimension. Later, it will be important for observing perfect correlations between entangled particles. The Bellport is shown in fig. 2.4. Some explicit Bellports are:

$$\begin{aligned}
BP_{N=2} &= \quad \tfrac{1}{\sqrt{2}} \begin{pmatrix} 1 & 1 \\ 1 & -1 \end{pmatrix} \\
BP_{N=3} &= \quad \tfrac{1}{\sqrt{2}} \begin{pmatrix} 1 & 1 & 1 \\ 1 & e^{i2\pi/3} & e^{i4\pi/3} \\ 1 & e^{i4\pi/3} & e^{i2\pi/3} \end{pmatrix} \\
BP_{N=4,\phi=\pi/2} &= \quad \tfrac{1}{\sqrt{2}} \begin{pmatrix} 1 & 1 & 1 & 1 \\ 1 & e^{i\phi} & -1 & e^{i\phi} \\ 1 & -1 & 1 & -1 \\ 1 & -e^{i\phi} & -1 & e^{i\phi} \end{pmatrix}_{\phi=\pi/2} \quad .
\end{aligned} \tag{2.22}$$

The elements of $BP_{N=4,\phi}$ are equal to roots of unity for $\phi = \pi/2$. The reason for introducing the extra phase will be explained later.

2.3.8 Fast Fourier Transformation

As discovered by Zukowski, Zeilinger, and Horne [1], the 4×4 BP has a simpler realization compared to the general version. Clearly, compared to the $1/2N(N-1)$ qubit operations required for a general Multiport (eq. 2.6), the number of elements can be greatly reduced when only a specific unitary such as the Bellport (BP) is desired.
In the case of the BP the simplification is connected to an algorithm performing a discrete fast Fourier transformation (FFT). More precisely, the analog of the Tuckey-Cooley FFT algorithm is applied [32]. This analogy has not been mentioned in the initial publication by Zukowski, Zeilinger, and Horne [1] introducing the Bellport. This algorithm can be applied for any composite dimension $N = N_1 N_2$ recursively reducing an N-dimensional FFT into smaller direct FTs of dimension N_1 and N_2.[1] Clearly, for high dimensions such simplification methods become important. However, already the 8×8 Bellport has only 12 beam splitters compared to the general 8×8 Multiport with 28 beam splitters. Therefore, if only the special case of a Bellport is required the above algorithm offers a great reduction in complexity.
Further information on the reduction of the complexity of the Multiport can be found in [33] [34] [35].

2.4 quNit tomography

Quantum tomography is the process of reconstructing the quantum state in an experiment via a series of measurements. The density matrix ρ of two particles is of the form

$$\rho = \sum_{i,j=0}^{N^2-1} v_{ij} \lambda_i \otimes \lambda_j \tag{2.23}$$

with $\{\lambda_i \otimes \lambda_j\}$ being any set spanning $SU(N) \otimes SU(N)$ and $v_{ij} = \langle \lambda_i \otimes \lambda_j \rangle$ [29, 36]. For pure states $\sum_{i=1}^{3} \lambda_i^2 = 1$ while for mixed states $0 \leq \sum_{i=1}^{3} \lambda_i^2 < 1$. Therefore, measuring all $N^4 - 1$ expectation values v_{ij} will allow to reconstruct the full density matrix ρ via eq. 2.23. The Multiport will be used to display the unitary transformation. Optimally, any operator of the set $\{\lambda_i \otimes \lambda_j\}$ should have the least overlap with any other operator of the set. The higher the overlap the more precise the measurements have to be to distinguish them. Here, the Pauli matrices come into play (section 2.2.1). In fact, the Pauli matrices represent a maximal set of MUBs (see section 2.7). Therefore, assuming an unknown N-level input state ρ, the Multiport together with detectors at the output (following eq. 2.20) can be used to measure each of the $N^4 - 1$ expectation values v_{ij} to reconstruct the density matrix.
In an experiment a finite number n of photons is detected. Assuming Poissonian statistics there is an uncertainty on the order of $\sqrt{n}$ in the measured counts and following eq. 2.23 leads to a region of possible states in Hilbert space. Every quantum state within this area in Hilbert

[1] In the language of discrete Fourier transformations the basic operation is a "butterfly operations" followed by a "twiddl factor" (a complex root of unity) being the analog of a beam splitter and phase shifter.

space would predict the counted photons within its given uncertainty. Directly reconstructing the density matrix (eq. 2.23) therefore might result in a unphysical density matrix where, for example, $\sum_{i=1}^{3} \lambda_i^2 > 1$.
In order to obtain a real density matrix a numerical search has to be performed due to the complexity of the problem. Here, the method is closely following the work of Altepeter, Jeffrey, and Kwiat [36] and all details can be found within. The space of possible density matrices ρ is parametrized using the set of real parameters $(t_1, t_2, ..., t_{2n})$ of a lower triangular matrix

$$T\left(t_1, t_2, ..., t_{2n}\right).$$

The density matrix is given via the expression

$$\rho_{(t1,t2,...,t_{2n})} = \frac{1}{Norm} \left(T^*\right)^\dagger \; T.$$

The $\nu - th$ measurement setting $M_{\nu,r}$ is defined by the unitary transformation U_ν and coincidence detection at detector pair r:

$$M_{\nu,r} = U_\nu^{*T} \left|r\right\rangle \left\langle r\right| U_\nu.$$

A certain density matrix $\rho_{(t_1,t_2,...,t_{2n})}$ then will predict $n_{\nu,r}$ counts at detector pair r and setting ν given by

$$n_{\nu,r} = Tr\left[M_{\nu,r}\rho_{(t_1,t_2,...,t_{2n})}\right].$$

The goal is to find the set $(t_1, t_2, ..., t_{2n})$ predicting the actually measured counts $n'_{\nu,r}$ with the highest probability. The problem is equivalent to finding a set $(t1, t2, ..., t_{2n})$ with the lowest residue of the relative difference between predicted $n_{\nu,r}$ and measured counts $n'_{\nu,r}$:

$$\min\left\{L_{(t_1,t_2,...,t_{2n})}\right\} = \sum_{\nu,r} \frac{\left(n'_{\nu,r} - n_{\nu,r}\right)^2}{2n'_{\nu,r}}.$$

$L_{(t1,t2,...,t_{2n})}$ is called the likelihood function (LHF). A numerical search will lead to the minimum of the LHF and allows to calculate the density function of maximum likelihood (MLF): $\rho^{MLE}_{(t1,t2,...,t_{2n})}$.
A program has been developed allowing for the reconstruction of the density matrix of two entangled quNits for any dimension N via a maximum likelihood estimation and using any sequence of measurements. The program will be applied in later sections.

2.5 Perfect correlations

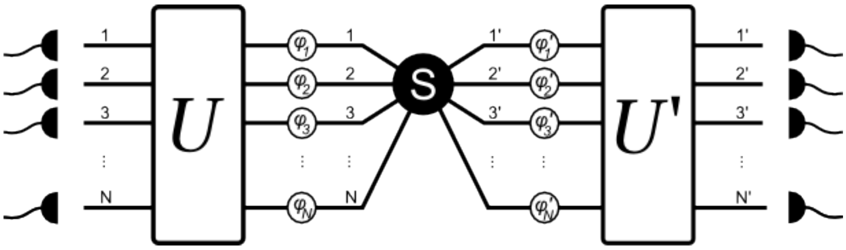

Figure 2.5

Quantum correlations of a composite (entangled) quantum system are types of correlations which cannot be consistently described by inherent local classical properties of the subsystem. Such correlations cannot be created by separated local transformations on each subsystem [37]. They are the key feature distinguishing "classic" from quantum correlations. The term perfect correlation will refer to a quantum correlation of probability one. Fig. 2.5 shows a theoretical setup consisting of a source producing an entangled state of equal amplitudes and phases

$$\psi_N = \frac{1}{\sqrt{N}} \sum_{i=1}^{N} |ii\rangle \, .$$

Each quNit of the state ψ enters after passing phase shifters (φ_i) a Bellport (eq. 2.21) followed by detection at outputs $i = 1...N$ and $j = 1'...N'$. The probability of detecting a photon pair at detectors (i, j) can be calculated to

$$P_{i,j} = |\langle i,j|\, U \otimes U' \,|\psi\rangle|^2 = \frac{1}{N} \left| \sum_{i=1}^{N} e^{i(\varphi_i + \varphi_i')} \omega^{(i-1)(i+j)} \right|^2 , \tag{2.24}$$

where $\omega = e^{i2\pi/N}$ is the N-th root of unity of the Bellport $U_{i,j} = \langle i|\, U \,|j\rangle = 1/\sqrt{N}\omega^{(i-1)(j-1)}$ [1]. Due to symmetry reasons of the Bellport ($\omega^{i+N} = \omega^i$) the above equation (eq. 2.24) has N groups containing N probabilities $P_{i,j}$ of equal value within a group as derived by Zukowski, Zeilinger, and Horne [1] for $N = 3$:

$$\begin{aligned} P_{1,1} &= P_{2,3} = P_{3,2} \\ P_{1,2} &= P_{2,1} = P_{3,3} \\ P_{1,3} &= P_{2,2} = P_{3,1} \end{aligned} \tag{2.25}$$

A perfect correlation occurs if $P_{1,k} = 1/3$. Then $P_{1,k} = 1/3 \;\forall\; i + j = 1 + k \; mod \; N$ and therefore all other probabilities vanish: $P_{1,l}^{k \neq l} = 0$. Thus, given certain phase settings, a detector on the side of quNit A is connected with probability one to a detector registering quNit B on the other side. As mentioned above, there are N groups of equal probability. Therefore, there are $N = 3$ different possible settings of perfect correlations between both detection sides. The settings differ by different phase shifts φ_i:

$$\begin{aligned}\varphi_1 + \varphi_1' &= \varphi_2 + \varphi_2' = \varphi_3 + \varphi_3' \\ \varphi_1 + \varphi_1' &= \varphi_2 + \varphi_2' + \omega^1 = \varphi_3 + \varphi_3' + \omega^2 \\ \varphi_1 + \varphi_1' &= \varphi_2 + \varphi_2' + \omega^2 = \varphi_3 + \varphi_3' + \omega^1. \end{aligned} \tag{2.26}$$

The three different phase settings are displayed in fig. 2.6 and for a $N = 4$ dimensional system in fig. 2.7. The perfect correlation pictures can be uniquely labeled (see fig. 2.7): each detector on each side is assigned a power of $\omega = e^{i2\pi/4} = i$. The product of the value of pairs of detectors perfectly correlated allows to uniquely label each of the 4 correlation pictures (see caption of fig. 2.7). The same is possible for every dimension N. Interestingly, if $\phi \neq \pi/2$ (eq. 2.22) for one of the Bellports such a labeling is not possible suggesting a special role of the Bellport [1].

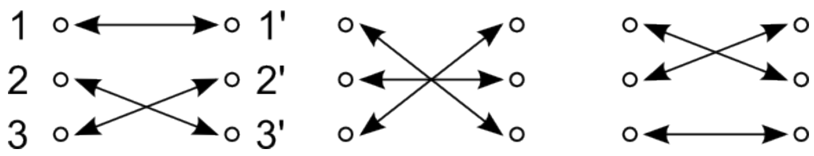

Figure 2.6: Perfect correlations between detectors on each side detecting on of the two entangled quTrits.

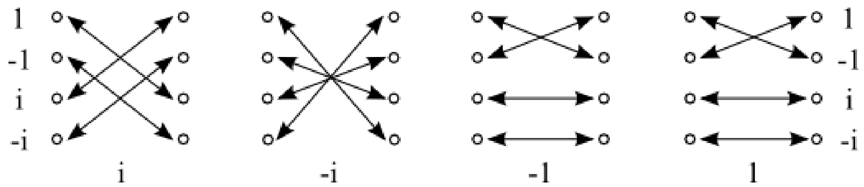

Figure 2.7: Perfect correlations between detectors on each side detecting on of the two entangled ququarts ($N = 4$). The values correspond to a labeling procedure: each detector on each side is assigned a power of $\omega = e^{i2\pi/4}$: $(1, -1, i, -i)$. The product of the assigned values of a pair of perfectly correlated detectors allows to uniquely label each of the 4 correlation pictures. For example, every perfect correlation between detectors in the first correlation picture to the left will result in a product of equal to i. For the fourth correlation picture to the right the product will always be equal to one. This is possible for every dimension N. Interestingly, if $\phi \neq \pi/2$ (Eq.2.22) for one of the Bellports this labeling is not possible.

2.6 Perfect correlations - Separation of modes

A short explanation will be given on how the coincidence interference signal from 3 modes in a $N = 3$ system can be separated into interference signals from pairs of modes. This will be necessary for the experimental characterization of the source. Considering a three level system

$$|\psi\rangle \propto e^{i(\varphi_1+\varphi_1')}\,|11\rangle + e^{i(\varphi_2+\varphi_2')}\,|22\rangle + e^{i(\varphi_3+\varphi_3')}\,|33\rangle\,.$$

As shown in fig. 2.5 the state enters a Bellport $\psi \to \psi'$ on each side followed by coincidence detection leading to correlations. The intensity of the correlations ($CC_{(i,j)}$) between two detectors

(i, j) is defined by all relative phases

$$CC = |\langle ij|\psi'\rangle|^2 \equiv CC(\varphi_1 - \varphi_1', \varphi_2 - \varphi_2', \varphi_3 - \varphi_3').$$

In order to set $|\psi\rangle$ to a defined state the relative phases

$$\{(\varphi_1 - \varphi_1') - (\varphi_2 - \varphi_2'), (\varphi_2 - \varphi_2') - (\varphi_3 - \varphi_3')\}$$

have to be known. Assuming one applies a varying phase shift with amplitude 2π and a frequency $\nu >> 1/t_{int}$ bigger than the integration time of the single photon detectors onto one mode the coincidence signal becomes

$$\int_{t=0}^{t_{int}} CC\left(2\pi Sin(\nu t), \varphi_2 - \varphi_2', \varphi_3 - \varphi_3'\right) dt = CC(\varphi_2 - \varphi_2', \varphi_3 - \varphi_3')$$

and is only depending on the relative phase $(\varphi_2 - \varphi_2') - (\varphi_3 - \varphi_3')$. Therefore, for any entangled quNit state by applying a fluctuation signal to N-2 modes the resulting coincidence signal will only depend on the relative phase of the remaining two modes. In this way all phases of all qubit subspaces of the quNit space can be isolated.

2.7 Mutually unbiased basis and the Bellport

Of main importance in the discussion about the foundations of quantum physics has been the relation of position (x) and momentum (p) of a particle:

$$|\langle x|p\rangle|^2 = \text{const.}$$

The two operators x and p are complementary: the knowledge of the exact position results in no information about momentum. As emphasized by Bohr complementary properties of a quantum system are: "equally real but mutually exclusive" [38]. Position and momentum are a classic example of the continuous degrees of freedom of a quantum system. Another example would be the spin components of a spin 1 system in a discrete Hilbert space. Those two examples are the extreme cases: the continuous degree and the discrete Hilbert space of low dimension. The simplest discrete system would be the qubit and in the context of path-encoding the complementary observables of a Mach-Zehnder-Interferometer would be the which-path information and the interference pattern. Those two examples are only the extreme cases: the continuous degree of freedom and a qubit system. The transition from one to another is a quNit systems with $N \to \infty$. [38]
In a finite, discrete Hilbert space the analog of the complementarity equation for two bases $\{f_j\}$ and $\{e_i\}$ becomes

$$|\langle f_j|e_i\rangle| = \frac{1}{\sqrt{N}}\ ,\ \forall \{i,j\} = 1...N. \tag{2.27}$$

The to $\{f_j\}$ and $\{e_i\}$ corresponding non-degenerate observables $\widehat{F}$ and $\widehat{E}$ are complementary [39]. The two sets of bases fulfilling the above equation form a so-called mutually unbiased basis

(MUB) . The name highlights the fact that the information gained form measuring in one set of bases is completely unrelated to the information obtained from a measurement in the other MUB. Following section 2.4 a set of MUBs is of relevance for performing optimal tomography. A set of $N+1$ MUBs as consecutive von Neumann measurements provide N^2-1 real number results and hence fully characterize the state. Therefore, a set of $N+1$ MUBs is called maximal. In fact, there cannot be more than $N+1$ MUBs in dimension N [39]. In other words, using MUBs for state estimation maximizes the information per measurement and minimizes redundancy [40].
As mentioned above, for $N \to \infty$ a quNit system might transitions from the discrete binary (qubit) case to the continuous case. This is one motivation for studying the concept of MUBs in dimension N. Interestingly, generally the existence of a maximal set of MUBs in dimension N is not known. However, for N being a **prime number** or a **prime power** $N = p^M$ the existence of $N+1$ MUBs has been proven [38]. In any dimension it is always possible to construct at least 3 MUBs [39]. It has been established that for dimension $N = p_1^{n_1} \cdot _2^{n_2} \cdot ...$ with the **prime number decomposition** $p_1^{n_1} < p_2^{n_2} < ...$ the number of MUBs is limited by [4]

$$p_1^{n_1} + 1 \leq \#MUBs \leq N + 1.$$

However, for the first non prime dimension $N = 6$ no proof exists. Actually, for $N = 6$ numerical searches seem to strengthen a conjecture that no more than 3 MUBs exist in dimension 6. The upper limit of the number of MUBs has been proven to be $N+1 = 7$ [41]. Bengtsson introduced a measure of distance representing the amount of "unbiasedness" [41] with the distance being equal to one for two MUBs. A numerical search in $N = 6$ lead to the maximum value of 99.83%. From an experimental stand point this might be an interesting result meaning that one can construct MUBs very close to a maximal set.
The problem of finding maximal sets of MUBs seems to be of a more general type and seems to be linked or even reappear in varying form in very different fields ranging from the questions of existence of finite affine planes, in the theory of radar signals, Graeco-Latin squares or Lie algebra to name a few [4].

2.7.1 Experimental thoughts on MUBs

The problem of finding the maximal number of MUBs seems to be a purely mathematical problem. Although the equation defining MUBs might seem quite simple, finding a set of maximal MUBs becomes increasingly complex with the dimension N. According to [39], for example, the used numerical search algorithm gets "stuck" at local maxima with increasing probability the higher the dimension. For this reason, an experimental search equivalent to the numerical search for a complete maximal set of MUBs is also likely to fail in dimension 6.
From an experimental stand point the fact that sets of bases "very close" to a maximal set exist might be of use. In fact, the maximal set might not even be distinguishable from the set of close distance within experimental uncertainty. From a foundational quantum information theoretic perspective the consequence of a possible non existence of a (informational complete) maximal set of MUBs might be of great importance.
The generality of the problem and the dependance of the value of the dimension seem to suggest

a underlining structure based on number theory. However, the consequence of the value of the dimension on a physical system in the context of MUBs is an open question. For high dimensions $N >> 1$ the difference between N and $N+1$ seems to be of little importance. However, if N is a prime number there might be a fundamental information theoretic difference between the prime number system and the $N+1$ dimensional system.
Multi-qubit system are of prime power dimension $N = 2^m$ and therefore a maximal set of MUBs always exists. Hence, such a system can never examine systems where maximal sets do not exist (as conjectured). Here, quNit systems offer the possibility to exploit the "dimensional dependence" with the transition to the continuous case for $N \to \infty$.
Having the simplest path-encoded system, a qubit given in the σ_z basis $|\Psi\rangle = \alpha|0\rangle + \beta|1\rangle$ the other MUBs would be the σ_x and σ_y basis. This, of course, is realized by a 50/50 beam splitter (and a phase shifter). If one particle enters one of the inputs there is a equal $1/N = 50\%$ chance of exiting at any output. Therefore, eq. 2.27 is fulfilled. For a higher-dimensional system the same Ansatz can be used: the first basis will be the direct basis. The next basis can be found by applying a unitary U transformation to the state with $|U_{ij}|^2 = \frac{1}{N}$ and some phase shifters. More precisely, the elements of the transformation have to be $U_{ij} = F_{ij} = \omega^{i \cdot j}$ with $\omega = e^{i\frac{2\pi}{N}}$. F is called the Fourier matrix with all elements being a power of the N-th root of unity. Above, as introduced in [1] in the context of perfect correlations the Fourier matrix was also termed Bellport. For the dimensions $N = 2$ and $N = 3$ the Fourier matrix is uniquely defined. However, for $N = 4$ there is a one parameter family of Hadamar matrices [4]. This family of matrices has already been presented in eq. 2.22. Depending on the free parameter only for $\Phi = 0$ and $\Phi = \pi$ can a maximal set of MUBs be found. This is especially interesting in the context of section 2.5 where a unique labeling of the correlations was only possible for a certain phase $\Phi = \pi/2$. For $N = 5$ the Fourier matrix is uniquely defined. Generally, if N is a prime number the Fourier matrix is uniquely defined [42, 43]. However, from what is known, in $N = 6$ there is a two parameter family of Fourier matrices [4]. Without going into detail, this seems to make the search for a complete set of MUBs extremely difficult. Even numerical searches have not given a clear answer. For this reason an "experimental" search is also likely to be not very effective.
As a side note, the Hadamar transformation can be viewed as being constructed from 2-dimensional discrete Fourier transformations (beam splitter) [44]. There exists a more efficient algorithm, the Fast Hadamar Transformation, which recursively decomposes the transformation into FHT of size N/2 [45]. This is linked again to what has been described in section 2.3.8.
For prime dimensions there is a relatively simple way of constructing a set of MUBs [42, 4]. All MUBs can be reached with the Fourier transformation (Bellport) and different sets of input phases. For example in $N = 3$ and $N = 5$ a complete set of MUBs is given by

$$\begin{aligned} N = 3: &\quad \left\{\mathbf{1}, D^0F, D^1F, D^2F\right\} \\ N = 5: &\quad \left\{\mathbf{1}, D^0F, D^1F, D^2F, D^3, D^4F\right\} \end{aligned} \tag{2.28}$$

with $D = \text{Diag}\{1, \omega, \omega\}$ ($D = \text{Diag}\left\{1, \omega, \omega^4, \omega^4, \omega\right\}$) for $N = 3$ ($N = 4$) being a diagonal matrix realizable by phase shifters at the input of the Bellport [42].
Another interesting subgroup are the so-called **cyclic MUBs**. A cyclic set of MUBs is a maximal

set only defined by a single unitary transformation U satisfying $U^{N+1} = \mathbf{1}$. For certain N, for example, for $N = 2^m$ a cycling unitary has been found [46]. By applying powers of U onto the direct basis any MUB can be reached. This might be of experimental use some day in the context of state tomography. Additionally, a cycling unitary is useful for secure quantum communication protocols in higher dimensions [46, 47]. For $N = 2$ and $N = 4$ the cycling unitary takes the form [46]:

$$U_{N=2} = \frac{-1+i}{2} \begin{pmatrix} 1 & -i \\ 1 & +i \end{pmatrix} , \; U_{N=4} = \frac{1}{2} \begin{pmatrix} i & i & 1 & -1 \\ i & -i & 1 & 1 \\ i & i & -1 & 1 \\ i & -i & -1 & -1 \end{pmatrix} . \tag{2.29}$$

3 Realization of a source for entangled qubits

The realization of a source for entangled qubits will be presented.

3.1 Why fiber-integrated? Why $1550nm$?

Around $1550nm$ in the so-called C-band optical fibers achieve a transmission loss of less than < $0.2dB/km$. The reason is the transmission characteristics of the used Silica material. Therefore, the Telecommunication industry is concentrating on the c-band wavelength region. Virtually every standard in-fiber component is optimized and its performance is tailored towards C-band operation. Thus, in the context of on-chip and in-fiber integration $1550nm$ as the single photon wavelength is of advantage.
However, at the beginning of this work, most quantum optics experiments concentrated on wavelengths in the visible regime. One reason were the highly efficient Silicon-based single photon detectors due to the high absorption coefficient of Silicon and the Silicon tailored semiconductor processes. However, at 1550nm Silicon is transparent and therefore Si-based detectors cannot be utilized. The performance of existing detectors at $1550nm$ was not comparable to standard Si-based detectors.
Although, the visible wavelength region had the advantage of good detectors and well-known devices, in-fiber and integrated components were non-standard or non-existing. For the Telecom wavelength, on the other hand, high performance, out-of-stock, in-fiber and on-chip devices were available with a generally lower propagation loss. However, most of those devices have not been sufficiently tested at single photon levels.
We decided to focus on the Telecommunication wavelength pushing the experimental challenges into the field of quantum optics while at the same time we could rely on the already proofen standard devices and designs from the Telecom industry. Main attention has therefore been focused on characterizing the different devices for our purposes at single photon levels.

3.2 The source

The development of a novel fiber integrated source for path-entangled photons in the C-band at $1.55\mu m$ using only standard fiber technology is presented. Since an integrated realization of the Multiport will be chosen, the source should be compatible with path-encoding, scalable in terms of the complexity, and ultimately allow on-chip integration as well. For a path-encoded realization single mode optical fibers (SMF) come into mind. They have the advantage of low optical loss, near perfect optical modes, and easy handling. Furthermore, many high quality well-specified in-fiber devices are readily available at low cost. Additionally, SMF offer high mode matching to the on-chip optical modes of an integrated circuit.
What follows can be found in a compressed form in Schaeff et al. [23] and is presented here in more detail.

3.2.1 Preliminary

Some concepts and abbreviations from the Telecom area are quickly summarized. The wavelengths used for data transmission are typically grouped into wavelength bands. The conventional-band (C-band) ranging from $1530nm$ to $1565nm$ is commonly used today exhibiting the lowest loss in silica fiber.
For frequency multiplexing of signals so-called wave division (de-)multiplexers (**WDM**) are used. They are available at different channel spacing. A spacing of 100GHz is called **dense-WDM (DWDM)**. The spacing is defined in the 100GHz **C-band** ITU (International Telecommunication Union) grid relating a channel number 1...72 to a center wavelength.

Channel #	Frequency (GHz)	Wavelength (nm)
1	190100	1577.03
2	190200	1576.20
...	...	...
32	193200	1551.72
33	193300	1550.92
34	193400	1550.12
35	193500	1549.32
36	193600	1548.52
...	...	...
72	197200	1520.25

Table 3.1: 100GHz C-Band ITU Grid

WDM devices are commercially available in-fiber components based on Bragg reflection. A WDM has one fiber input called "COM" port and two outputs. The output port called "PASS" transmits one ITU channel while all other channels are reflected and exit at the output port "reflect". In the following "WDM" will refer to a multiplexer passing the signal wavelength around 1550nm while reflecting some other wavelength outside of the C-band typically 980nm or 780nm.
Important specifications such as the insertion loss (IL) are given on the **deci-Bell scale**: $r_{dB} = 10^{-r_{\%}/10} dB$ where r is a power ratio $r_{\%} = \frac{P}{P_0}$ relative to some value P_0. Intensities can be given in units of "dBm" with the reference point defined as $P_0 = 1mW$.
For quick calculations it is useful to keep in mind that:

$$3dB \approx 50\% \text{ and } 10dB = 10\%.$$

Any kind of **extinction ratio** will always be given in units of "dB" representing the power ratio of the signal and the residual power. **Optical cross-talk** between properties such as polarization or filter channel is defined in the same way.
Back reflection is the ratio given in dB between the inserted signal and the back-reflected signal.

The standard single mode fiber for operation in the Telecom band is abbreviated **SMF28** and will be the standard fiber type if not stated otherwise. **PM** fiber stands for polarization maintaining fiber.

3.2.2 Concepts of the entangled quNit source

The concept of the path-entangled quNit source is shown in fig. 3.1. N non-linear crystal waveguides are coherently pumped by a common pump beam λ_p split by a beam splitter leading to a superposition of N down conversion events happening in on of the N crystals. The down converted pair can be separated by N dense wave division multiplexers (DWDM) . In the following the modes are regrouped by wavelength resulting in a path-entangled two quNit state:

$$|\Psi_N\rangle = \alpha_1 |1_{\lambda_1} 1_{\lambda_2}\rangle + \alpha_2 e^{-i\varphi_1} |2_{\lambda_1} 2_{\lambda_2}\rangle + ... + \alpha_N e^{-i\varphi_N} |N_{\lambda_1} N_{\lambda_2}\rangle . \tag{3.1}$$

Here, φ_i represents the accumulated phase, while the amplitudes α_i are controlled by the splitting ratios of the $N \times N$ beam splitter. As described in section 2.3.6 (eq. 2.20) a projective measurements is realized by sending the state ψ into the $N \times N$ Multiport (fig. 3.1b) followed by detection.
The chosen design offers a relatively good scalability towards higher dimensions. Consider a quNit system at dimension N. If one wants to extend the source to dimension $N + 1$ another "arm" or mode (consisting of another crystal, DWDM, etc.) has to be added to the setup. The additional arm is not interfering with other parts of the setup. Only the pump beam has to be split once more to pump the additional $N + 1$-th mode. Therefore, the setup scales linearly in terms of its complexity with increasing dimension.

3.2.3 First realization - the qubit source

Due to the special design (fig. 3.1) it is possible to build the system using only in-fiber standard Telecom technology offering high quality, in stock, and well specified devices. All devices are coupled to fibers. Using fibers there is no need for (free-space) alignment making it easier to handle a high number of components. In principle, every used in-fiber device is also realizable within an integrated photonic circuit. This offers the possibility of a complete on-chip integration.

The design of the source for entangled qubits is depicted in fig. 3.2. In the following the important optical devices within the full setup will be introduced. Every component was characterized and specified at the single photon level.

Devices

Starting to the left, the pump beam at a wavelength of $\lambda_p = 775.06nm$ produced by a grating stabilized diode laser is split using a tunable in fiber beam splitter.

Tunable fiber beam splitter

A standard tunable fiber beam splitter is used to define the splitting ratio of the pump beam and in this way to set amplitudes of the entangled state ψ. A micro-meter screw sets the distance between two tapered fibers influencing the coupling ratio between the two fibers. The device is

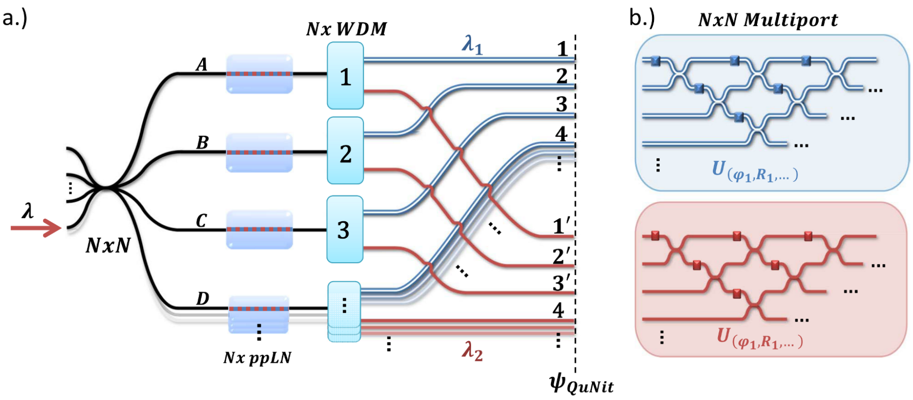

Figure 3.1: Example of a setup for creating and manipulating path-entangled quNit pairs. a.) N non-linear crystal waveguides (ppLN) are used offering the feature of integration together with a higher down-conversion efficiency compared to bulk crystals [48, 49]. All N crystals are coherently pumped by a common pump beam split on a $N \times N$ beam splitter. With a certain probability a photon pair is created via type-I spontaneous parametric down-conversion (SPDC):$\lambda \rightarrow \lambda_A + \lambda_B$. Due to the small conversion probability, the possibility of multiple SPDC events occurring in one or more crystals at the same time is negligible. Therefore, coherent pumping of N crystals will result in a superposition of the SPDC event happening in one of the N ppLN crystals. In the following step the SPDC pairs (λ_A, λ_B) in each mode (A,B,C,...,N) are separated by their wavelength using N dense wavelength division multiplexers (DWDM) into the two modes $1 \rightarrow (1_A, 1'_B), ..., N \rightarrow (N_A, N'_B)$. After regrouping the modes by their wavelength, a path-entangled two quNit state is obtained. b.) Each photon then enters an NxN Multiport, realized by a combination of phase shifters and beam splitters. By choosing the appropriate phase φ_i and reflectivity R_i settings any arbitrary N-dimensional unitary transformation can be realized. Combined with single photon detection a projective measurement is finally realized.

optimized for a wavelength of around 850nm. Thus, at $775nm$ the extinction ratio is not optimal and a splitting ratio range of only 10% to 90% can be achieved. The insertion loss at 775nm of around 1dB is quite high. However, at this point the loss of pump light can be neglected. After the beam splitter the pump light enters the N non-linear crystals.

ppLN crystals for SPDC

Integrated periodically poled MgO doped Congruent Lithium Niobate waveguide crystals (ppLN) directly packaged to fibers are used. They have been optimized for second harmonics generation $1550nm + 1550nm \rightarrow 775nm$ and are operated in reverse for spontaneous parametric down-conversion (SPDC). The down-converted photons are of same polarization. Phase matching is achieved by adjustment of the poling period using a temperature controller. Due to the nature of the waveguides only one pump polarization is guided through the crystal. Therefore, the SPDC process can be optimized by maximizing the transmission of pump power. The crystals are packaged to PM850 and PM1550 fibers. All crystals are characterized. Exemplary the measured specifications of one of the ppLN crystals is presented in fig. 3.3. The conversion efficiency per pump photon is relatively high, on the order of 10^{-5} to 10^{-6}. The spectrum can be considered quite broad covering almost the full c-band.

Within the down-conversion spectrum the generated photon pairs are correlated in their wavelength due to energy conservation $\lambda_p \rightarrow \lambda_1 + \lambda_2$. Therefore, a pair can be separated using wave division multiplexing.

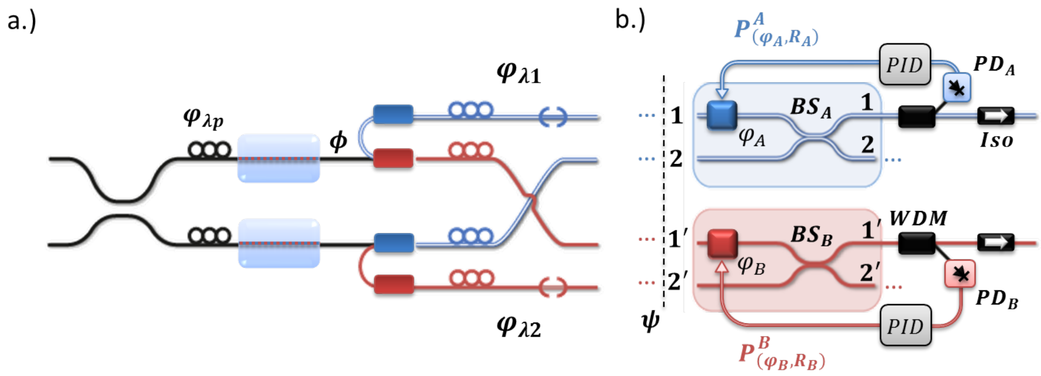

Figure 3.2

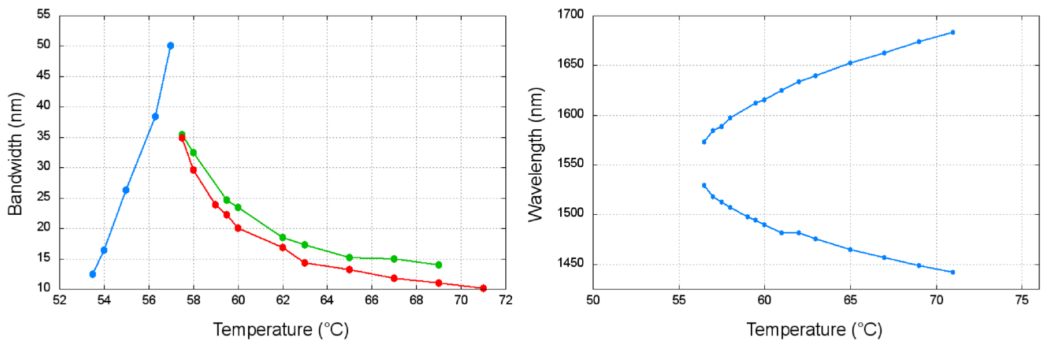

Figure 3.3: **Left:** Measured 3dB bandwidth of the down-conversion spectrum. Below $57°C$ the two spectra of signal and idler (green and red) overlap resulting in one broad spectrum (blue). **Right:** Center wavelength of signal and idler.

Wave division multiplexing Dense wave division multiplexers (DWDM) are used to separate the down-converted pair. A filter bandwidth of 100GHz has been chosen. Due to the high conversion efficiency cutting away most of the down-conversion spectrum is not problematic. The DWDM transmits a $100GHz \approx 0.8nm$ spectrum around its center wavelength while reflecting the remaining part of the c-band into another fiber. Two cascaded DWDMs are used to filter each of the two photons originating from the same crystal. The center wavelengths have been chosen to be ITU channel #32 (1551.7nm) and #36 (1548.5) being symmetric in frequency around $2 \times 775nm$. Fig. 3.4 shows an example of the transmission spectrum of two pairs of two cascaded DWDM channels.

Multiple DWDM devices have been tested. The combinations with the best match in center wavelength and equal insertion loss have been chosen. Common piezo fiber stretchers are used as phase shifters. In-fiber delay lines are inserted allowing to change the optical path by $\pm 2mm$ for alignment purposes. The outputs of each photon are connected to 50/50 fiber beam splitters. Together with the single photon detection a projective measurement is realized:

$$|P\rangle = \sqrt{1-\alpha}\,|1_{\lambda_1}\rangle + \sqrt{\alpha}e^{i\varphi}\,|2_{\lambda_1}\rangle$$

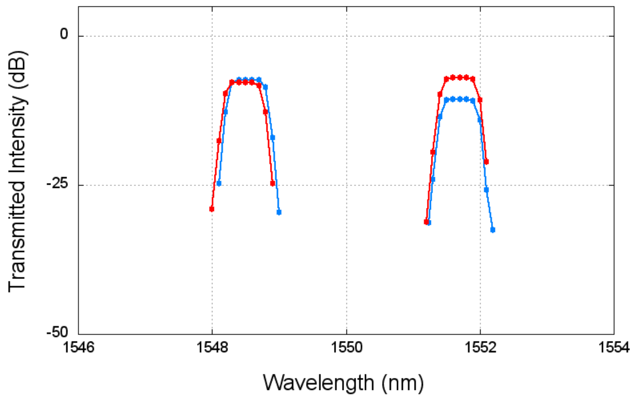

Figure 3.4: Transmitted spectrum of two (red and blue) pairs of DWDMs. The loss offset is arbitrary.

and analog for the modes of the other qubit. Before detection, after passing the beam splitter the pump light is separated from the single photon signal using a combination of in-fiber isolators and 850/1550 WDMs. The isolator has the property of transmitting 1550nm but absorbing 775nm. Eventually, the signal enters the single photon detectors.

Single photon detection

Triggered single photon detectors (id102, IDQuantique [50]) are used. One detector on the side of qubit A is continuously triggered at ν_T opening the detection window τ_g. If a photon is detected a trigger signal is send to the detector of qubit B opening its gate for τ_{cc}. If within τ_{cc} a photon is registered at detector 2 it is considered as one coincidence detection event.
The optimal detection setting with respect to the signal-to-noise ratio (SNR) was experimentally determined directly in the experiment. An optimum of $SNR \approx 100$ was found at the detection setting presented in tab. 3.2 with a detected coincidence rate of $150CC/s$ corresponding to a pump power of approximately $250\mu W$/crystal.

ν_T	1MHz
τ_g	100ns
τ_{cc}	2.5ns
τ_d	$100\mu s$
QE	10%

Table 3.2: Optimized detection setting. One detector is triggered at a constant rate ν_T and a gate time of τ_g. If a photon is detected detector two is triggered for τ_{cc}. Each crystal is pumped with approximately $250\mu W$/crystal leading to a coincidence rate of $150CC/s$ and $SNR \approx 100$.

3.2.4 Indistinguishability

The whole design relies on the indistinguishability of N SPDC events resulting in a superposition. It is crucial that all outputs of the state ψ_{quNit} (fig. 3.1) are the same in all physical properties (spectral shape, wavelength, arrival time, polarization, rate, loss). Therefore, ensuring indistuingishability has been of main concern. In the following important features allowing to distinguish the pairs are presented and the consequence on the visibility is estimated.

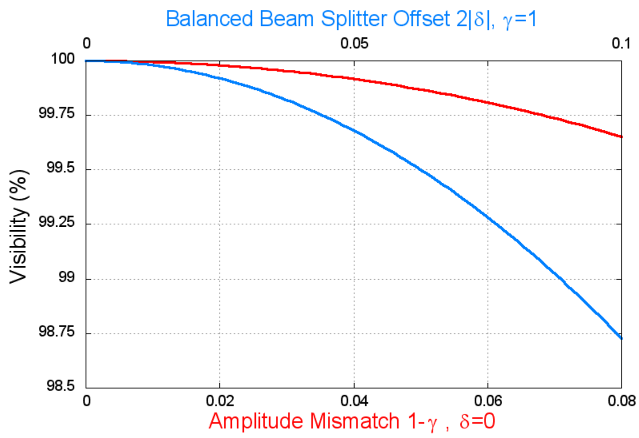

Figure 3.5: Reduction of the visibility of the state $|\psi\rangle \propto a_0 |00\rangle + a_1 |11\rangle$ entering a beam splitter with reflectivity $\sqrt{1/2+\delta}$. $\gamma = a_0/a_1$ is the ratio of the amplitudes, for $\gamma = 1$ both amplitudes are equal. δ defines the difference in reflectivity of the two beam splitters entered by the two qubits: $R = 1/2 + \delta$. Note that $2|\delta|$ is plotted.

Amplitudes, Loss

The amplitudes of the state ψ should be equal. The amplitudes are defined by different factors: the rate of produced pairs in each crystal, the loss, and the quantum efficiency of the detectors. In principle any difference in loss between the arms in the setup can be adjusted by changing the splitting ratios of the pump light. As can bee seen in fig. 3.5 (blue line) a mismatch of the amplitudes of two modes $a_1 |0\rangle$ and $a_2 |1\rangle$ interfering on a beam splitter with relative amplitudes of $\gamma = a_0/a_1$ leads to a reduced visibility depending on γ. Changing the pump ratios to adjust significant loss differences would also influence the signal to noise ratio (between real detected signal coincidences and accidental coincidences). Therefore, during construction of the source the devices have been characterized and combined such that equal loss is achieved within $\pm 0.15dB$. Using the tunable beam splitters the remaining imbalance of the amplitudes is adjusted. The precision of the adjustment is limited by the integration time of the detection as well as drifts of the beam splitter. The amplitudes are ensured to be the same by $\pm 5\%$ of the measured coincidence count rate (at $\approx 400CC/4s$) resulting in a maximal reduction in visibility down to

$$V_{\mathrm{Loss}} \approx 99.87\%.$$

Photon arrival time

Photon pairs coming from different crystals with different relative arrival times (due to different relative optical lengths) allow to distinguish different SPDC events. Therefore, the same relative arrival time has to be ensured within the single photon coherence length. This is not trivial because the internal optical length of all in-fiber devices is unknown. Fig. 3.6 shows the important optical lengths in the system. The length l_0 the pump laser acquires before entering the setup

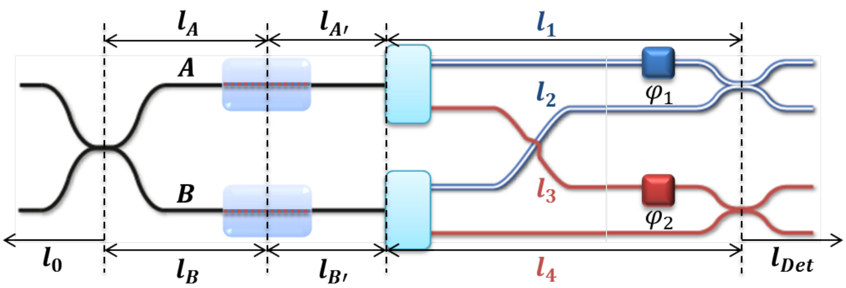

Figure 3.6: Sketch of the setup highlighting the relevant lengths of the system.

is irrelevant and can be viewed as a global phase. Same is true for l_{Det}. A necessary condition for the state ψ is the coherent pumping of the two crystals. Therefore, the two lengths l_A and l_B need to be the same within the coherence length of the pump laser. Paths $l_{A'}$ and $l_{B'}$ are taken by both SPDC photons of the created pair. Therefore, $l_{A'}$ and $l_{B'}$ are not relevant for the relative arrival time of the pair and can be viewed as a additional virtual path length adding to l_A and l_B of the pump beam. Thus, the necessary condition for coherent pumping of the crystals becomes:

$$l_A + l_{A'} - l_B - l_{B'} << \mathrm{coh}(\lambda_p). \tag{3.2}$$

In the following the photon pairs are separated and travel along different paths. The relative arrival time at the detectors of the different pairs comes into play:

$$l_1 - l_3 - (l_2 - l_4) << \mathrm{coh}(\lambda_{1550}) \approx O(mm) \ (@100GHz). \tag{3.3}$$

Two devices have been developed to measure optical lengths of fibers, they are shortly described in section 3.6. Additional delay fibers of certain lengths with a precision of $\pm 2mm$ are inserted into the setup and in-fiber delay lines τ are used for fine adjustments. The precision of measuring the relative lengths is $\pm 100\mu m$. Assuming the same spectral shapes, two Gauss functions of $100GHz \approx 0.8nm$ FWHM and at a distance of $100\mu m$ have an overlap of 99.9%.

Spectral properties

If the spectral properties of the SPDC produced photons filtered by the DWDMs differ in shape or center wavelength the SPDC events can be identified. The SPDC spectra of the two crystals has been measured (see fig. 3.3). Different DWDMs have been characterized for their spectral properties. Fig. 3.4 shows and example of a pair of DWDMs. The spectra can be assumed to be the same and little influence on the visibility is suspected. The DWDMs have a negligible cross talk between channels #32 and #36 of $> 50dB$.

Polarization

The same polarization is assured using fiber polarization controllers and in-fiber polarizers before detection. Although polarizers add additional loss and optical length to the system it greatly simplifies the alignment process. Effectively, the polarizers replace a misalignment in polarization by loss. Loss can be accounted for by the pumping ratios of the crystals. We found the polarizers to have an extinction ratio of at least $> 35dB$ at 1550nm. Therefore, assuming a polarization mismatch can be mapped to an amplitude imbalance of around ±5% the visibility is reduced to

$$V_{Pol} = 99.87\%.$$

Imbalanced beam splitters

In order to realize a projective measurement beam splitters are added. Surely, the will not be perfect 50/50 beam splitters. Any offset $(50+\delta)/(50-\delta)$ will lead to a non perfect interferometer with reduced visibility. The beam splitters have an intensity splitting ratio variation of 50 ± 5. As depicted in fig. 3.5 this corresponds to a visibility reduction by

$$V_{BS} = 98.0\%.$$

Phase noise

Setting the phase of the entangled state to a certain value will be treated separately. Here, we will only consider the effect on the visibility of a MZI with the existence of phase noise. Noise is considered to be any change in phase $\delta\varphi$ faster than the detectors integration time: $\sqrt{2}\,|\psi\rangle = |0\rangle + e^{i\varphi+\delta\varphi}\,|1\rangle$. Sending $|\psi\rangle$ onto a beam splitter one will measure an output intensity of

$$I(\varphi) = \frac{1}{4}\left|\int_{\varphi'=\varphi-\delta\varphi}^{\varphi+\delta\varphi}\left(i + e^{i\varphi'}\right) d\varphi'\right|.$$

The visibility therefore will be reduced by:

$$Vis(\delta\varphi) = \frac{I(\pi/2) - I(3\pi/2)}{I(\pi/2) + I(3\pi/2)} = \frac{sin(\delta\varphi)}{\delta\varphi}. \tag{3.4}$$

This relation is also illustrated in fig. 3.7. $\delta\varphi$ effectively reduces (increases) the detected maximum (minimum) measured intensity and therefore reduces the visibility. Assuming $\delta\varphi$ to be $\pm 5\%\pi$ results in a reduced visibility of 99.6%.

Total indistinguishability

To estimate the total reduction in visibility all distinguishing features mentioned above need to be taken into account. In principle, they cannot be treated separately. Nevertheless, for a first, rough estimate the total visibility approximates to

$$V_{Total} \approx \prod V \approx 97.3\%.$$

3.3 Phase control

The disadvantage of optical fibers is their relatively strong temperature dependence of the optical path [51] as well as the sensitivity of the phase towards vibrations [52]. Vibrations due to sound also strongly influences the pump interference signal. For this reason the setup has been

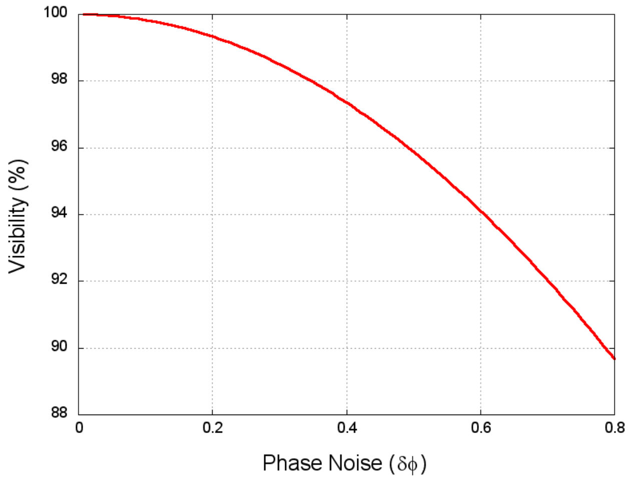

Figure 3.7: Reduction in visibility due to a noisy phase $\varphi + \delta\varphi$ for a state $\sqrt{2}\,|\psi\rangle = |0\rangle + e^{i\varphi+\delta\varphi}\,|1\rangle$ entering a beam splitter.

enclosed isolating it from air flow. The fibers are placed and fixated in paths cut into granular foam for temperature isolation. The temperature induced change in refractive index is directly proportional to the fiber length. Therefore, the length of the coherent part of the setup has been minimized and phase fluctuations were reduce to $\approx 1\pi/30s$.

3.3.1 PID

For control over the state ψ the phases need to be controllable. An active feedback control loop is implemented using a PID controller (fig. 3.8). Similarly to the single photons, the pump beam is transmitted through the whole setup and put to interference at the beam splitters (fig. 3.8b). The phase the pump beam λ_p acquires will be related to the phase of the single photon signal. Prior to single photon detection the pump interference signal is split using a WDM and detected using a photo diode (PD) .

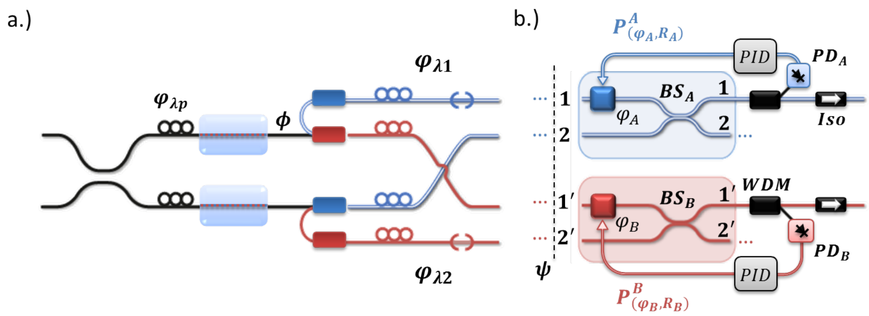

Figure 3.8

In the following, the elements of the phase control will be derived. Fig.3.8 displays all important (relative) phases in the setup. The entangled state Ψ before entering the beam splitters is of the form

$$|\psi\rangle = \frac{1}{\sqrt{2}} \left(e^{i(\varphi_p + \varphi_{\lambda_1} + \varphi_{\lambda_2})} |11\rangle + |22\rangle \right).$$

After the beam splitter, the probability of joint detection at $\langle 11|$ computes to

$$\langle 11|\psi'\rangle \propto e^{i\left(\varphi_p + \varphi_{\lambda_1} + \varphi_{\lambda_2}\right)} + 1. \tag{3.5}$$

For simplification, only the pair of output modes $\langle 11|$ is considered. It follows in order to set the entangled state to a certain phase

$$\varphi_p + \varphi_{\lambda_1} + \varphi_{\lambda_2} = c \tag{3.6}$$

needs to be constant.

Now the path of the pump light will be considered. If a photon at 1550nm acquires the phase φ_{1550} then the pump beam $\lambda_p = 775nm$ would acquire twice the phase $\varphi_p = 2\varphi_{1550}$. The single photon pair has a wavelength of $\lambda_1 = \varphi_{1550} + \Delta$ and $\lambda_2 = \varphi_{1550} - \Delta$. Therefore, if the photon pair acquires the phase φ then the pump traveling in the same mode has a phase of

$$\lambda_p = 2 * (\varphi_1 + \varphi_2) = 2\varphi_{1550}. \tag{3.7}$$

Thus, the phases ϕ_p and $\phi_{\lambda_1} + \phi_{\lambda_2}$ (see fig. 3.8a) acquired by the pump laser and the two single photons are equivalent and can be ignored. Following the pump beam in the upper (lower) modes ending at PD_a (PD_b) it acquires a phase of:

$$\begin{aligned} \varphi_p^{upper} &= \varphi_{\lambda_p} + (2\varphi_{\lambda_1}), \\ \varphi_p^{lower} &= \varphi_{\lambda_p} + (2\varphi_{\lambda_2}). \end{aligned} \tag{3.8}$$

$2\varphi_{\lambda_1}$ and $2\varphi_{\lambda_2}$ come from eq. 3.7. Similar to eq. 3.5 after the beam splitter a photo detector $PD_{a/b}$ will measure the intensity $I_{a/b}$:

$$\begin{aligned} I_a &= \left| e^{i\varphi_p^{upper}} + 1 \right|^2 \\ I_b &= \left| i\ e^{\varphi_p^{lower}} + 1 \right|^2. \end{aligned} \tag{3.9}$$

A feedback loop uses $I_{a/b}$ to control the phase shifter $\varphi_{A/B}$ such that $I_{a/b}$ stays constant:

$$\begin{aligned} const = c_1 &= \varphi_{\lambda_p} + (2\varphi_{\lambda_1}) \\ const = c_2 &= \varphi_{\lambda_p} + (2\varphi_{\lambda_2}) \\ \Rightarrow c_1 + c_2 &= 2\varphi_{\lambda_p} + (2\varphi_{\lambda_1}) + (2\varphi_{\lambda_2}). \end{aligned} \tag{3.10}$$

Eq.3.10 is equivalent to eq. 3.6 and therefore stabilizing the pump intensity through the setup allows for full control of the phases of the entangled state.

Monitoring the intensity I_a, eq. 3.9 allows to calculate the phase acquired by the pump φ_p^{upper}

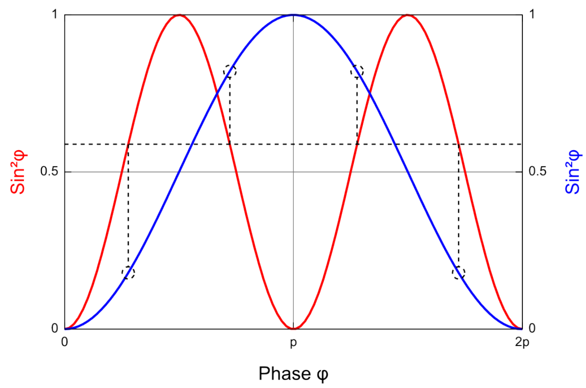

Figure 3.9: Illustration of the relation between pump intensity at 775nm (red) and the mean single photon wavelength at 1550nm (blue). For a certain pump intensity (dashed line) there are 4 possibilities for the single photon phase.

modulo $(\pi/2)$ (similar for φ_p^{lower}). At a certain pump intensity I_a there are $2\pi/(\pi/2) = 4$ possibilities for the actual single photon phase φ_{λ_1} (eq. 3.5) as illustrated in fig. 3.9. Therefore, before any experiment the relation is characterized: depending on a number of factors such as precision and time a number of measurement points (at least two for knowing the slope of the Sin^2) are taken putting (I_a, I_b) into relation with the detected single photon coincidences. The recorded data is fitted and the resulting fit parameters Λ are used to set the phase of the entangled state.

Realization of the phase control loop

A PID (proportional, integral, derivative) controller has been implemented. The PID has been designed build and programmed by Robert Polster, details can be found in his Masters Thesis [53]. A micro controller (ATxmega128a1,8Bit,16MHz) based design has been chosen. A custom circuit board includes the micro controller, analog-digital conversion of the detected photo detector signal, digital-analog converter, and an amplifying circuit for driving the piezo phase shifter up to 90V. The PID loop is performed by the micro controller connected to the PC. A number of serial commands have been developed related to specific tasks the PID has to perform during an experiment.

Fig. 3.8b shows the PID loop connected to the experiment. A WDM is splitting the pump light guiding it to silicon based photo detectors. The photo detectors (PD) output a voltage related to the detected intensity which is connected to the PID board.

3.4 Results

The source exhibits a high brightness and can reach detected coincidence rates of 1kHz at 100Ghz bandwidth and an input pump power of $250\mu W$ into each non-linear crystal. However, in order to decrease both the dark count probability and saturation effects of the photon detectors as well as to lower the number of filter devices required to block the 775nm light, lower pump powers are used. A coincidence count rate (CC) of roughly $150CC/s$ and an accidental coincidence rate of $(1.47 \pm 0.15)Hz$ is obtained. Thus, the coincidence-to-accidental-ratio is around $SNR \approx 100$. The accidental coincidence rate is estimated by introducing a time delay in the coincidence detection system such that any detected coincidence signal cannot originate from a true signal pair. The origin of the accidental coincidences is a systematic effect of a finite coincidence window of around 2.5ns (much longer than the coherence time of the photons) due to the timing jitter of the detector together with a combination of the intrinsic detector dark count rate, the residual pump light and photons at the signal wavelength originating from fluorescence inside the non-linear crystal.

3.4.1 PID performance

The PID is fast enough to stabilize the signal in most cases. Sounds or vibrations can sometimes cause the PID to shortly loose the signal. In such cases the characterization has to be repeated (see 3.3.1). In case the PID reaches the border of the piezo range a previously characterized value equal to 4π ($= 2\pi$ @ 1550nm) is subtracted from the applied voltage allowing in principle continuous stabilization.

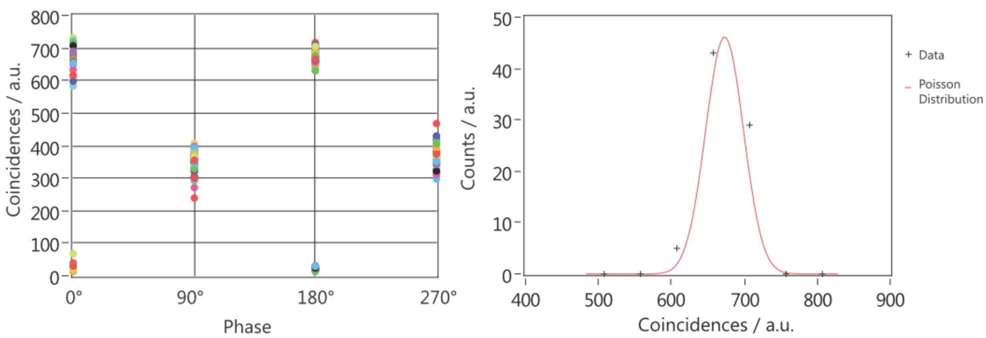

Figure 3.10: Data taken from by Robert Polster [53]. **Left:** The PID is continuously set to different phases and the coincidence signal is recorded. **Right:** For one phase setting a histogram is presented. The red line corresponds to a Poissonian distributed counting statistic centered at the theoretically expected value.

The performance of the PID has been estimated (fig. 3.10). Setting the PID to a desired phase φ the error introduced due to the PID stabilization is almost not distinguishable from the theoretical error expected from a pure Possonian counting statistic of the measured photons.

3.4.2 Source quality

In the following three experiments are presented from which a measure for the quality of the source can be obtained. As described in section 2.3.6 the beam splitter together with the phase shifter allows the realization of any projective measurement. In the following this is used to measure the according values sequentially setting the phases to the corresponding setting followed by single photon coincidence detection.

Entanglement visibility

Ideally, for a maximally entangled state the visibility would be $V = 100\%$, its deviation is a direct measure of the achieved indistinguishability of the two SPDC events and a measure of the quality of the source. Setting the phase difference to 0 and π the maximum and minimum coincidence count rates are obtained leading to a visibility of

$$V = (95.6 \pm 0.4)\% \ , \ V_c = (97.3 \pm 0.5)\% \tag{3.11}$$

in the equal-superposition basis with V_c including subtraction of accidental coincidences. The reduction of the visibility from the perfect 100% is most likely a result of a residual distinguishability. Note, that the accidental corrected visibility cannot be distinguished from 100% in the computational basis. Here, the computational basis corresponds to a direct measurement of the state (ψ in fig. 3.2) with beam splitter after ψ (fig. 3.2) removed.

CHSC inequality

To further stringently verify the quality of entanglement of our source a violation of the CHSH Bell-like inequality is tested [54]. Above a value of 2 the result cannot be explained by any local-realistic hidden variable model. Thus, the corresponding state must be non-separable and therefore entangled. For a maximally entangled state quantum theory predicts a maximum value of $2\sqrt{2}$. Therefore, the S value is a measure for the quality of the source. Directly from the measured count rates without any correction the S value is obtained as

$$S_{CHSH} = (2.70 \pm 0.03).$$

This corresponds to a violation of the CHSH inequality by more than 20σ. Compared to the ideal value $2\sqrt{2}$ the measured value shows a reduction of $(95.5 \pm 0.7)\%$. This is in excellent agreement with the non-perfect measured visibility (eq. 3.11).

Tomography

Following section 2.4, the entangled state ψ is measured in all three mutually unbiased bases. After subtracting the residual accidental coincidences from the data, using maximum likelihood estimation, the density matrix ρ of the state is reconstructed (fig. 3.11). From this the state fidelity F, as a measure of overlap between the measured and ideal state, and tangle, as a common entanglement measure, are obtained [55]. Compared to the ideal state, the state fidelity F and tangle τ are estimated to

$$F = (96.86 \pm 0.15)\% \text{ and } \tau = (87.9 \pm 0.6)\%$$

and corrected for accidental noise:

$$F_c = (99.44 \pm 0.06)\% \text{ and } \tau = (97.9 \pm 0.2)\%.$$

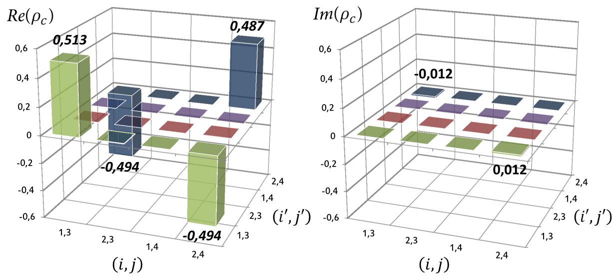

Figure 3.11: Real and imaginary parts of the density matrix ρreconstructed by maximum likelihood estimation after accidental noise subtraction. Unlabeled data corresponds to measured values smaller than $Re(\rho) < 0.005$ and $Im(\rho) < 0.0008$.

These values are the intrinsic fidelity and tangle of the source. This agrees well with the previous measurements of the quality of the state. The errors are estimated by a Monte Carlo simulation of the reconstruction analysis assuming Poisson noise in the measured counts.

3.5 Discussion & extension to higher dimensions

The results presented in section 3.4 where promising towards an extension to higher dimensions. The deviation from the perfect visibility is in the range of what is to expect from the characterizations and estimations of the single devices (section 3.2.4). The extension to a two entangled ququart system is straight forward and follows to what has been described. In the following, some changes to the setup are listed.

- The sensitivity to vibrations and sound had to be reduced. From the work of Hati, Nelson, and Howe [52] one may deduce encapsulating the fiber into grooves of foam, gluing or taping it down induces stress. Stress in turn seems to be inducing a higher vibrational sensitivity of the phase [52]. Spliced fiber connections also produce stress which might also increase phase sensitivity. This has not been examined within the given time. However, there is no way around splicing some fibers. Hence, the setup has been rearranged. Fibers are mostly guided freely on a bread board loosely fixed by tape. The board itself is standing on isolating feet on an optical table. A significant decreases in vibration sensitivity is observed and can now be ignored within the lab environment.

- A new enclosure of the source has been designed further isolating the system and thereby improving stability. The phase is typically changing on a scale of $\leq 1\pi/5min$. The sensitivity to sound has reached a level where it does not affect the functioning of the system.

- The PID loop frequency has been increased by increasing the clock frequency of the micro controller as well as optimizing the program for speed. After the experiment it became apparent that minimizing the length of the setup is not important since the PID could handle drifts easily. A test showed that stabilizing $10ths$ of meters of fiber is not a problem.

- Fluctuations of pump power transmitted through the non-linear crystals was a major problem during the experiment. The used crystals were packaged to PM800 and PM1550 fiber.

We expect a misalignment of the PM fiber axis with respect to the crystal. Taking extra care during alignment of the pump polarization minimizing the fluctuations partly solves the problem. However, lower fluctuations than 5% of the crystal pump power could not be reached. Thus, the crystals have been replaced. The PM fibers are now aligned with a higher precision and power fluctuations are reduced.

- The temperature control has been replaced. The old control was a slow relay based system causing large temperature variations around the set-point. We expected those variations to also have an effect on the pump fluctuations.

- It became apparent the current detection scheme will hardly work for the higher dimensional source with a higher loss (due to the Multiport). The new detection scheme will be introduced in a following section.

- The visibility V of the interfered pump light was the biggest obstacle. It was clear that this would be of main concern when increasing the dimension of the system. There is little control over the pump light through the setup since alignment concentrates on the indistinguishability at the signal wavelength. Improvement can therefore only take place electronically at the photo detector (PD) output.

- The tunable beam-splitters turned out to be unstable in time ($\approx$ days) and generally unreliable. They have been replaced by fixed splitting ratio in-fiber beam splitters. Fine tuning of the amplitudes is achieved by adjusting the polarization of the pump before entering the non-liner crystals.

- Electric filters have been implemented in front of the phase shifters filtering external sources of electrical noise.

- The phase stabilization scheme will be changed accounting for the added modes of the higher-dimensions.

Fig.5.1 shows the source extended to four arms resulting in the entangled ququart state

$$|\psi\rangle \propto |00\rangle + e^{i\varphi_1}|11\rangle + e^{i\varphi_2}|22\rangle + e^{i\varphi_3}|33\rangle .$$

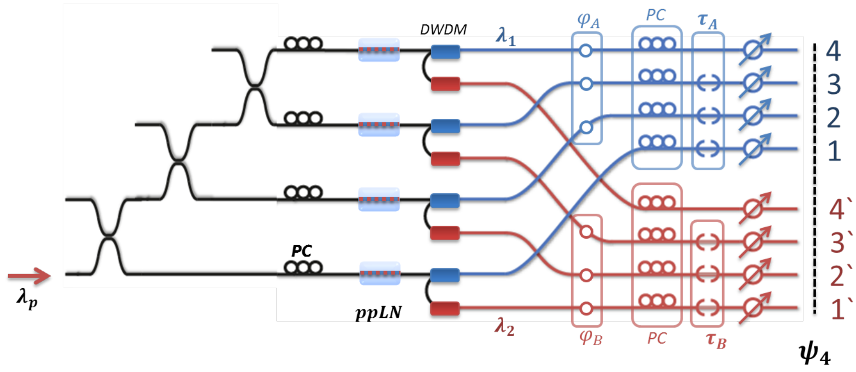

Figure 3.12: Extended source for producing path-encoded entangled ququarts.

3.6 Length measurement

Two types of length measurements have been used for measuring optical paths of fibers.
The first method utilized a white light interferometer using a broadband light source at 1550nm and an in-fiber motorized delay stage in one arm of a Mach-Zehnder interferometer. Inserting fibers into the arms of the interferometer one finds the maximum interference signal at a certain delay which relates to the relative optical path. A precision of $\pm 100\mu m$ is reached for a $\approx 30s$ measurement and $\approx 300\mu m$ for a 1s measurement. The system has already been described by Polster [53]. The method has also been used at single photon levels inside the setup along with the first construction of the setup.
The second method is used for a quick but less accurate measure of fiber length and has turned out to be extremely useful taking only a few seconds to measure a fiber length with an accuracy of approximately $\pm 2mm$. Often the precision is sufficient and translation stages can be used for final fine adjustment. Furthermore, it is a cost efficient and easy design. A standard laser distance meter (Toolcraft, LD50) is used. It features a specified accuracy of $\pm 2mm$ up to a length of $50m$. Although developed for free space application it has turned out to be of comparable quality for in-fiber devices. Compared to other commercially available devices, this version is of low cost, worked for all tested fibers types, and can tolerate a high loss. The accuracy of measuring the fiber length has been found to be of order: $\pm 2mm$. However, it depends on the insertion loss, fiber type, and length.

4 Realization of the general Multiport

The realization of the Multiport as a photonic integrated circuit (PIC) will be presented. Because integrated optics is in some way new to the area of quantum optics a short detour presenting the different materials and production processes will be taken in the next sections.

4.1 Introduction - Why integration

The initial motivation of integrated optics might have originated from the prospects and achievement of integrated electric circuits where extremely complex structures such as micro controllers were developed with millions of transistors units. However, integrated optics faces some difficulties. Integrated devices who serve an optical function are mostly geometrically related to the wavelength and therefore their size is often limited by multiples of the wavelength as well. Furthermore, optical connections are significantly more critical compared to their electrical counterparts and the relatively high loss requires complex amplification devices. [56]
However, integrated optics offers huge possibilities to quantum optics. Integrated devices are typically buried inside a single material chip with phase stability intrinsic to the system. Furthermore, the standard semiconductor foundry technology has reached such high levels that thousands of (optical) devices can easily be handled. Thus, the complexity in terms of the number of devices most integrated quantum optical circuits would require is negligible. Consequently, photonic integrated circuits (PIC) have successfully been implemented in various photonic quantum experiments. Shor's factoring algorithm has been demonstrated [57], quantum random walks have been observed [58], a probabilistic C-NOT gate has been realized [59], and delayed choice experiments [60], entanglement manipulation [61, 62], or boson sampling [63] has been demonstrated. Further highly complex PICs containing multiple beam splitters and phase shifters have been used in various other quantum experiments [64–67, 60, 68].
In an quantum optical setup phase coherence of a quantum state is of crucial matter. Phase stability quickly becomes an issue using classic bulk optic implementations. Hence, integrated optics seems promising towards more complex quantum optical setups. However, optical loss is an issue. It becomes the bottle-neck in quantum optics where optical amplification simply is not an option. Therefore, most properties of the integrated circuit in this thesis has been tailored towards reducing the total loss of the device.
The Multiport as a realization of any unitary operator has been proposed by Reck, Zeilinger, Herbert J., and Bertani [20], Zukowski, Zeilinger, and Horne [1]. Multiports of fixed settings have already previously been realized. For example, in-fiber 3×3 fused couplers and on-chip integrated 4×4 multi-mode interference (MMI) couplers of fixed splitting ratios have been utilized for observing two photon interference [21, 60, 69]. Using fixed splitting ratio fused 3×3 fiber couplers a three-path Mach-Zehnder interferometer has been constructed with piezo fiber phase shifters in each arm. A three-path interference pattern has been observed using a cw laser by Weihs, Reck, Weinfurter, and Zeilinger [22]. Furthermore, each photon of an entangled photon pair was inserted into one input of a Franson-type three-path Mach-Zehnder interferometer by Reck [30]. With a freely drifting phase while recording the coincidence signal, one of three possible sets of perfect correlations between detectors were observed. Furthermore, the correlation

space of one of the three output combinations was measured for 36 phase settings with a visibility of $< 60\%$ [30], again, using fixed splitting ratio fused 3×3 couplers.
Although qutrit-qutrit correlations have already partly been observed a complete characterization is missing. The reason mainly is due to missing control of the system. A fixed ratio splitter represents only a particular unitary transformation and thus only corresponds to one element of SU(N). So far, an integrated realization of the general Multiport covering the full SU(N) space has not been demonstrated.
In the following a brief overview of the area of integrated optics will be given starting at the different materials and production methods and leading to commercially available state-of-the-art integrated devices.

4.2 Materials

Different material combinations can be used to form a waveguide. Some examples of the base material are Polymers, Silica, Silicon, Chalcogenide, $LiNbO_3$, $LiTaO_3$, InP or Si_3N_4 based. Waveguides are formed by increasing the relative refractive index in the core regions. One way of sorting the different materials is by their index contrast $\Delta = (n_1 - n_2)/n_1^2$ between core and cladding. The higher the contrast Δ the more compact the integrated circuit due to a lower waveguide bending radius and mode size [70]. A main cause of propagation loss is the waveguides sidewall roughness (between core and cladding material) inducing scattering [71]. Especially, the sidewall roughness compared to the waveguide size is considered to be the important factor.
In the 1960s **Lithium Niobate** ($LiNbO_3$) was rapidly recognized as a suitable material offering a relatively low loss and strong electro, acousto optic and piezo effects. Besides being a birefringent material, $LiNbO_3$ has a high non-linear coefficient leading to efficient frequency conversion mechanisms. For this reason, around 1985 a variety of active $LiNbO_3$ devices such as fast modulators [72] and a high integration level of up to 50 switches on one chip have been realized [73]. In parallel other circuits based on other materials such as polymers, silica on silicon or semiconductors such as indium phosphide, gallium arsenide or silicon have been developed.
The different available materials (semiconductor and dielectric) have led to two approaches: monolithic and hybrid integration.
The highest level of integration can be achieved in full monolithic integration. All optical components from light source, mode control, electronics and detectors are integrated on a single substrate. Most promising for **monolithic integration** are semiconductor materials such as **GaAs** or **InP**, both offering strong optical effects at a high bandwidth. Especially the possibility of the integration of InGaAs based single photon detectors might be of advantage from the quantum optics perspective. Furthermore, high quality polarization management is achieved. Monolithic integration has become a standard base for different commercial products such as optical hybrids [74].
Hybrid integration chooses a different approach. Specific materials are used for different optical elements performing a particular optical task such as detection, modulation, or switching. They are either directly connected or mode converters and optical fibers are used as an interconnect. Here, some examples are silica and silicon based circuits combined with short regions

of strong electro-optic materials such as $LiNbO_3$.
Silica on Silicon (SiO_2/Si) has also become of great interest. Historically, it is the most well-known material in semiconductor industry with good quality, low priced substrates and very controlled, specified and optimized processes [75]. This results in high quality circuits with unprecedented low loss. Additionally, with an index contrast of around $\Delta \approx 0.1\% \text{to} 1.5\%$ and a waveguide cross section geometry of $\approx 6 \times 6 \mu m^2$ Silica waveguides are closely impedance matched to optical fiber. This results in low fiber coupling loss as well as low back reflections, both of great importance for long haul fiber applications. For this reason Silica on Silicon has become of great importance in the fiber telecommunication industry. However, due to the low index contrast silica waveguides are characterized by large dimensions with bending radii on the order of $\approx mm$.
Here, **Silicon on insulator** (SOI) with a very high contrast between Silicon (core) and insulator (for example air) is of use. This provides a high confinement and compact circuits. For comparison, according to [75], Arrayed Waveguide Gratings (AWGs) based on Silica waveguides ($\Delta < 1\%$) for a 1×4channel multiplexer/demultiplexer result in an approximate sizes of $12.5 cm^2$. The similar device based on Silicon on Insulator will have an approximate size of $0.5 cm^2$ [75]. SOI has developed its own momentum and has become a "sufficient viable solution" as a commercially successful platform [76]. Even high performance integrated Ge-on-Si photo diodes [77] and Lasers at the Telecom wavelength [78] have been demonstrated. Modulation based on the thermo-optic effect is limited in bandwidth, however, sub-μs response is possible [79] and modulation in the 10GHz regime using the plasma dispersion effect has become a standard [76]. However, the drawback of miniaturization is the increasing waveguide sidewall roughness compared to the waveguide dimension leading to scattering loss [71]. Therefore, Silicon waveguides generally can be considered to have a higher propagation loss compared to circuits of lower contrast assuming the same level of process control. **Silicon Nitride** based waveguides with a low attenuation and operations from 400nm to 2350nm have also become a viable platform with a full range of passive and active optical devices available [80]. To my knowledge, the lowest achieved propagation loss is $0.1 dB/m = 0.001 dB/cm$ using a SiN_3/SiO_2 Silica waveguide and an optimized fabrication process [80].
Silica has been chosen as the base waveguide material for the realization of the Multiport. It offers the lowest propagation and fiber coupling loss which is the most crucial property at single photon level. Also, fiber alignment is not as crucial and sensitive for low contrast waveguides. A propagation loss of as low as $0.01 dB/cm$ [81] has been demonstrated. The circuits have been proofen to be sufficiently polarization independent [82]. Additionally, a high level of complexity has been achieved for commercially available devices. The relatively slow thermo-optic effect ($\approx ms$ [82]) is not of concern due to the long single photon detection integration time in most quantum optical experiments. Due to the high state of the art of fabrication, reliable devices can be obtained with a high level of complexity. Basic waveguide structures have become a standard tool (which distinguishes Silica PICs from many other methods). As demonstrated in 2001 implementing hundreds of optical devices on a single chip does not pose a major problem [82] (500MZIs, 1024 phase shifters, insertion loss 6.7dB, total waveguide length 66cm, 0.75%Δ, polarization dependent loss 0.11dB, MZI switching time 4.1ms). Silica has been identified as a

promising candidate for PLC switching where a number of input signals are redirected to certain outputs [83]. The design of such switching devices comes extremely close to the integrated design of a Multiport. They have been a major focus of development for telecommunication applications.
The trend in Telecommunication industry (the driving force behind most of PIC research) seems to be towards a higher level of miniaturization resulting in more compact, faster, less power consuming and cheaper devices. Therefore, following to some extend the same path as the Telecom market and trying to utilize it for quantum applications might be of advantage in future.

4.3 Fabrication of Silica-on-Silicon photonic integrated circuits (PIC)

Fabrication begins with deposition of a silica cladding layer via thermal oxidation onto a base silicon wafer. Above, a core layer is deposited. A common process is chemical vapor deposition (CVD). Introducing different gases into the reaction chamber will have different effects on the deposited layer. The introduction of GeH_4 will increase the refractive index of the layer resulting in a germanium-doped silica core with an index step of around $7 \cdot 10^{-3}$. Applying standard photo-lithography the core layer is patterned. Etching of the core can be done via reactive ion etching (RIE). The process has to be carefully controlled for obtaining smooth surfaces with a low roughness [71]. In the following the mask is removed in an appropriate solvent. Eventually, the core is covered by the top cladding layer using CVD.

4.4 The Multiport chip - Description of the fundamental devices

Fig. 4.1 shows the final design of the Multiport. As expected, the Multiport is built from $SU(2)$ operations realized by a MZI formed by two 50/50 beam splitters with two phase shifters in between. The phase shifters are simple heaters using the thermo-optical effect. The final chip will contain multiple independent PLCs: the qubit, qutrit, and ququart Multiport along with some test structures. Independent structures are separated by $500\mu m$. A doped Silica waveguide realization of low index contrast has been chosen for the purpose of low loss and good mode matching to single mode fibers.

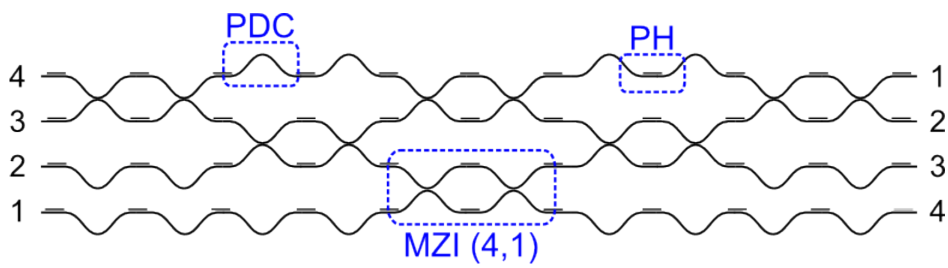

Figure 4.1: Schematic of the final Multiport design containing path difference compensators (PDC), MZIs acting on the mode (i, j) and phase shifters (PH).

In the following the important on chip devices are shortly described.

4.4.1 Straight Waveguide

The straight waveguides are formed by a $6\mu m^2$ doped Silica core surrounded by Silica. The core is located in the middle of a $30\mu m$ high Silica layer grown on top of a 1mm thick Silicon wafer. The index contrast is approximately $\Delta \approx 1.5\%$ with a cutoff wavelength of around $\lambda_{cutoff} \approx 1450nm$. The maximum power input is $P_{MAX} \approx 30-40mW$. The estimated propagation loss is $0.2dB/cm$. The waveguide modes of the Multiport are separated by $250\mu m$ thereby matching the pitch of standard fiber arrays.

4.4.2 Directional coupler (DC)

The 50/50 coupler with a waveguide width of $3.8\mu m$, a pitch of $6\mu m$ and a length of the evanescent coupling region of $78\mu m$ is shown in fig. 4.2. On both sides the waveguides fan out to $40\mu m$ pitch and then in a second fan-out to the standard $250\mu m$ pitch connecting to the straight waveguides. The total length is 5mm. The aimed for precision in reflectivity is $R = (50 \pm 5)\%$.

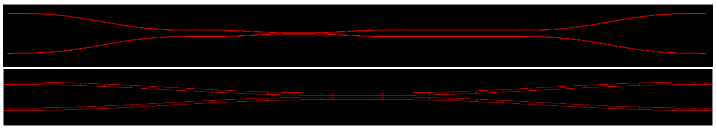

Figure 4.2: **Top:** Layout of a directional coupler (DC) as the realization of a 50/50 beam splitter. **Bottom:** Magnification of the coupling region.

4.4.3 Thermo-optic phase shifter (PH)

A conducting metal track of $2\mu m$ hight, 5mm length, and width of $50\mu m$ is placed on the surface $\approx 15\mu m$ above the waveguide (fig. 4.3). The waveguide is surrounded by deep etch wells (depth $\approx 300\mu m$) undercutting the waveguide. The result is an increased thermal isolation, reduced power consumption and thermal crosstalk. The total length is 5mm. The resistance of the phase shifter is approximately 160Ω with a π voltage of $U_\pi \approx 30mW$ and $U_{2\pi} \approx 60mW$.

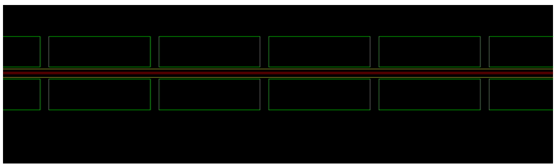

Figure 4.3: Layout of the thermo-optic phase shifter (PH). The etched wells surrounding the waveguide are marked in green.

4.4.4 Path difference compensator (PDC)

Similar layout to one arm of a DC. The purpose of the device is to compensated length and loss differences within the circuit. For example, in the case of the 3×3 Multiport (see fig. 4.1) one mode enters a PDC to compensate for loss and length differences due to the two other modes entering a MZI.

4.4.5 Mach-Zehnder interferometer

A Mach-Zehnder interferometer (MZI) will be build out of two DCs with phase shifts in each arm. To compensate for path differences other waveguides not entering a MZI are inserted into a PDC.

4.4.6 The full chip

Fig. 4.5 and fig. 4.4 show the full $6mm \times 100mm$ chip containing the 4×4, 3×3 and 2×2 Multiport together with other test structures. As described above, the waveguides have a pitch of $250\mu m$ aligning to the pitch of standard fiber arrays. Between two devices such as two different Multiports the pitch is $500\mu m$. The facets of the chip are polished for optimal coupling to single mode fiber. In principle, an angled polish or coating could be utilized to minimize back reflections.

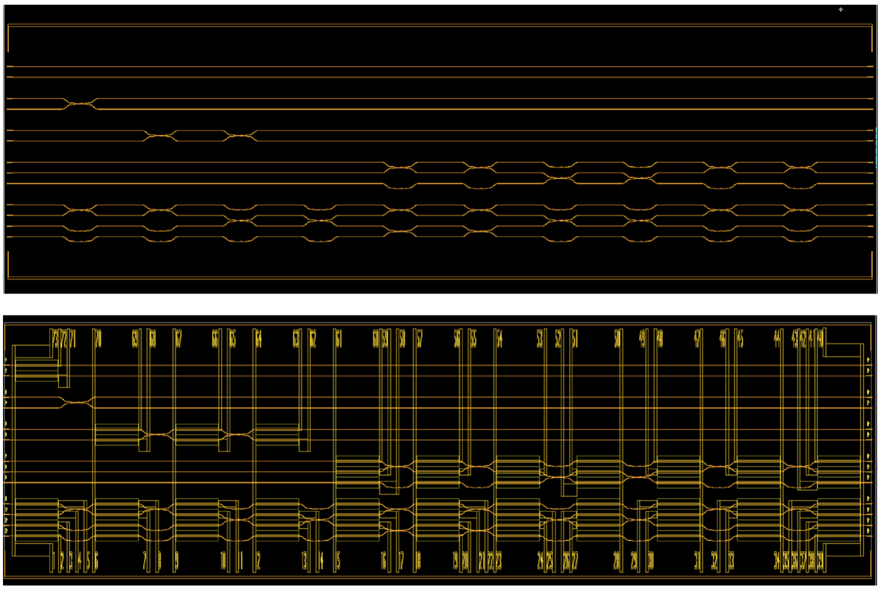

Figure 4.4: Design of the Multiport Chips. From top to bottom one can see straight waveguides, a beam splitter, a MZI (the 2×2 Multiport), the 3×3 Multiport and the 4×4 Multiport. a.) Waveguides only b.) Waveguides and electrodes layer.

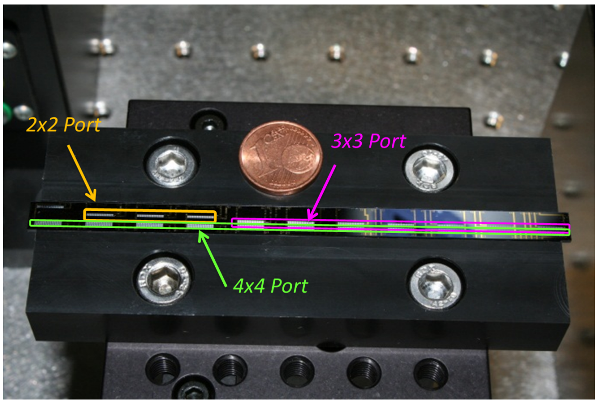

Figure 4.5: Actual Multiport $100mm \times 6mm$ chip containing the 4×4, 4×3 and 2×2 Multiport together with other simpler test structures. Waveguides cannot be seen, white: areas of phase shifters, electrodes are golden.

4.5 Optical and electrical coupling

The process of coupling the integrated chips to optical fibers is reviewed. During the characterization of the Multiport a full coupling setup has been developed allowing for optical coupling and permanent packaging of fibers or fiber arrays, and electric coupling and permanent packaging of all (≈ 80) electric pins to an electric circuit via an alignable probe card. The chips can be temperature stabilized allowing for temperature dependent measurements. The whole coupling system has been used and further improved on in a project by Sebastian Ecker and is described in full detail in his project thesis [84]. Although major effort went into the coupling setup, only a rough outline is given. All details have been described along with complete instructions within [84]. Section 4.6 will continue with the characterization of the basic properties of the Multiport using the coupling setup.

Fiber arrays of up to 12 fibers aligned precisely ($\pm 1\mu m$) and matching the on-chip waveguide pitch of $250\mu m$ are used to couple the fibers to the chip. The chip is placed into a holding post between two 6-axis stages. The fiber arrays are mounted onto the two 6-axis alignment stages. The post can be used to temperature stabilize the chip for temperature dependent measurements. Cw-light at 1550nm is inserted into one of the fibers on the right side. A lens system magnifies and projects the output facet of the chip onto a fluorescent screen imaged by an objective and a CCD camera serving as a first feedback for alignment. Eventually, the fiber-chip-fiber transmission is maximized using all degrees of freedom.

Once the chip is tested the permanent packaging of the chip is performed. Previously to coupling a lid is placed on the Multiport chip (fig. 4.6). The purpose of the lid is to increase the face area of the chip for the index matching glue. The placement of the lid is a sensitive matter and has to be aligned precisely with the chips facet. Otherwise, during the curing process and contraction of the glue the angled surface will cause a misalignment. For this purpose an extra setup has been developed allowing for precise placement [84]. The properties of the index matching glue are chosen as a compromise between the refractive index (being close to the waveguides and fibers) and exhibiting little and uniform contraction during curing. UV light is used for slow and uniform curing. A second glue is used to further support the fiber-chip joint. The chip is now permanently coupled (fig. 4.6).

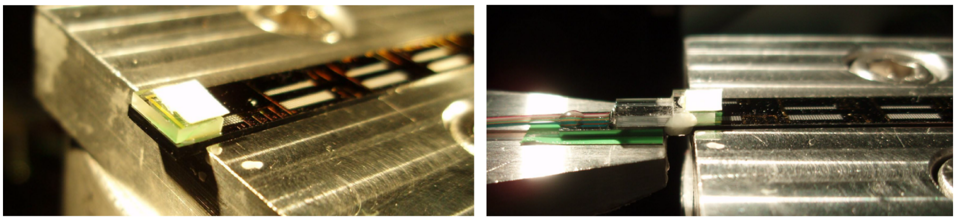

Figure 4.6: **Left:** Picture of a lid placed precisely on top of a Multiport chip. **Right:** Picture of the finished packaged joint between Multiport chip and fiber array. Pictures taken by Sebastian Ecker

As shown in fig. 4.4 the Tritter has around 21 contact pads leading to phase shifters while the full chip has more than > 80 connections. An electric probe card has been used. The probe card is a commercially available product typically used for connecting multiple contacts on electric circuits. The probe card has aligned pins placed at a certain position with a precision of $\pm 0.5\mu m$ in every direction (fig. 4.7). The probe card has been cut and rearranged to fit into a holder. With the chip mounted inside the setup the probe card can be aligned freely with respect to the chip. During alignment an electric circuit indicates closed connections on the Multiport chip. Offset and tilt of the probe card with respect to the chip is deduced and readjustments are made. Once aligned and connected the probe card is screwed to the base holder of the chip and the fully packaged chip (fig. 4.8) can be removed.

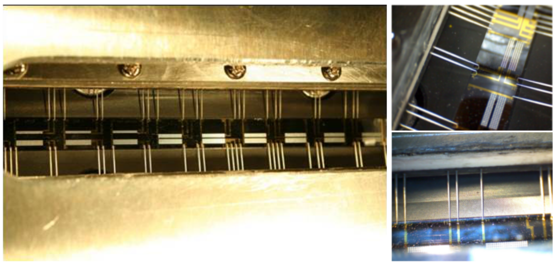

Figure 4.7: **Left:** Picture of the probe card during alignment. **Right:** microscope image aiding during probe card alignment.

4.6 Characterization of the passive properties of the basic integrated devices

In the following the measured basic properties of the Multiport chips are given. The values given below are typical worst case values averaged over multiple characterizations of different chips with different fibers and arrays.

Insertion loss of a straight 10cm long waveguide including in- and out-coupling at $1550nm$ is determined to

$$IL \approx 4dB.$$

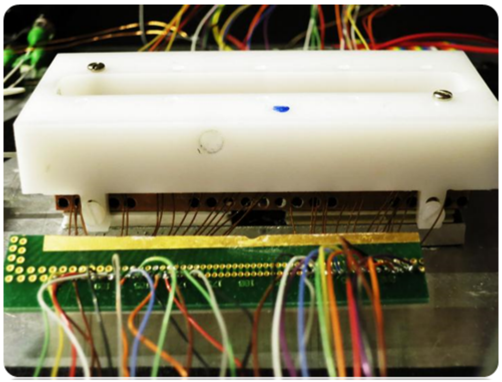

Figure 4.8: Picture of the completely packaged Multiport chip. After probe card alignment the probe card holder is tightened to the chip holder.

The IL for the two single photon wavelengths (channel #32 and #36) varies within $0.03dB$. Assuming a coupling loss of $0.75dB$/facet the propagation loss (PL) becomes

$$PL \approx (0.3 \pm 0.1)dB/cm,$$

with $\pm 0.1/cm$ representing the variation from chip to chip. The polarization dependent loss of a straight waveguide at 1550nm:

$$PDL < 0.01dB/cm.$$

Polarization dependence of the reflectivity of a beam splitter:

$$R_{Pol} \approx (R \pm 1.74)\%.$$

Measured temperature dependence of the reflectivity of a beam splitter:

$$R(T) \approx (R \pm 1.3)\%/K.$$

The reflectivity of the beam splitters on one chip depends on the position within the circuit and varies by:

$$\sigma_R \leq (R \pm 5)\%.$$

The drift is related to the position on the chip along the longer axis and seems to be related to the fabrication process being not perfectly uniform along the full 10cm of the chip. In principle, a drift can be compensated by asymmetric heating or cooling of the chip. However, this will not be necessary.

Loss of a beam splitter (DC):

$$L_{DC} \approx 0.5dB.$$

Loss MZI:

$$L_{MZI} \approx 1.7dB$$

IL of the Multiports:

$$\begin{aligned}
2 \times 2\text{MP}: \quad IL_B &\approx \quad 5.7dB \\
3 \times 3\text{MP}: \quad IL_T &\approx \quad 8.8dB \\
3 \times 3\text{MP}: \quad IL_Q &\approx \quad 11.1dB.
\end{aligned}$$

One problem which became apparent after characterization is the loss of the PDCs. The function of the path difference compensators is to introduce a path delay together with additional loss in order to compensate for other waveguides passing a MZI. However, this failed since PDCs overcompensate for a MZI. Compared to the MZI the PDC introduces an additional loss in the range of 1.5...2.1dB. No changes can be made after fabrication. In the next section, in order to put the 3×3 Multiport to test it will be combined with the in-fiber source of entangled qutrits.

5 Combining source and Multiport

The technical and experimental details of interfacing the qutrit source to the packaged Multiport will be discussed forming the last step before results and performance of the full setup will be presented in section 6.

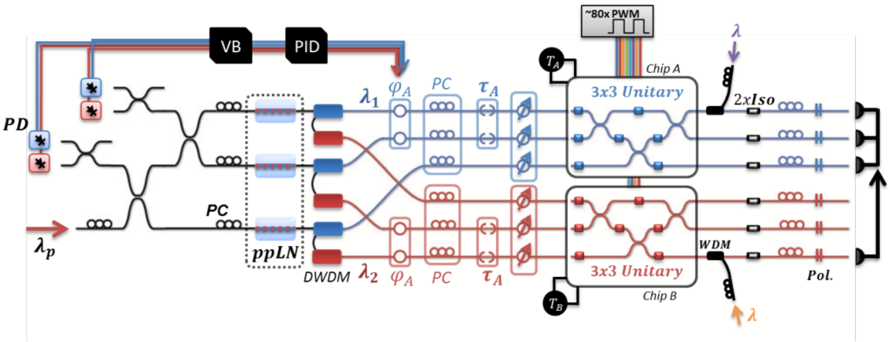

Figure 5.1: Sketch of the full qutrit setup.

The source (fig. 3.1) in section 3.2.2 has been expanded to four modes (ququarts). However, only the 3×3 Multiport connected to the qutrit subspace of the source will be examined due to time constraints. Fig. 5.1 shows the final setup. The integrated Multiport chip is replacing the fiber beam splitters of section 3.2.2. The fiber lengths have to be readjusted and the phase stabilization needs to be extended. This will be described in section 5.1. Fig. 5.1 outlines the experiment with focus on the optical path. The electric part and the control system will be considered in section 5.2. In section 5.3 the detection system is improved due to the introduced "high loss" Multiport chips.

5.1 Optical conciderations and adjustments

5.1.1 Arrival time and arm loss

The path encoded entangled qutrit source is interferometrically closed by connecting a Multiport to each qutrit. The length and loss differences are minimized similarly to section 3.2.3 and eq. 3.3. The length difference of modes (i, j) of qubit 1 has to be equal to the difference in length of the modes (i', j') of qubit 2:

$$\Delta_{1,2} = \Delta_{1',2'} \ , \ \Delta_{1,3} = \Delta_{1',3'} \ , \ \Delta_{2,3} = \Delta_{2',3'}. \tag{5.1}$$

Additional delay fibers will be introduced into the source before entering the Multiport. The fibers are prepared with a precision of $\pm 1mm$. Fine adjustments are performed using the variable optical delay line (τ in fig. 3.1). Eventually, the length differences are:

$$\begin{aligned}
\Delta_{1,2} - \Delta_{1',2'} &\leq (45 \pm 50)\mu m \\
\Delta_{1,3} - \Delta_{1',3'} &\leq (25 \pm 50)\mu m \\
\Delta_{2,3} - \Delta_{2',3'} &\leq (160 \pm 50)\mu m.
\end{aligned} \tag{5.2}$$

The same condition as eq. 5.1 is desirable for the loss (see section 3.2.4). The loss of each arm of the source has been measured as well as every input to the Multiport. The best combination has been chosen. Eventually, each arm pair has a combined loss of:

$$\begin{aligned}
L_{1,1'} = L_1 + L_{1'} = &\quad (21.6 \pm 0.1)dB \\
L_{2,2'} = &\quad (21.69 \pm 0.1)dB \\
L_{3,3'} = &\quad (22.12 \pm 0.1)dB \\
\Rightarrow \Delta L_{3,3'} = \Delta L_{2,2'} + 0.43dB = \Delta L_{1,1'} + 0.06dB.
\end{aligned} \tag{5.3}$$

The remaining difference in loss of $\leq 0.43dB$ will be compensated by the pump splitting ratios.

5.1.2 Phase requirements

The phase control will be changed since additional modes have been introduced to the source. Consider the qutrit setup, the pump beam is transmitted through the whole setup and all three modes interfere at the Multiport. The output signal detected behind the Multiport will show changes in intensity depending on all three paths. In principle, on can still calculate the phase change due to only one mode. However, three detectors observing all three outputs would be necessary and phase stabilization would require a total of 6 detectors. Furthermore, to trace back the initial phase change would involve the characterization of the Multiport at the pump wavelength for every unitary applied making phase stabilization unnecessarily difficult. Thus, a different scheme has been chosen.

The new scheme is shown in fig. 5.2. Two phase stabilization lasers of wavelength λ_A and λ_B are now used. They are inserted backwards into the setup into the output port of the Multiport. Both wavelengths are transmitted through the whole setup and interfere at the beam splitters used to split the pump beam. Then the two wavelengths are separated using a beam splitter and wavelength filter and are detected by a photo diode (PD).

The phase stabilization requirements will now be derived:

The state ψ before entering the Multiport is given by

$$|\psi\rangle \propto e^{i(\varphi_1+\varphi_{1'}+\varphi)}|11\rangle + e^{i(\varphi_2+\varphi_{2'}+\tilde{\varphi})}|22\rangle + e^{i(\varphi_3+\varphi_{3'})}|33\rangle. \tag{5.4}$$

Some unitary $U \otimes U$ is applied at the Multiports. If the unitaries have non-zero off-diagonal entries the phase becomes of importance. We will assume that the Bellport is applied U_{BP}. However, the following holds for any general unitary. For simplicity only the output pair $\langle 11|$ is considered:

$$\langle 11|U_{BP} \otimes U_{BP}|\Psi\rangle \propto e^{\varphi_1+\varphi_{1'}+\varphi} + e^{\varphi_2+\varphi_{2'}+\tilde{\varphi}} + e^{\varphi_3+\varphi_{3'}}. \tag{5.5}$$

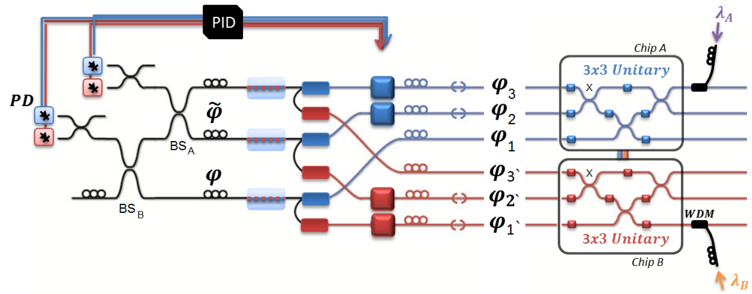

Figure 5.2: Sketch of the setup with focus on the important phases for phase stabilization. The two relative phases $\varphi_3 - \varphi_2$ and $\varphi_2 - \varphi_1$ ($\varphi_{3'} - \varphi_{2'}$ and $\varphi_{2'} - \varphi_{1'}$) define the state of qutrit A (B). The two relative phases correspond to two MZIs: the **inner MZI** is formed by one beam splitter of the Multiport (marked by "x") and BS_A, and the **outer MZI** formed by the Multiport and BS_B. The outer MZI includes the inner MZI in one arm due to the cascaded construction of the pump beam splitters BS_A and BS_B.

For a certain state, for example for maximum correlations $\left(|\langle 11|U_{BP} \otimes U_{BP}|\psi\rangle|^2 = 1\right)$, it follows that

$$\left|e^{\varphi_1+\varphi_{1'}+\varphi} + e^{\varphi_2+\varphi_{2'}+\tilde{\varphi}} + e^{\varphi_3+\varphi_{3'}}\right|^2 = 1$$
$$\Rightarrow \varphi_1 + \varphi_{1'} + \varphi = \varphi_2 + \varphi_{2'} + \tilde{\varphi} = \varphi_3 + \varphi_{3'}. \tag{5.6}$$

The latter condition has to be fulfilled using the two phase stabilization lasers λ_A and λ_B. The two stabilization lasers λ_A and λ_B acquire a phase relative to the pump laser $\varphi^{775} \approx 775nm$ of

$$\begin{aligned} \varphi_A = &\quad \varphi^{775} + \Delta_A, \\ \varphi_B = &\quad \varphi^{775} + \Delta_B. \end{aligned} \tag{5.7}$$

According to fig. 5.2 there are two MZIs for each phase stabilization laser. The first MZI will be called "inner MZI" and starts inside the Multiport, covers the modes $(2,3)$ and $(2',3')$, and ends at BS_A. The second MZI is formed by the Multiport, the modes $(1,(2,3))$ and $(1',(2',3'))$, and BS_B. It includes the phases of modes $(2,3)$ and $(2',3')$ of the inner MZI and will thus be called "outer" MZI . Using the two stabilization lasers λ_A and λ_B and the PID the inner MZI can be stabilized to a constant intensity implying constant phases:

$$\begin{aligned} c_A = &\quad \varphi_2^A + \tilde{\varphi}_A - \varphi_3^A \\ c_B = &\quad \varphi_{2'}^B + \tilde{\varphi}_B - \varphi_{3'}^B \end{aligned}$$

$$\Rightarrow c_A + c_B = \varphi_2^A + \varphi_{2'}^B + \tilde{\varphi}_A + \tilde{\varphi}_B - \varphi_3^A - \varphi_{3'}^B \tag{5.8}$$

$c_{A/B}$ are constant values. Using eq. 5.7, eq. 5.8 can be written as

$$c_A + c_B = \quad \varphi_2^{775} + \varphi_{2'}^{775} + 2\tilde{\varphi}_{775} - \varphi_3^{775} - \varphi_{3'}^{775} + \Delta_A + \Delta_B. \tag{5.9}$$

The wavelength of the two stabilization lasers will be symmetric around the pump wavelength of 775nm: $\Delta_A = -\Delta_B$. Thus, eq. 5.9 becomes

$$c_A + c_B = \varphi_2^{775} + \varphi_{2'}^{775} - \varphi_3^{775} - \varphi_{3'}^{775} + 2\tilde{\varphi}^{775}. \tag{5.10}$$

Above condition is sufficient to control the relation $\varphi_2 + \varphi_{2'} + \tilde{\varphi} = \varphi_3 + \varphi_{3'}$ of eq. 5.6.
Now, the part $\varphi_1 + \varphi_1' + \varphi$ of eq. 5.6 needs to be controlled relative to the other phases. Therefore, we will now consider the outer MZI. We will assume the inner MZI is stabilized and the phases $(\tilde{\varphi}, \varphi_2, \varphi_3)$ and $(\tilde{\varphi}, \varphi_{2'}, \varphi_{3'})$ are at a constant values. Following section 2.3.2 the phases of the inner MZI form a (global) phase $\varphi_{\text{inner}} = 1/2\,(\tilde{\varphi} + \varphi_2 + \varphi_3)$ for λ_A (and similarly for λ_B). φ_{inner} will be the phase of one arm of the outer MZI. Thus, stabilizing the intensity of the outer MZI leads to:

$$\begin{aligned} c_A' &= \varphi_1^A + \varphi^A - 1/2\left(\tilde{\varphi}^A + \varphi_2^A + \varphi_3^A\right) \\ c_B' &= \varphi_1^B + \varphi^B - 1/2\left(\tilde{\varphi}^B + \varphi_2^B + \varphi_3^B\right) \end{aligned}$$

$$c_A' + c_B' = \varphi_1^A + \varphi^A + \varphi_1^B + \varphi^B - 1/2\left(\tilde{\varphi}^A + \tilde{\varphi}^B + \varphi_2^A + \varphi_3^A + \varphi_2^B + \varphi_3^B\right) \tag{5.11}$$

Eq. 5.8 can be rewritten as

$$\varphi_3^A + \varphi_{3'}^B - c_A - c_B = \varphi_2^A + \varphi_{2'}^B + \tilde{\varphi_A} + \tilde{\varphi_B}$$

replacing the last term in brackets in eq. 5.11:

$$c_A'' + c_B'' = \varphi_1^A + \varphi^A + \varphi_{1'}^B + \varphi^B - 1/2(2\varphi_3^A + 2\varphi_{3'}^B).$$

The constant values have been absorbed into $c_{A/B}''$. Using eq. 5.7 the last equation can be expressed in terms of the single photon wavelength:

$$\Rightarrow c_A'' + c_B'' = \quad 2\varphi_1^{1550} + 2\varphi^{1550} + 2\varphi_{1'}^{1550} - 2\varphi_3^{1550} - 2\varphi_{3'}^{1550}. \tag{5.12}$$

Eq. 5.12 and eq. 5.10 allow to fulfill eq. 5.6. Therefore stabilizing the transmitted intensity of the two stabilization lasers allows to set the phase of the entangled state ψ. The wavelengths of the two lasers has to be symmetric in frequency around the pump wavelength (eq. 5.10). First the innermost MZI has to be stabilized followed by the outer MZI. In principle the scheme can be extended to any dimension (the number of phase stabilization lasers stays the same). Any noise within the inner MZI is directly transferred to the next MZI. Therefore, the error of the phase control scales directly with the dimension. Different stabilization schemes are imaginable where such a scaling is avoided. However, an extension of the setup to dimensions would likely integrate the source on-chip as well with no need for active stabilization.
In the experiment the wavelengths of the stabilization lasers are set to

$$\lambda_A = 765.25nm \text{ and } \lambda_B = 785.00nm.$$

The two wavelengths passing each Multiport seem to be partly guided by the waveguides but are also scattered through the chip in an uncontrolled but deterministic way. Depending on the input channel and Multiport setting the light can be attenuated by up to 30dB. If the Multiport is changed the transmittance behavior changes as well. Therefore, if the Multiport is changed the characterization of the stabilization laser and the coincidence signal is repeated. Since the visibility of the outer MZI depends on the relative phases of the inner MZI the characterization has to be repeated for the outer MZI if the phases of the inner MZI are changed (although in principle computable and compensable). The two wavelengths are inserted using two WDMs. The photo detectors are placed at the unused inputs of the cascaded beam splitters used for dividing the pump beam.

5.1.3 PID phase control

Here, the process leading to the stabilized control of all phases using the PID will be described. Initially, the characterization between pump phase and single photon correlation signal of every pair of modes needs to be performed. There are two phase stabilization lasers with two wavelengths each for stabilizing the pair of modes for one of the two photons. The purpose of the characterization is to find the relation $\varphi_{765} \longleftrightarrow (\varphi_{1550})$ for photon A and $\varphi_{785} \longleftrightarrow (\varphi_{1550})$ for photon B. For simplicity, we will now only consider photon A, however, the same is true for photon B. The intensity at the fW detector is given by

$$I_{765} = sin^2\left(\varphi_{765}\right) \Rightarrow \varphi_{765} = arcsin\left(\sqrt{I_{765}}\right). \tag{5.13}$$

If the PID stabilizes the signal to a certain amplitude P (given in percent) at a certain fringe F^2 then φ_{765} is given by the (μ-controller code friendly) formula

$$\varphi_{765}(F,P) = (-1)^{F+1}\ \left(P - \left(2 - (-1)^{n>>1}\right)\frac{\pi}{2}\right).$$

The operation ">>" is a bit shift, details can be found in [53]. The coincidence correlation signal depending on the pump phase has the form

$$CC_{\varphi_{765}} = a + b\ sin^2\left(-c\varphi_{765} + d\right). \tag{5.14}$$

The parameters a and b define the offset and amplitude of the interference signal. Similarly for φ_{1550} the coincidence correlation signal is of the form

$$CC_{\Delta\varphi_{1550}} = \alpha + \beta\ sin^2\left(\varphi_{1550}/2\right) \tag{5.15}$$

with α being the offset of the signal (for example due to noise and accidentals) and β representing twice the intensity amplitude of the correlation. The visibility can directly be calculated from those two parameters. Assuming eq. 5.15 as proportional to eq. 5.14 yields the relation $\varphi_{765}\left(\varphi_{1550}\right)$:

$$\varphi_{765} = \frac{1}{c}\left(d - \frac{\varphi_{1550}}{2}\right). \tag{5.16}$$

[2] refers to the 4 parts of a $sin(x)$ function within $x = 0...2\pi$ in which the slope has the same sign.

Therefore, for a full characterization the coincidence signal is recorded for a sequence of changing (F,P) values. While channel φ_{765nm} of photon A is scanned the phase φ_{785nm} of photon B is kept constant. The resulting signal $CC\left(\varphi_{765} - \varphi_{785}^{const}\right)$ is subsequently fitted using eq. 5.14. The constant phase φ_{785nm} appears in eq. 5.16 as the phase offset (parameter d). From the best fit parameters the visibility is obtained and the relation is defined $\varphi_{765}\left(\varphi_{1550}\right)$ using eq. 5.16. The resulting fit parameters can be used for the phase of photon B φ_{785nm} as well. Thus, after the characterization the system can be set to the desired phases φ_{1550}^{A} and φ_{1550}^{B}. If a list of different phases should be measured in sequence it can happen that one of the phases will lie close to an intensity maximum of the phase stabilization signal $\varphi_{785/765}$ and therefore can hardly be stabilized. In those cases a subprogram can add phase global offsets to all phases effectively "moving" the phase away from a maximum or minimum (see Appendix). Details can be found in the thesis by Polster [53].

In the case of $N > 2$ during characterization there are more than 2 phases (or more than 1 relative phase) contributing to a coincidence signal. Therefore, if the inner MZI in fig. 5.2 is characterized a signal of amplitude 2π and a frequency of 50Hz is applied to the outer path corresponding to the outer MZI. Following section 2.6, the 50Hz signal is faster than the detection integration time and effectively removes the dependence of the coincidence signal from the outer mode.

Maximizing the interference signal the PID receives is of great importance for the precision and noise reduction of the stabilization. For this purpose another device called "Visibility Board" (VB) has been developed. The VB manipulates the output signal of the photo diode (PD) before sending it to the PID for phase stabilization. By receiving the command it automatically maximizes the visibility of the electric output signal of the PD by electrically subtracting and amplifying the photo diode voltage signal. All channels are processed in the same way. Starting at a common visibility of $V \approx 20\%$ the VB improves it by a factor of ≈ 3 to $V' \approx 80\%$. Of course, this process introduces noise into the signal. However, almost always is the improvement in visibility is greatly compensating for it.

5.2 Electric control

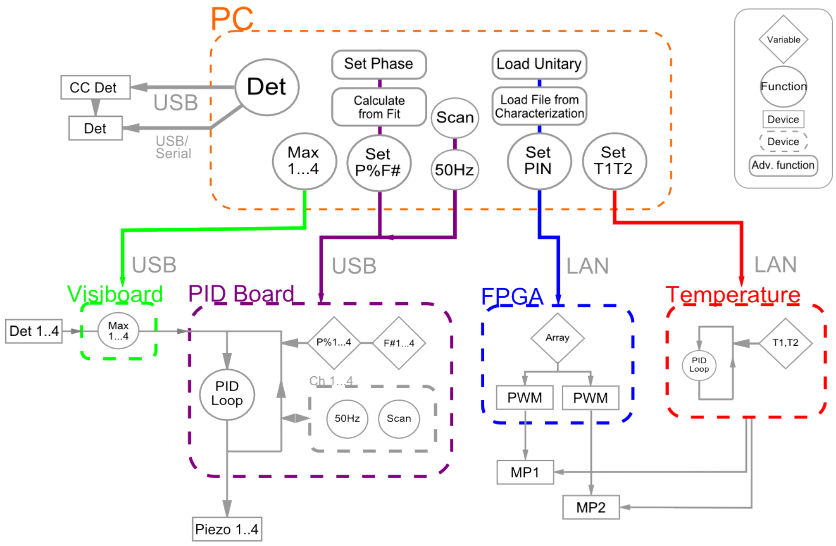

Figure 5.3: The VB (green) optimizes the electric signal for the PID (purple) for phase stabilization. The temperature stabilized (red) Multiports are controlled using an FPGA (blue).

In fig. 5.3 an overview of the electric control system is presented. In the following sections the important functions will be described. In section 5.2.1 the driving of every phase shifter on the Multiport as well as the temperature control is discussed. Section 5.2.2 briefly describes how each MZI and phase shifter of the Multiport is individually characterized. Some quick calculations estimating the tolerances of setting the Multiport regarding perfect correlations will be presented in section 5.2.2. Eventually, the full process for performing an experiment is outlined in section 5.2.3.

5.2.1 Basic Multiport control

For the on-chip heaters to perform a full 2π phase shift a power of

$$P_{2\pi} \approx 60mW \quad R \approx 180\Omega$$

is required. Separate driving of such a high number of phase shifters is problematic from a logistic and cost standpoint. The solution is to use the relatively slow response time of a thermo-optic phase shifter

$$\tau \approx 10ms.$$

A field programmable gate array (FPGA) module is driving 8 digital modules supplying a total of 80 separately controllable pulse width modulated (PWM) channels . The driving frequency has been chosen to be at

$$f_{PWM} = 40\text{kHz}$$

with a duty cycle resolution of 12bit (4096 steps). The duty cycle is the amount of time the PWM signal stays in active state relative to the total time of the clock. The frequency is a compromise between resolution and the requirement that $f_{PWM} >> 1/\tau \approx 1/10ms = 100Hz$. For this purpose the PWM frequency response of a $1550nm$ cw laser transmitted through the Multiport and detected by a fast photo detector has been recorded. The PWM frequency has been chosen such that no influence on the 1550nm signal is detectable and according to section 3.2.4 no measurable reduction in visibility is expected ($V > 99.99\%$). The high (low) level of the PWM is set to $U_{high} = 4V$ ($U_{low} = 0V$) chosen such that a phase shift $> 2\pi$ is possible for every phase shifter on the chip.
All PWM channels are driven by an FPGA which is controlled by the PC. Details on how to explicitly access each Multiport pin are described in the appendix.
Both Multiport chips are separately temperature stabilized using an independent micro-controller based PID circuit controlled by the PC.

5.2.2 Automated characterization

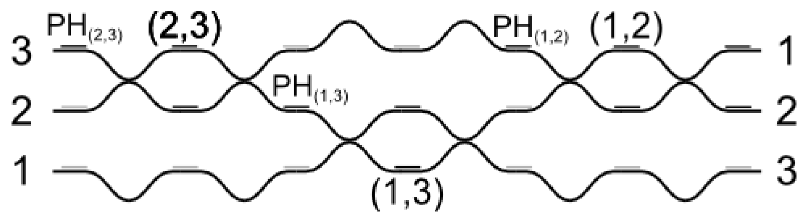

Figure 5.4

In principle, by inserting light into the different inputs of the Multiport and observing different outputs the real parts of the unitary matrix can be measured. Inserting light phase stable into two inputs every relative phase is measured leading to the phases of the Multiport. Every $N \times N$ unitary transformation can be replaced by a Multiport of appropriate setting. Thus, any unitary transformation can be characterized in the described way independent of the actual internal structure.
The Multiport is thus characterized in the following way:
Iteratively every Mach-Zehnder interferometer of the Multiport is characterized by recording the transmitted intensity I as a function of the PWM duty cycle d: $I(d)$. Any internal phase will be part of some MZI-type circuit and can be characterized in the same way. CW light at 1550nm is inserted into different Multiport inputs and detected using a normal photo detector at the outputs. Inserting light into input 1, MZI(1,3) and MZI(1,2) are characterized at output 3 and 2 (the reflective setting, see section 2.3.3). Inserting light into input 3, MZI(2,3) can be characterized at output 3. The inner phases $PH(1,2)$ and $PH(1,3)$ are characterized via the MZI formed by MZI(2,3) and MZI(1,2). The (global) output phases are not relevant, the input phases will be characterized later. This system can, of course, be generalized to any dimension. In principle the structure of the Multiport does not need to be known: scanning a phase a fringe will become visible at at least two outputs allowing for a characterization. Using the active

phase shifter greatly simplifies the reconstruction of the Multiport. In comparison the unitary reconstruction of an unknown passive circuit [85, 86] is more difficult.
Knowing the maximum and minimum intensity, $I(\varphi)$ corresponding to a certain phase shift is calculated via

$$I(\varphi) = (I_{max} - I_{min})\, Sin^2(\varphi). \tag{5.17}$$

The recorded intensity dependance on the duty cycle $I(d)$ using eq. 5.17 yields $d(\varphi)$ and completes the characterization. Here, measuring I_{max} and I_{min} at the reflective side of the MZI becomes crucial (section 2.3.3). As will be discussed later, due to heating of the Multiport, temperature drifts, and electric crosstalk the phase shifter slightly change values if another heater is switched on. Hence, the Multiport characterization is repeated until the desired precision is reached. Two iterations have been sufficient within this work.
A program automatically performs what has been described in this section (see Appendix). For any desired setting of the Multiport the values are recorded and saved to a text file. Another program will later access these files and set the Multiport accordingly.

Predictions

Before the integrated realization of the Multiport was considered different calculations have been performed in order to estimate the necessary precision on the internal phases and reflectivities. For example, a Monte-Carlo simulation was performed assuming errors in all internal phases $\delta\varphi$ and reflectivities δR randomly distributed using a normal distribution of the error with a standard deviation of σ. For each set of error values > 10000 runs have been performed. The probability of the maximum perfect correlation averaged over all three bases serves as the measure of quality. The mean over all runs > 10000 corresponds to one point in fig. 5.5. As can

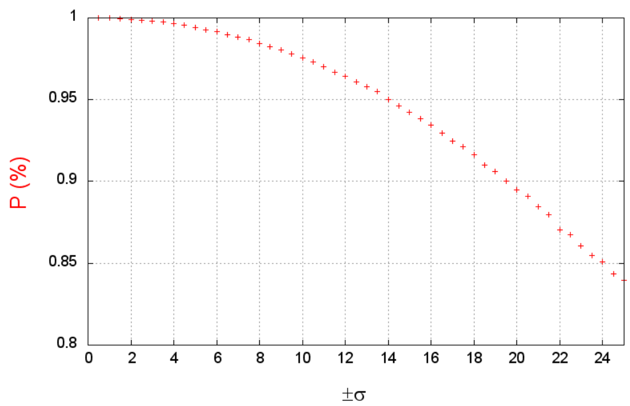

Figure 5.5: Monte-Carlo result of the reduction of the probability of observing a perfect correlation averaged over all three basis (MUBs). The reduction in the probability of observing the maximum perfect correlation is due to every phase shifter and reflectivity inside the Multiport having a random deviation of $\delta\varphi = \sigma$ and $\delta R = \sigma$ for both qutrit Multiports.

be seen in fig. 5.5 the quality of perfect correlations is not very sensitive. Even for the assumption of a relatively high error the average reduction in the maximum correlation probability P_{red} is estimated to only:

$$\begin{aligned} \delta\varphi = \pm 5\%\pi, \quad \delta R = \pm 5 \quad &\rightarrow \quad P_{red} = 99.4\% \\ \delta\varphi = \pm 2.5\%\pi, \quad \delta R = \pm 2.5 \quad &\rightarrow \quad P_{red} = 99.9\% \end{aligned} \tag{5.18}$$

The sensitivity of the setup to phase and reflectivity variations therefore seems manageable. We aim at a phase precision of $\pm 1\%$.

5.2.3 The measurement sequence

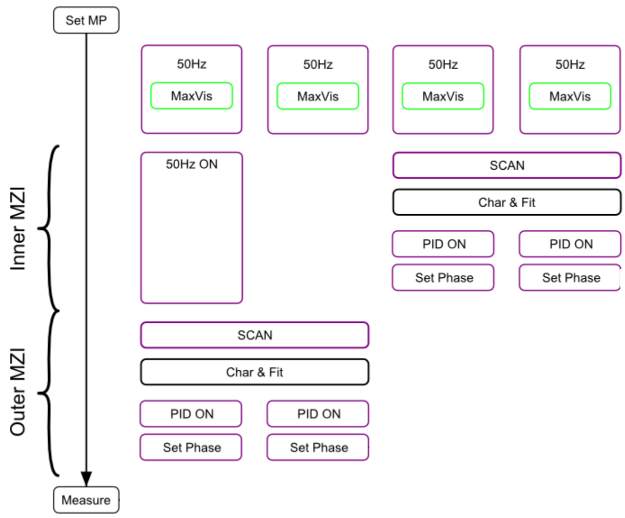

Figure 5.6: Sequence of characterization and measurements to perform an experiment. Starting at setting the Multiport to a certain unitary (top) and ending at a single photon detection measurement (bottom). The four columns represent one of the four relative phases of the entangled qutrit system. After the Multiport has been activated to display a certain unitary transformation the VB maximizes the visibility. Then the inner and outer MZI of the system are individually characterized. The PID scans, characterizes and fits the correlation signal for each MZI and afterward sets the phases to the desired values. Eventually, single photon detection completes a measurement.

Fig. 5.6 illustrates the full sequence of an experiment beginning at setting the Multiport to a particular transformation and ending at a measurement. First the MP is set to a unitary transformation ($200ms$) followed by the PID applying a 50HZ signal to all channels for the VB to maximize the visibility ($\approx 3-5s$ depending on initial visibility). Now, the interference signal of the inner MZI is isolated by applying a 50Hz signal to the outer modes. The PID scans the maximum and minimum for later reference ($\approx 2s$) and the characterization can start. Depending on the desired precision, number of measurement points, and integration time the process takes approximately $1min$ (4 Fringes each 4 points with 4s integration time: $4\times4\times4s = 64s$). Once the relation between coincidence signal and phase is known it can be set to any value (50ms...150ms depending on the distance to the current position of stabilization). The same process is repeated for the outer MZI. Once all phases are set a measurement can be completed. Eventually, the

phases of the outer MZI can be changed again (50ms...100ms) immediately followed by another measurement. If a phase of the inner MZI has to be changed the visibility of the outer MZI will change and therefore has to be characterized again.
In principle the characterization does only need to be performed once although the visibility changes when the Multiport or inner phase setting is changed. Once the maximum and minimum of the correlation fringe for characterization is known two measurement points are enough to reveal the current slope of the fringe the PID is stabilizing on. The phase therefore can be set after two (6s) characterization measurements. In principle, the PID can be shortly switched off, the Multiport changes its setting, and the PID is switched on again stabilizing at the current position of the signal. Because the change of the Multiport setting is fast (100ms) compared to the phase change ($\approx$ min) the stabilization can continue. This has been initially tested. However, all measurements, so far, did not crucially depend on a fast switching time of the Multiport.

5.3 Detection

In general, single photon detection for Telecom wavelengths especially in the C- and L-band has been problematic. Silicon based avalanche photo diodes (APD) have a quantum efficiency (QE) of around 50% in the visible spectrum. However, the QE is rapidly decreasing towards the near infrared reaching approximately 0.1% at $1064nm$ [87]. For this reason different materials have been considered. Main attention has been paid to Indium Gallium Arsenide (InGaAs) as it offers a high absorption coefficient at Telecom wavelengths, low excess noise, and a high bandwidth. Moreover, with a bandgap energy at room temperature of 0.75eV it is perfectly suited for C- and L-band operation with a range of about 900nm to 1700nm [88].
The fundamental principle of an APD is the photoelectric effect creating charge carrier triggering avalanche current at a reverse biased p-n junction. For a high gain the APD is operated outside of the linear amplification regime well above the breakdown voltage in the so-called Geiger Mode. For distinction to a normal APD it is consequently called single photon avalanche diode (SPAD). The higher the reversed bias voltage (U_{RB}) above the breakdown voltage (U_B) called excess Voltage (U_E) the higher the quantum efficiency (QE) and the better the timing resolution of the produced avalanche pulse [87]. Operation above breakdown voltage means that one injected single carrier can trigger a self-sustained exponential increasing avalanche current. For this reason a quenching circuit has to be utilized: after a trigger event the reversed bias voltage (U_{RB}) is lowered below the breakdown voltage (U_B). The avalanche effect ceases and the voltage is returned to the operation above breakdown. This process takes some time during which no further event can be detected. This so-called dead-time causes saturation effects with the saturation limit decreasing with increasing dead-time (t_{dead}). Even in the absence of light the SPAD will trigger due to thermally generated carriers similar to the dark current in ordinary photo diodes. This so-called dark count rate increases with U_E. During an avalanche some carriers are captured by deep levels in the depletion layer of the p-n junction. They are subsequently released with a fluctuating delay. This causes so-called after-pulses which are correlated with the previous avalanche pulse. The number of after pulses increases with the total number of carriers and the number of thermally induced carriers which again increases with U_E. The problem of after

pulses can be reduced by the quenching circuit by keeping the bias voltage below the breakdown voltage for an additional hold-off time. A hold-off time much bigger than the release rate of the trapped charges dramatically reduces the number of after pulses. The trap release rate decreases with temperature and can greatly limit the detection speed [89]. For this reason, free-running operation of InGaAs detectors is hardly possible and gated operation has been preferred where the gate off time is bigger than the trap release rate. In this experiment a triggered or gated detection scheme is used. However, recently, increasing improvements in the quenching circuit have further pushed the gating frequencies to higher rates up to $100MHz$ and have even resulted in reduced after pulse probabilities and dark count rates in free-running operation [50, 90].
It should be noted, there are, of course, other methods researched for high efficient single photon detection. Such as super-conducting nanowire single-photon detectors [91], transition edge sensors [92], or quantum dots [93]. Especially transition edge sensors (TES) have attracted a wide interest since they offer unprecedented detection efficiencies and dark count rates. However, in this work SPADs have been chosen although they are supersede by other methods in QE and noise. A main advantage compared to the above mentioned method is their commercial availability. The other methods are still a topic of research and can not be considered as a out-of-the-box tool. Often cryogenic operation is required and the signal requires further processing. Commercial SPADs on the other hand are compact tested devices delivering data with standard communication protocols at a small form factor. This especially is important, if the topic of research is not the detection but the development of a setup for entangled quNits where 2N detectors are required.

5.3.1 Detection scheme derivation

Consider a source producing N_0 pairs per second. Detector 1 (2) has a loss of $\eta_{1(2)}$ and a QE of $q_{1(2)}$. Detector 1 is triggered at a rate ν_T with a gate opening time of τ_g. If a photon is detected a dead time τ_d is introduced and detector 2 is triggered waiting for a coincidence photon within the timing window τ_{cc}. If $1/\tau_d << \nu_T$ is negligible the detected singles S_1 at detector 1 will be $S_1 = \nu_T \tau_g \eta_1 q_1 N_0$. If τ_d is not negligible the trigger at rate ν_T of detector 1 will sometimes fall into the dead time τ_d. The number of trigger events depends on the number of singles S_1 and the number of a dark counts D_1 occurring within the gating window τ_g at a dark count rate DR_1. Therefore, the trigger rate and the number of detected singles and dark counts will be effectively reduced to

$$\nu_{eff} = \frac{\nu_T}{1 + \tau_d(\tau_g D_1 + S_1)}$$

$$S_1 = \nu_{eff} \tau_g \eta_1 q_1 N_0 \quad , \quad D_1 = \nu_{eff} \tau_g \mathrm{DR}_1. \tag{5.19}$$

After detector 1 detects a single photon, detector 2 will be triggered detecting the partner photon with a probability of $\eta_2 q_2$. The number of detected coincidences (CC) becomes

$$CC = \eta_2 q_2 S_1. \tag{5.20}$$

However, accidental coincidence events can be detected due to any combination of detection events DC-Singles, DC-DC, Singles-Singles, Singles-DC. Detector 2 will therefore show an accidental coincidence count (ACC) of

$$ACC = \tau_{cc} D_2 (S_1 + D_1) + \tau_{cc} \eta_2 q_2 N_0 (S_1 + D_1).$$

The signal-to-noise (SNR) therefore becomes

$$\begin{aligned} SNR =& CC/ACC \\ =& \frac{1}{\tau_{cc}} \frac{\eta_1 \eta_2 q_1 q_2 N_0}{\eta_1 q_1 N_0 DC_2 + DC_1 DC_2 + \eta_2 \eta_1 q_2 q_1 N_0^2 + \eta_2 q_2 DC_1 N_0}. \end{aligned} \tag{5.21}$$

At high brightnesses $N_0 >> DC_{1/2}$ the SNR will thus decrease with increasing brightness due to two photons from different pairs being counted as a coincidence (term $\eta_2 \eta_1 q_2 q_1 N_0^2$ in eq. 5.21). For low brightnesses where N_0^2 can be neglected the SNR will increase linearly mainly due to dark counts:

$$SNR \propto \begin{cases} \frac{1}{\tau_{cc}} \frac{\eta_q \eta_2 q_1 q_2 N_0}{DC_1 DC_2} & \text{for } N_0 << \{DC_1, DC_2\} \\ \frac{1}{\tau_{cc}} \frac{1}{N_0} & \text{for } N_0 >> \{DC_1, DC_2\} \end{cases} \tag{5.22}$$

Therefore, for a certain brightness the SNR will reach a maximum. From eq. 5.21 it follows at the maximum:

$$\eta_1 q_1 N_0 \cdot \eta_2 q_2 N_0 = DC_1 \cdot DC_2. \tag{5.23}$$

If at each detector the dark counts DC are equal to the number of detected singles $\eta_1 q_1 N_0$ the maximum SNR will be reached. Note, that the singles displayed by the detector, however, are reduced by the effective trigger rate. Therefore, the detected singles to dark count ratio will be a bit lower than 1 (eq. 5.19).

As long as dark counts can be neglected the SNR does not depend on the loss (eq. 5.22). Therefore, in this case, additional loss $\eta_1 + \delta\eta_1$ does only decrease the coincidence count rate while the SNR stays constant. This scenario is the case at low dead times due to low after pulse probabilities and dark count rates. For example, for VIS single photon detectors a dark count rate of $< 100 DC/s$ down to $2 DC/s$ [50] and a dead time of only 50ns [50, 94] is typical for commercial devices.

If, however, this condition is not met, the SNR will decrease with increasing loss ($\delta\eta_1$) due to dark counts (eq. 5.21). Increasing the brightness N_0 will even further decrease the SNR due to an quadratic increase in the accidental rate. This will be the case for most single photon detectors at the Telecom wavelength where high dark count rates of $1000 DC/s$ and a dead time of $100\mu s$ have been typical for commercial devices (excluding very recent developments).

5.3.2 Qubit detection scheme

For the entengled qubit source in section 3.2.3 two IDQuantique detectors (IDQ) have been used. From eq. 5.21, 5.20, and 5.19 the SNR can be estimated when a loss (such as the MP) is introduced in both arms $\eta_{1/2}$ shown in the left graph of fig. 5.7. The presented dependence has been experimentally verified using one crystal (by unplugging the other) of the qubit source and introducing different fixed loss attenuators into the setup.

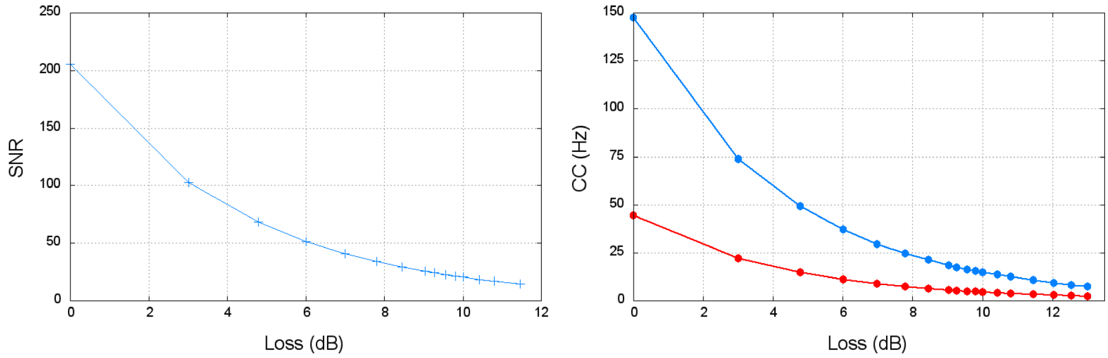

Figure 5.7: **Left:** Estimated reduction of the optimal SNR (eq. 5.23) with varying loss at η_1 and η_2. **Right:** Coincidence count rate at optimal SNR (blue) and half of optimal SNR (red).

Following the left graph of fig. 5.7, introducing a MP with a loss of $\approx 12dB$ would reduce the optimal SNR to 12.8. However, at optimum SNR according to Eq. 5.20 a coincidence rate of only $\approx 2.8CC/s$ would be obtained (right graph of fig. 5.7). In a measurement the given coincidence rate would be divided over all crystals and only appear in the correlation maximum. For good Poissonian counting statistic and a relative error of, for example, 5% an increased detection integration time of approximately 2.4min per measurement point would be required. Therefore, a different detection scheme had to be developed before extending the qubit source.

5.3.3 New detection scheme

While the qubit source was extended, at the same time, the Austrian Institute of Technology (AIT) [90] was developing a novel SPAD based detector in the free running regime with low dark count rates and low after pulsing probabilities using a fast active quenching circuit. The specifications had been estimated to a dead time of $5\mu s$ and 350ps timing resolution at 10%QE. Typically, under normal operation at QE of below 5% the after pulse probability can be as low as 3% at a dark count rate of on the order of $100DC/s$. Especially the reduced dead time promised a significant advantage compared to the IDQ detectors. As described in section 5.3.2 the increased loss causes an dramatic decrease in detected coincidences due to the long dead time and is further limited by the effective gating frequency ν_g. Therefore, in collaboration with the AIT the prototype detectors have been directly tested and characterized within the qubit source. Some results are presented in [95]. The detectors are now commercially available [96].

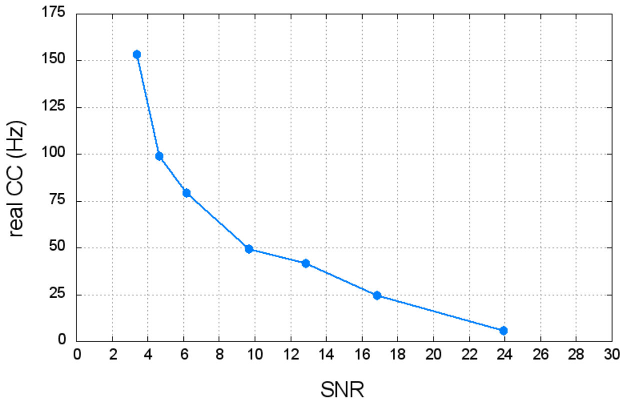

Figure 5.8

Different tests have been performed including different detection schemes and combinations of detectors from AIT and IDQ searching for the optimal setup for the extended source. As a result the optimal scheme has been identified to be a AIT detector triggering an IDQ detector. Here, the low dead time and low dark count probabilities of the AIT detector together with the low gating window of 2.5ns of the triggered IDQ detector produce the best results. At a SNR of 10 one obtains a rate of $50CC/s$. Thus, for a relative Poissonian noise error of 5% a measurement time of $t_{5\%} = 5s$ is required. Compared to the required 2.5min using two IDQ detectors described in the previous section:

$$\begin{aligned} t_{5\%}^{AIT\to IDQ} &= \quad 5s \\ t_{5\%}^{IDQ\to IDQ} &= 2.5min \end{aligned} \tag{5.24}$$

a major improvement by a factor of 30 is achieved.

The setup is completed. The following section will present the results of various measurements.

6 Results

Results of different measurements of the complete setup will be presented. First, in section 6.1 the Multiport will be further characterized with regard to its main purpose: the realization of any unitary transformation. Section 6.1.5 will introduce a method of visualizing the performance of the Multiport in the abstract unitary space. The quality of all qubit subspaces of the qutrit setup will be estimated with various measurements in section 6.3. Section 6.4 presents some measurements in the full entangled qutrit space including a full scan and analyzation of the correlation space (section 6.4.1) and the observation of the different types of perfect correlations (section 6.4.2).

6.1 Multiport performance
Realization of any unitary transformation

6.1.1 MZI characterization

The basic properties of the Multiports have been presented in section 4.6. Now, the performance of more advanced functions of the Multiports are of interest. All phase shifters have been completely characterized. The typical worst case of the different specifications will be given measured for multiple Multiport chips. All chips are stabilized at a temperature of $20.5°C$. The duty cycle at 12bit has values from 0 to 4048 corresponding to a duty cycle of 0% (off) to 100% (on). From all tested Multiport chips, two Multiports have been chosen. They will be labeled 2.12 and 2.13 .

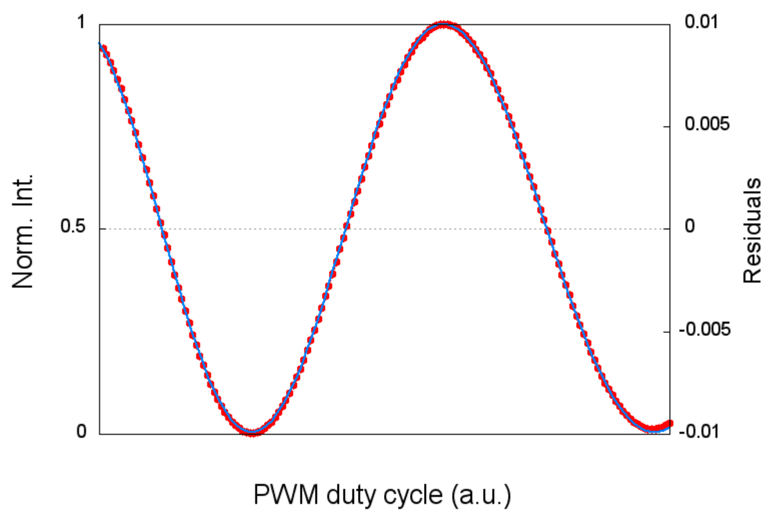

Figure 6.1: Transmitted normalized intensity of an on-chip MZI inside the Multiport at different PWM duty cycles. The red line is a best nonlinear fit of the form $a + b\ Sin(cx^2 + dx + e)^2$. The term cx^2 cannot be neglected. The reason for the quadratic term might be the non-zero rise and fall time of the PWM signal, or the non-linear thermo-optic phase shift dependence.

Fig.6.1 shows a typical fringe when scanning a MZI on the MP by applying a PWM signal onto one inner phase shifter and monitoring the transmitted intensity. Fig.6.1 allows to calculate the internal phase difference between both paths of the MZI when no heater is activated. Tab. 6.1 presents the results for the two 3×3 Multiports.

MZI PIN	φ_0
a7	$(0.24 \pm 0.01)\pi$
a5	$(0.21 \pm 0.01)\pi$
a3	$(0.22 \pm 0.01)\pi$
A7	$(0.21 \pm 0.01)\pi$
A5	$(0.22 \pm 0.01)\pi$
A3	$(0.22 \pm 0.01)\pi$

Table 6.1: Calculated intrinsic phase difference of all Tritter MZIs of Multiports #2.12 and #2.13. There is no fundamental reason for the high error. The phase difference simply has not been of concern for the automated characterization.

According to tab. 6.1 the average phase difference $\overline{\varphi_0}$ can be achieved with an effective optical path difference d_{eff} of

$$d_{eff} = (1.38 \pm 0.06)\lambda_{1.55\mu m} = (2.14 \pm 0.10)\mu m.$$

The path difference is to be compared to the MZI geometry with an arm length measured from the centers of the beam splitters of $\approx 9.4mm$.

	MP2.12		MP2.13	
	$V_1(\%)$	$V_2(\%)$	$V_1(\%)$	$V_2(\%)$
(1,2)	96.1 ± 0.3	99.0 ± 0.2	90.8 ± 0.6	99.8 ± 0.1
(1,3)	98.6 ± 0.3	99.0 ± 0.3	88.0 ± 0.7	99.7 ± 0.1
(2,3)	99.4 ± 0.3	99.6 ± 0.2	85.6 ± 0.7	98.7 ± 0.2

Table 6.2: Extinction ratio of the three MZIs of the two 3×3 Multiports 2.12 and 2.13. Although MP2.13 exhibits a significantly lower visibility it has been chosen over other Multiport chips due to its lower loss.

Tab. 6.2 shows all measured visibilities for both outputs of every MZI of the two 3×3 Multiports. Using Eq.2.18 each MZI can be further characterized. Tab. 6.3 presents the resulting beam splitter imbalances (Eq.2.18) for every MZI. The arms of each MZI are assumed to be of equal loss ($\Lambda = 0dB$).

	MP2.12		MP2.13	
	$d_1(\%)$	$d_2(\%)$	$d_1(\%)$	$d_2(\%)$
(1,2)	50.0 ± 3.6	50.0 ∓ 10.5	50.0 ± 9.5	50.0 ∓ 12.5
(1,3)	50.0 ± 0.8	50.0 ∓ 7.6	50.0 ± 10.8	50.0 ∓ 14.4
(2,3)	50.0 ± 0.5	50.0 ∓ 5.0	50.0 ± 10.1	50.0 ∓ 17.6

Table 6.3: Imbalances $d_{1/2}$ of the beam splitters for both used Multiports. Note, according to eq. 2.18 on can neither identify which beam splitter has which offset away from 50% nor which sign: $50 \pm d_{1/2}$ or $50 \mp d_{1/2}$.

Tab.6.2 reveals a drift of the visibility of the MZIs over the length of the chip. The same drift will be inferred on the beam splitter imbalances in tab.6.3. MP2.13 contains relatively high imbalances. Nevertheless, the circuit has been picked due to low insertion loss. Fig.6.2 shows the results of tab.6.3 displayed graphically.

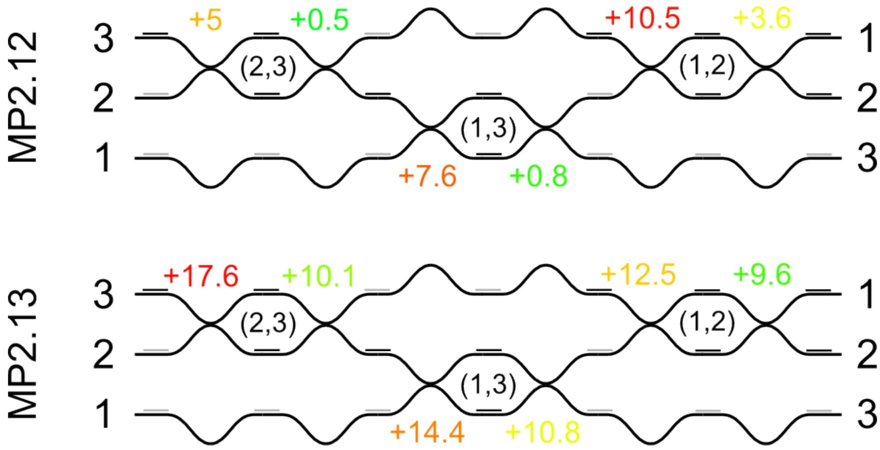

Figure 6.2: Imbalances δ of the beam splitters $(50.0 + \delta)\%$ taken from tab.6.3. $d_{1/2}$ are chosen such that it would be consistent with a drift over the chip.

Fig. 6.3 presents the regions of interest during a typical characterizing of a MZI on the MP by applying a PWM signal onto one inner phase shifter and monitoring the transmitted intensity.

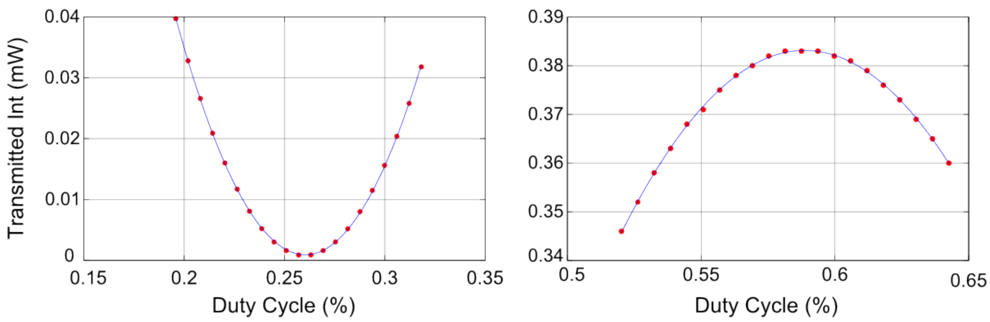

Figure 6.3: **Left:** Minimum transmitted intensity of an on-chip MZI inside the Multiport. **Right:** Maximum transmitted intensity. Extreme points are automatically extracted via a nonlinear fit (blue line).

The maximum and minimum of transmission of the fringe are automatically fitted and the visibility is calculated. In order to obtain a desired value of the reflectivity the maximum/minimum values are used to calculate the corresponding intensity. The same is done for every MZI on the chip and every internal phase. Eventually, the desired unitary matrix is obtained. The precision and repeatability in finding the minimum and maximum intensity (I) at the corresponding duty cycle frequency (d) depends on different factors such as the error of the fit, or the precision of the PWM control. A laser light at $1550nm$ is inserted into the Multiport and detected using a power meter connected to the output. The maximum errors for a typical characterization amount to

$$\delta I_{max} < |\pm 0.15\%| \ , \ \delta I_{min} < |\pm 14.30\%|$$

given in percent relative to the maximum (minimum) intensity. The position of the maximum (minimum) at a certain duty cycle d_{max} (d_{min}) can be determined within a range of the duty cycle δd to

$$\delta d_{max/min} < |\pm 0.1\%| \, .$$

The precision in setting the MZI to a certain value depends on the value itself due to the $Sin^2(\varphi)$ dependance. Setting a MZI to 50% reflectivity, a repeatability of the reflectivity of

$$\delta R^{50\%}_{max/min} < |\pm 0.5\%|$$

and

$$\delta d^{50\%} < |0.05\%|$$

is achieved, with the error approaching $\delta d_{max/min}$ for $R \longrightarrow 1$ or $R \longrightarrow 0$. However, the given values exclude temperature drifts which will be subject to the next section.

6.1.2 Thermal control and other influences

During characterization of the Multiport chips it became apparent that activated phase shifters cause a temperature increase of the full chip and therefore influence all other phase shifters. The effect has been minimized during fabrication by isolating the phase shifting regions and thereby avoiding direct heat diffusion to neighboring waveguides. Furthermore, Silicon as the base material is strongly thermally conducting compared to Silica (Si: $124W/mK$, fused Silica: $2W/mK$, both at room temperature[3]). Therefore, the base Silicon material is acting as a heat sink. However, there is still a measurable effect. At room temperature, activating 40 heaters will increase the chip's temperature up to $\approx 32°C$ (isolating chip holder, surrounded by air).
A second chip holder has been developed [53]. It is build from Copper with a good thermal conductivity. In the middle of the holder 0.1mm below the bottom of the Multiport chip a PT1000 and thermoelement temperature sensors are placed. Any specified temperature of the Multiport refers to the temperature measured by the thermoelement (precision $\pm(0.05\% + 0.3°C)$). The Chopper holder is placed on top of two peltier elements for cooling. A PID micro-controller is

[3]Taken from www.matweb.com, 07.2013

stabilizing the signal using the PT1000. A thermal stability of

$$\Delta T = \pm 0.03°C$$

at a steady MP setting is achieved. During characterization the temperature stays within $\leq \pm 0.07°C$. Switching the Multiport from all phase shifters turned off to the Bellport setting the temperature stays within $\pm 0.75°C$.
The position (duty cycle frequency $d^{50\%}$) of the MZI at a reflectivity of 50% (the highest sensitivity, highest slope of sin^2) is measured with respect to different chip temperatures. The **highest temperature sensitivity** has been determined to

$$\frac{d(d^{50\%}_{A5})}{dT} = +0.69\% \frac{1}{°C}.$$

For example, assuming the 50% reflectivity value is at 40% of the duty cycle at $20°C$, at a temperature of $21°C$ the 50% value will be found to be at 40.69% of the duty cycle. The $d^{50\%}$ value does change with the polarization as well. The **polarisation dependence** of the correct duty cycle frequency d has been determined to

$$d^{50\%}_{Pol} \leq 2.20\%.$$

One single source U_0 is used to power all heating elements. Due to the non-zero **internal resistance** of the source, at a high load (many heaters activated) the voltage U_0 will drop. A stabilizing electric circuit has been implemented reducing the change in duty cycle of a single heater to less than

$$d^{50\%}_{\Delta U_0, a7} < 0.16\%.$$

Other activated heating elements on the chip influence the temperature distribution on chip and thus, also influence other heating elements. The magnitude of influence clearly depends on the distance and the applied (heating) power verifying the temperature as the major cause. Using the temperature stabilization and chip holder acting as a heat sink the temperature change between all other heaters off and all heaters at 50% was minimized to a change in duty cycle of

$$d^{50\%}_{T} < 0.5\%.$$

6.1.3 Realization of the Bellport

Exemplary the BP is realized and the unitary transformation is verified. In order to check the resulting unitary transformation cw light is inserted into every input of the BP and detected at each output leading to the experimentally determined $|BP|^2$ matrix:

$$|BP_{Exp}|^2 = \begin{pmatrix} 0.3347 & 0.2411 & 0.2448 \\ 0.3305 & 0.2371 & 0.2527 \\ 0.3362 & 0.3251 & 0.3286 \end{pmatrix}. \tag{6.1}$$

The upper right elements of eq. 6.1 are of lower intensity. In principle every element should have an absolute value squared of 1/3. Excluding the global in- and output phases there is one internal phase whose error influences Eq.6.1. In order to get an estimate of the error of the characterization we will assume a Multiport $BP_{theor}(\lambda, \delta\varphi)$ with an internal loss λ of a PDC and an error on the internal phase of $\delta\varphi$. The best agreement between BP_{exp} and BP_{theor} can be found for

$$\lambda = 1.95dB\ ,\ \delta\varphi = -0.018 = -0.57\%\pi.$$

The good agreement confirms the loss λ of the PDC as the cause of the reduced intensity of eq. 6.1. The value of $1.95dB$ agrees with the previously determined loss (section 4.6). The residual difference (R) between theoretical and measured intensity then becomes:

$$R_{rel} = \frac{|BP_{exp}|^2 - |BP_{theor}(1.95dB, -0.57\%\pi)|^2}{|BP_{theor}(1.95dB, -0.57\%\pi)|^2}$$

$$R_{abs} = |BP_{exp}|^2 - |BP_{theor}(1.95dB, -0.57\%\pi)|^2$$

$$R_{rel} = \begin{pmatrix} -0.40 & 2.50 & -2.48 \\ 0.85 & 0.76 & -2.21 \\ -0.86 & 2.46 & 1.42 \end{pmatrix} \%$$

$$R_{abs} = \begin{pmatrix} -0.0013 & 0.0062 & 0.0059 \\ 0.0028 & 0.0018 & -0.0055 \\ -0.0029 & 0.0082 & 0.0047 \end{pmatrix}. \tag{6.2}$$

Note, the given loss λ and residual intensity differences R are given as intensities. The error in amplitude will be the square root.

Therefore, given the (unfortunate) PDC loss the unitary BP matrix can be realized with a precision of each matrix element (i, j) of better than

$$\delta R \leq |\pm 0.0082|\,.$$

The best value of the error of the phase is

$$\delta\varphi_{i,j} \leq |\pm 0.57\%\pi|\,.$$

Same can be done for the second Multiport resulting in

$$\lambda_2 = 1.61dB.$$

Following section 4.6, performing a simulation with two Bellports with perfect phase and reflectivity setting but an internal loss of $1.95dB$ and $1.61dB$ results in a maximum correlation probability reduction averaged over all bases of 96.4%. Due to the unnecessary PDC loss 96.4%. will be the maximum experimentally achievable value.

6.1.4 Coverage of the unitary space

Following section 2.3.3 the coverage (cov) of the full unitary space can be estimated. Every MZI of the Multiport is characterized and the visibility (V) is extracted via the fit described in section 2.3.3. $V \neq 1$ means the MZI cannot realize every reflectivity. According to eq. 2.13, not any rotation ($e^{iY\lambda}$) between the two modes can be realized because λ is limited. The visibilities of the three MZIs of both qutrit Multiports are given in tab.6.4

	MP2.12		MP2.13	
MZI	V(%)	cov($SU(2)$) (%)	V(%)	cov($SU(2)$) (%)
(1,2)	96.1 ± 0.3	99.960 ± 0.005	90.8 ± 0.6	99.98 ± 0.03
(1,3)	98.6 ± 0.3	99.994 ± 0.002	88.0 ± 0.7	99.59 ± 0.05
(2,3)	99.4 ± 0.3	99.999 ± 0.001	85.6 ± 0.7	99.40 ± 0.06

Table 6.4

Phase shifters are not limited in their operation since any phase modulo 2π can be applied. The only limit is the precision of the 12bit PWM signal which does not pose a fundamental limit. From eq. 2.13 it follows $\lambda = Sin^{-1}\left(\sqrt{1-r}\right)$. The reflectivity r can only reach values between $r = \delta ... 1$ with $\delta = \frac{1-V}{1+V}$. Using Eq.2.19 the coverage can be calculated:

$$cov_N = \frac{\overbrace{\int\int ... \int}^{\lambda_{i,j}=min_{i,j}...max_{i,j}} d\lambda_{1,2} d\lambda_{2,1} ... d\lambda_{N,N}}{\int_{SU(N)} dU_N}.$$

Tab. 6.5 presents the results.

MP	cov $(SU\,(3))$	cov $(SU\,(3) \otimes SU\,(3))$
2.12	$99.95^{+0.01}_{-0.01}\%$	$98.32^{+0.19}_{-0.19}\%$
2.13	$98.37^{+0.18}_{-0.19}\%$	

Table 6.5: Coverage of the unitary space for each qutrit A and B ($cov^{A/B}_{SU(3)}$) and the full $SU(3) \otimes SU(3)$ space $cov^{A}_{SU(3)} \cdot cov^{B}_{SU(3)}$.

Therefore, a coverage of $(98.32 \pm +0.19)\%$ of the full qutrit-qutrit $SU\,(3) \otimes SU\,(3)$ space can be realized. 1.68% unitary transformations from $SU(3) \otimes SU(3)$ are not possible. Those transformations are impossible because some MZIs cannot reach the corresponding reflectivity value. One example which cannot be realized:

$$U \otimes U \propto \begin{pmatrix} 1 & 1 & 0 \\ 1 & 1 & 0 \\ 0 & 0 & \sqrt{2} \end{pmatrix} \otimes \begin{pmatrix} 1 & 1 & 0 \\ 1 & 1 & 0 \\ 0 & 0 & \sqrt{2} \end{pmatrix}. \tag{6.3}$$

Effectively the above transformation results in a qubit-qubit system and is likely not of great interest using the 3×3 Multiport. However, if such a transformation is desired one could eliminate the unwanted contribution from the 3rd mode by applying the 50Hz signal (see section 2.6).

6.1.5 Visualization of the coverage

According to eq. 2.9 the coverage of a $SU(2)$ Multiport can be parametrized by one rotation (λ_r), one phase shift (λ_φ), and one global phases which can be ignored. One way of visualization therefore is to display the two parameters (r, φ) as polar coordinates $(\lambda_r Sin(\lambda_{\varphi'}), \lambda_r Cos(\lambda_{\varphi'}))$ with λ_φ mapped onto $\lambda'_\varphi = 0...2\pi$. A perfect Multiport would therefore result in a full circle of radius 1. More interesting is the combination with the digital PWM signal of limited resolution (12bit): movement in $SU(3)$ will only be possible at a certain step size dU. Characterizing both phase shifters (fig. 6.1) will lead to a fit connecting the normalized transmitted intensity to the PWM signal I(PWM). The parameter λ_r is related to the MZI reflectivity r (section 2.2.3) via

$$Sin(\lambda_r) = \sqrt{1-r} = \sqrt{1-I(PWM)}$$

and equivalent for the phase shifter $\varphi = 2\lambda_\varphi$. The given relation $Sin^2(\varphi/2) = I(PWM)$ leads to

$$\lambda_\varphi = 2Sin^{-1}\left(\sqrt{I(PWM)}\right).$$

Now the step size can be calculated $d\lambda = \frac{d\lambda}{dPWM} dPWM$. Note, that the step size $d\lambda$ is not uniform but depends on the position λ. The PWM resolution of 12bit leads to a PWM step size of the duty cycle of

$$dPWM = 1/12bit.$$

The results for one $SU(2)$ unit (PIN A3) inside the 3×3 Multiport are displayed in fig. 6.4. A similar plot can be done for every $SU(2)$ unit of the 3×3 Multiport. The coverage of $SU(3)$ (eq. 2.10) can be displayed by three of such graphs (fig. 6.4) of $SU(2) \otimes SU(2) \otimes SU(2)$ (ignoring the global phases).

Fig. 6.5 shows some examples of 2×2 unitary matrices in the corresponding parameter space: the Pauli matrices together with a symmetric and antisymmetric beam splitter:

$$BS_{sym} = \frac{1}{\sqrt{2}} \begin{pmatrix} 1 & i \\ i & 1 \end{pmatrix}, \; BS_{asym} = \frac{1}{\sqrt{2}} \begin{pmatrix} 1 & 1 \\ 1 & -1 \end{pmatrix}. \tag{6.4}$$

Analogically, every MZI of the Tritter on MP2.12 is characterized. The resulting parameter space is displayed in fig. 6.6. Characterization of the two Multiports completes the setup.

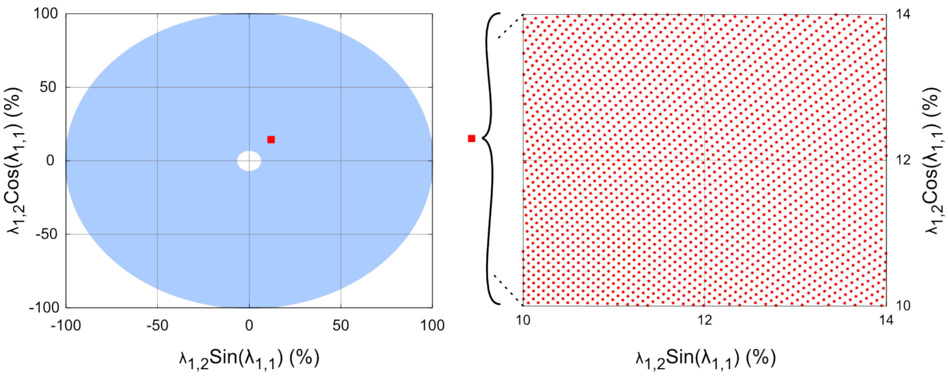

Figure 6.4: **Left:** display of the parameter range for both parameters λ in polar coordinates $(\lambda_r Sin(\lambda_\varphi), \lambda_r Cos(\lambda_\varphi))$. λ_r (λ_φ) are the parameters corresponding to the (limited) MZI reflectivity r and phase shift φ. The light blue area represents the space which can be reached by the Multiport. The white area in the middle is not accessible due to the limited visibility of the MZI. **Right:** Magnification of the red area of the left picture. The points are separated by the minimal step size limited by the resolution $(1/12bit)$ of the PWM signal.

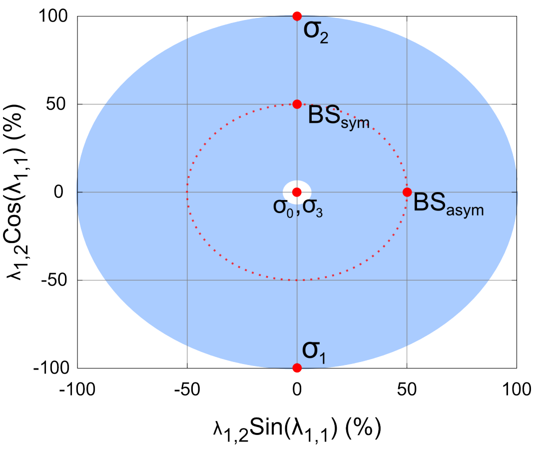

Figure 6.5: Examples of the position of certain 2×2 unitary matrices. The Pauli Matrices σ_i, $i = 1, 2, 3$ and the diagonal one matrix σ_0 together with a symmetric and antisymmetric beam-splitter (see. Eq.6.4).

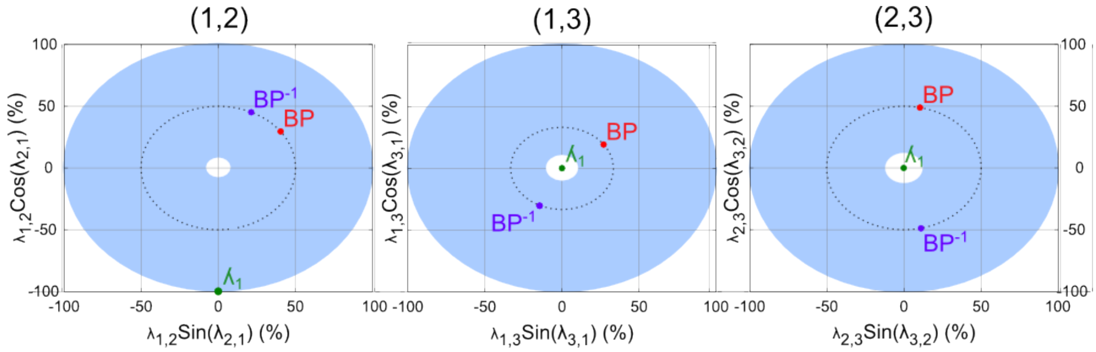

Figure 6.6: Equivalent to fig. 6.4 every 2×2 MZI ((1,2),(2,3) and (1,3)) of the 3×3-MP is characterized. The product $SU(2) \otimes SU(2) \otimes SU(2)$ then represents the full 3×3 unitary space (up to global phases). Some example unitary transformations are displayed: the Bellport (BP), the inverse Bellport BP^{-1} and one of the Gell-Mann Matrices λ_1.

6.2 Overview of the setup

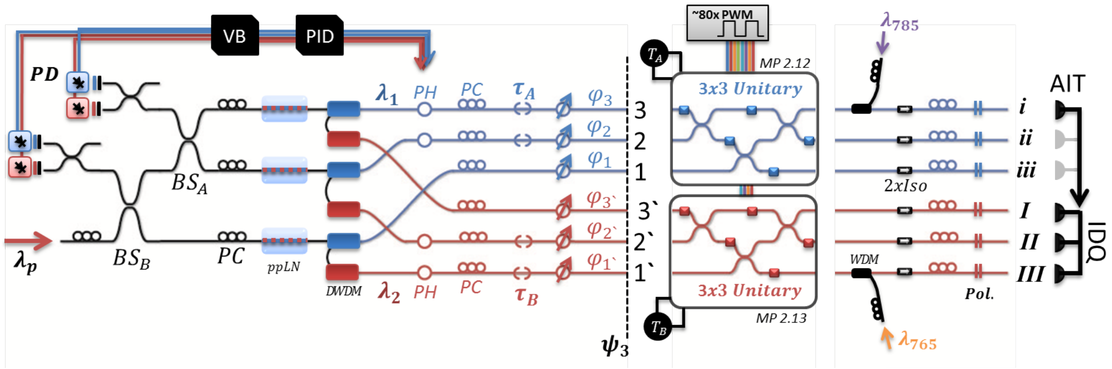

Figure 6.7

The full experiment is presented in fig. 6.7. The source produces a state of two entangled qutrits

$$|\Psi_3\rangle = \frac{1}{\sqrt{3}}\left(e^{i\left(\varphi_1+\varphi_1'\right)}|11\rangle + e^{i\left(\varphi_2+\varphi_2'\right)}|22\rangle + e^{i\left(\varphi_3+\varphi_3'\right)}|33\rangle\right). \tag{6.5}$$

The splitting ratios of the bump beam have been chosen such that the state is of balanced amplitudes. The phases $\varphi_1, \varphi_1', \varphi_2, \varphi_2', \varphi_3, \varphi_3'$ are controlled by the PID controller. Each entangled qutrit of the source is connected to a Multiport. Each Multiport will display a particular unitary transformation U via the corresponding phase and reflectivity setting of its components. The state $|\Psi\rangle$ is thus transformed to

$$|\Psi_3'\rangle = (U_A \otimes U_B)\,|\Psi_3\rangle\,.$$

Single photon detectors are placed at the output of the Multiports. The outputs will be labeled i, ii, iii for qutrit A and I, II, III for qutrit B. Events of joint detection between output i of qutrit A and output III of qutrit B will for example be labeled by (i, III) whereas the probability amplitude is given by

$$\langle i, III|\Psi_3'\rangle\,.$$

Due to the triggered detection scheme only one detector at one output is used for detecting qutrit A. Thus, only the coincidence events between (i, I) (i, II) and (i, III) are simultaneously recorded. In order to measure a different output of Multiport A the detector is connected to a different output[1].
In the following, "corrected" will refer to a value where the based coincidence count rates have been corrected for accidental coincidence detection events.

[1]Ultimately, three detectors on both sides are of advantage but has not been fully implemented within the given time.

6.3 Pairwise quBit results

Measurements within all three qubit-qubit subspaces of the entangled qutrit pair will be presented. The results serve as an estimate of the quality of the final qutrit state similar to section 3.2.3.

6.3.1 Visibility

Combinations of the Pauli matrices σ_i are displayed by the Multiports. The Pauli Matrices have only two non zero off diagonal elements. Therefore, only two modes (qubit) are put to interference. Applying $\sigma_i \otimes \sigma_i$ for $i = 1, 2, 3$ the visibility is obtained and averaged over all basis for every qubit combination. Tab. 6.6 presents the results.

Corr. Visibility (%)	Visibility (%)
$\overline{V^C_{1,2}} = 92.6 \pm 0.6$	$\overline{V_{1,2}} = 81.2 \pm 0.5$
$\overline{V^C_{1,3}} = 84.2 \pm 1.0$	$\overline{V_{1,3}} = 72.8 \pm 1.0$
$\overline{V^C_{2,3}} = 93.2 \pm 0.6$	$\overline{V_{2,3}} = 80.7 \pm 0.6$

Table 6.6: Visibility $V^{\sigma_k \otimes \sigma_l}_{i,j}$ averaged over all bases $\sigma_x \otimes \sigma_x$, $\sigma_y \otimes \sigma_y$ and $\sigma_z \otimes \sigma_z$ of the quantum system formed by the modes (i, j) and (i', j').

Compared to the qubit visibility of $V = (97.3 \pm 0.5)\%$ of the qubit source presented in section 3.2.3, the visibility now is considerably lower. One reason is the following: the MZIs of the two Multiports do have a finite extinction ratio (see previous section) causing cross-talk. In principle, for example, when measuring the visibility of modes $(1, 2)$ $(V^{\sigma_z \otimes \sigma_z}_{1,2})$ the third mode should not interact with the others. However, due to the non-perfect MZIs a residual interference signal is maintained and the visibility is reduced.

6.3.2 Non-perfect Pauli matrices - qubit tomography

The qubit state of every 2-dimensional subspace of the full entangled qutrit space is reconstructed (section 2.4). For each of the three possible combinations of modes (i, j) every combination of $\sigma_a \otimes \sigma_b$ for $a = 1..3$, $b = 1...3$ is measured. From the 3×36 measurements the three density matrices can be calculated. A maximum likelihood estimation is performed. As has been discussed in the previous section 6.1.4 the MZIs exhibit a non-perfect visibility in the range of $(99.4 \pm 0.3)\%$ to $(85.6 \pm 0.7)\%$. Nevertheless, we will assume the displayed Pauli matrices are perfectly realized although they lie outside of the covered unitary space (fig. 6.4 and fig. 6.5). Consequently, the assumption of perfect MZIs will reduce the quality of the measured density matrix and its fidelity. Therefore, the results will tell us not only the quality of the produced entangled state but also whether or not it is reasonable to assume perfect unitaries (although outside of the covered space) with some reduction in visibility. The resulting real and imaginary parts of the density matrices ρ are presented in fig. 6.8, 6.9, and 6.10 for the three qubit subspaces labeled A,B and C.

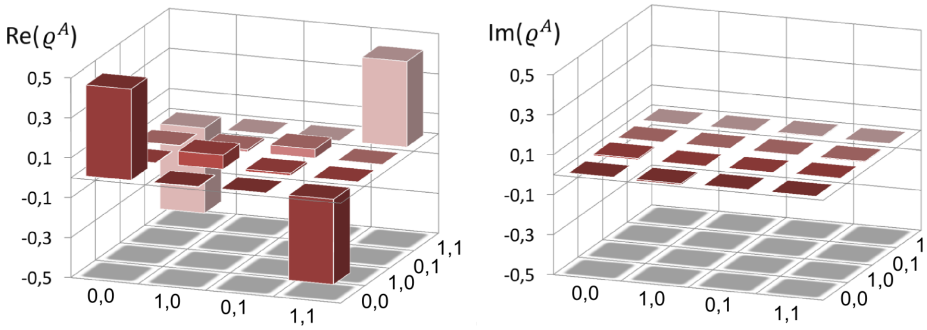

Figure 6.8: Reconstructed **corrected** density matrix ρ. All imaginary parts are $Im\left|\rho^A_{i,j}\right| < 0.01$.

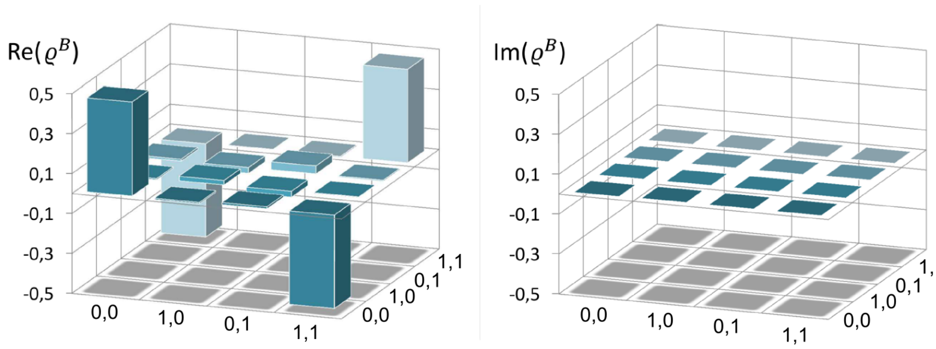

Figure 6.9: Reconstructed **corrected** density matrix ρ. All imaginary parts are $Im\left|\rho^B_{i,j}\right| < 0.01$.

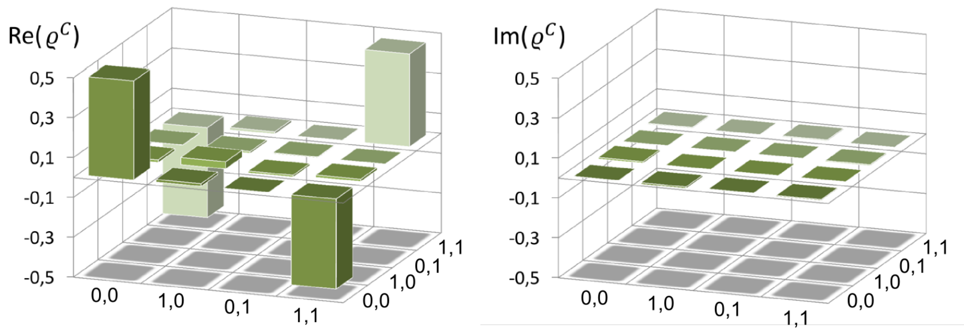

Figure 6.10: Reconstructed **corrected** density matrix ρ. All imaginary parts are $Im\left|\rho^C_{i,j}\right| < 0.01$.

Assuming the theoretically expected perfect state to be of the form

$$\rho = \frac{1}{2}\begin{pmatrix} 1 & 0 & 0 & -1 \\ 0 & 0 & 0 & 0 \\ 0 & 0 & 0 & 0 \\ -1 & 0 & 0 & 1 \end{pmatrix} \tag{6.6}$$

the fidelity can be calculated and is given in tab. 6.7.

subspace	Fidelity (%)
A	93.33 ± 0.88
B	96.86 ± 0.69
C	96.22 ± 0.73

Table 6.7: Corrected fidelity of the reconstructed state compared to the perfect theoretically expected state. Accidental coincidence counts have been subtracted.

6.4 QuTrits

Fig. 6.11 illustrates the process of setting all phases of the state. Applying a 50Hz signal to the phase shifters of the outer modes 1 and $1'$ the constribution of the corresponding amplitude to the coincidence signal is terminated (section 2.6). The inner MZI formed by modes $(2, 3)$ is characterized (blue) and set to the desired phase and similarly for modes $(2', 3')$. Afterward, the 50Hz signal on the outer modes is stopped and the outer phases φ_1 and φ_1' are characterized (red).

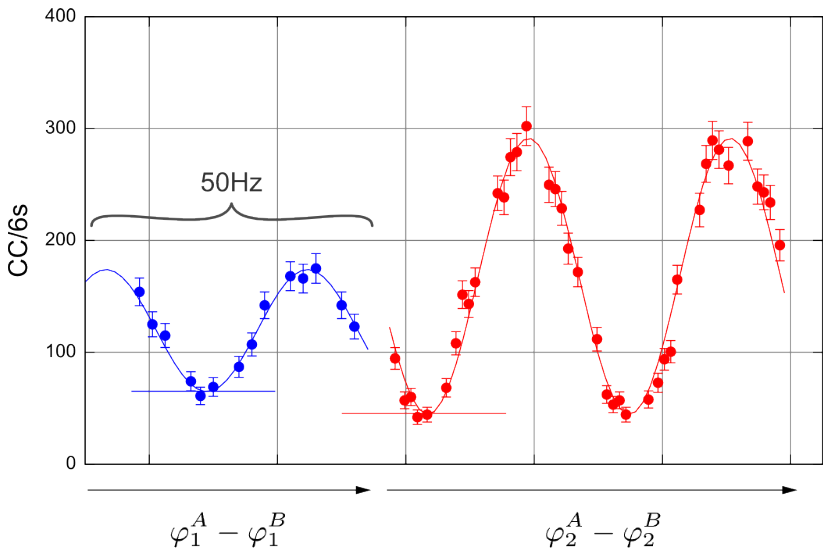

Figure 6.11: The phase pairs of the entangled qutrit state are set iteratively. First a 50Hz signal is applied to the outer channel effectively eliminating its contribution to the coincidence signal leading to the interference of two modes (amplitudes). After the phases have been set to a desired value the 50Hz signal is turned off and the outer MZI is characterized. Now, the interference of three modes (amplitudes) defines the signal.

The amplitude difference of the red and blue signals (fig. 6.11) corresponds to the height expected from the interference of two vs. three equal amplitudes. From the amplitude of the blue fit $2A_{bit} = 109.1/s$ one can calculate the expected qutrit amplitude assuming that $A_0 = A_1 = A_2$:

$$\left(\frac{3}{2}\sqrt{A_0^2 + A_1^2}\right)^2 = \left(\frac{3}{2}\sqrt{(109.1 \pm 3.5)/s}\right)^2 \approx (245.6 \pm 7.9)/s.$$

From the red fit it follows that the qutrit amplitude has a value of

$$2A_{Trit} = (246.9 \pm 5.2)/s$$

Both values are in good agreement. Fig. 6.11 also shows a difference in the minimum of the red and blue fringe. The reason for the higher offset is the third mode at which 50Hz are applied causing an offset of the signal by A_3^2 and therefore reducing the visibility by a factor of $2/3$.

Theoretically, the third averaged mode would cause an offset (Δ_{off}) of

$$\Delta_{off} = \left(\frac{1}{2}\sqrt{(109.1 \pm 3.5)/s}\right)^2 \frac{2}{3} \approx (18.2 \pm 0.6)/s.$$

Experimentally, an offset of

$$\Delta_{off}^{exp} = (20.3 \pm 1.5)/s$$

is measured. The measured offset is slightly higher. The reason is due to the noise created by the 50Hz signal. All phase shifter are driven by the same electric board. Driving the piezo phase shifter at 50Hz and an amplitude of $90V$ creates electric crosstalk to the other phase shifters and therefore slightly reduces the visibility. However, the characterization is not affected since the offset does not appear in the argument of the sin^2 dependance.

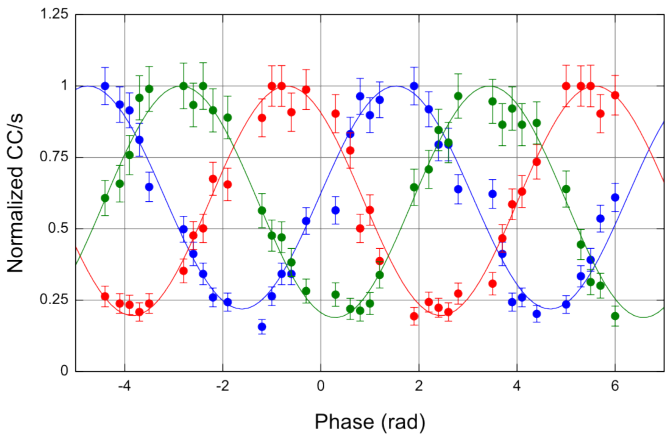

Figure 6.12: Typical normalized coincidence signal of all three possible detector combinations of qutrit A (one detector i) and qutrit B (detectors I, II, III): (i, I),(i, II),and (i, III). The low visibility is due to an increased pump intensity for faster characterization.

Fig. 6.12 shows the typical signal of all three detector combinations. As expected the three signals show an offset of $\frac{1\pi}{3} = 60°$. The difference in detection rates between the three triggered detectors is roughly given by $\{100\%, 80\%, 70\%\}$.
The phases $\varphi_2 - \varphi_2'$ are characterized and set to the angles

$$\varphi_2 - \varphi_2' = 0°, 10°, 20°, ...350°, 360° \;,\; \varphi_3 - \varphi_3' \equiv 0.$$

Afterward, $\varphi_1 - \varphi_1'$ is scanned from $0...2\pi$ recording all coincidence events (i, I),(i, II),and (i, III). The resulting amplitude of the measured coincidence signal is plotted in fig. 6.13. As expected the three maxima are displaced by $\frac{2\pi}{3}$ and $\frac{4\pi}{3}$. Note, the amplitude of the fit is plotted. If one detector exhibits a maximum correlation the other two amplitudes will be of equal height and therefore completely (destructively) interfere.

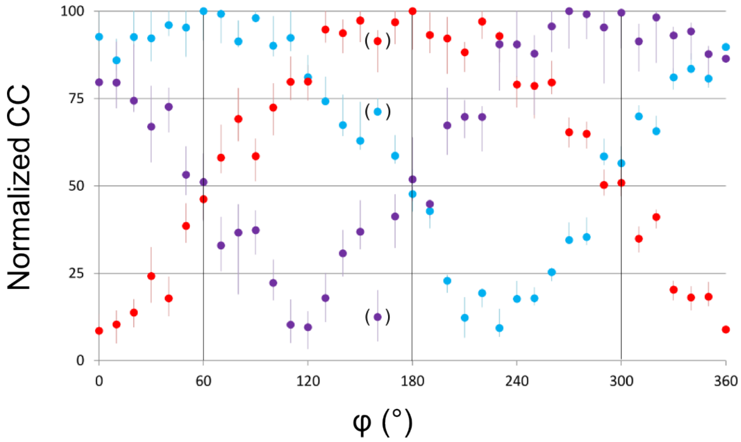

Figure 6.13: Amplitude of the coincidence fringe when scanning the phases $\varphi_1 - \varphi_1'$ after the inner phases $\varphi_2 - \varphi_2'$ have been characterized and set to $\varphi_2 - \varphi_2' = \varphi$ while $\varphi_3 - \varphi_3' = 0$. The error is a result of the Poisonian noise and the estimated uncertainty of the fit parameters based on a Monte Carlo simulation.

Typically, the pump power has been chosen to be at around $4\frac{\text{mW}}{\text{crystal}}$ resulting in approximately $\approx 30CC/s/$crystal and a signal-to-noise of $SNR \approx 10$. A characterization scan is performed with 15 measurement points and an integration time of 6s. The fit is of the form: $\propto sin^2\left(\frac{1}{2}\varphi + \delta\varphi\right)$. In order to set the system to the correct phase the phase offset $\delta\varphi$ is of importance. To estimate the uncertainty of the fit parameter $\delta\varphi$ due to Poissonian counting statistics a Monte Carlo simulation is performed. The result is an average standard error $\sigma_{\delta\varphi}$. The two relative phases (inner and outer MZI) of each qutrit can be set with a precision of:

$$\sigma_{\delta\varphi} \approx \quad 1.2\%\pi = 2.2° \tag{6.7}$$

$$\sigma_{\delta\varphi} \approx \quad 0.6\%\pi = 1.2°. \tag{6.8}$$

The difference originates from the different count rates due to the superposition of two (three) crystals for the inner (outer) MZI. The error is solely based on the intrinsic Poissonian error of the counted number of photons and can be decrease by an increase in integration time or number of measurement points.

6.4.1 The correlation space

N=2

Quantum correlations of an entangled two qubit state exiting two local 2×2 Bellports are, of course, well known. The entangled state has one free phase φ. For $\varphi = 0$ (π) maximum (minimum) coincidences are obtained. Although with a low SNR, the blue fringe in fig. 6.11 represents qubit correlations.

Due to the symmetry of the Bellport / beam splitter, measuring both outputs of a beam splitter (with input phase φ) with two detectors is equivalent to two measurements at one output using the phases φ and $\varphi + \pi$. This is due to the elements of the Bellport being the second root of unity $\left(\omega = e^{i\frac{2\pi}{2}}\right)$:

$$BP_{2\times 2}\left|1\right\rangle = \frac{1}{\sqrt{2}}\begin{pmatrix} \omega^2 & \omega^2 \\ \omega^2 & \omega^1 \end{pmatrix}\left|1\right\rangle = \frac{1}{\sqrt{2}}\begin{pmatrix} \omega^2 & \omega^2 \\ \omega^2 & \omega^1 \end{pmatrix}\begin{pmatrix} \omega^1 & 0 \\ 0 & \omega^0 \end{pmatrix}\left|0\right\rangle. \tag{6.9}$$

Dimension N=3

The Bellport is displayed onto both Multiports:

$$U_{BP} \otimes U_{BP}\left|\psi\right\rangle.$$

The state of eq. 6.5 serves as the input:

$$\left|\Psi_3\right\rangle = \frac{1}{\sqrt{3}}\left(e^{i\left(\varphi_1+\varphi_1'\right)}\left|11\right\rangle + e^{i\left(\varphi_2+\varphi_2'\right)}\left|22\right\rangle + e^{i\left(\varphi_3+\varphi_3'\right)}\left|33\right\rangle\right).$$

The relative phase $\varphi_2 - \varphi_2'$ is set in $10°$ steps from $0°, 10°, 20°, ..., 350°, 360°$ while $\varphi_3 - \varphi_3' = 0$. For every phase $\varphi_x = \varphi_2' - \varphi_2$ the phase $\varphi_y = \varphi_1 - \varphi_1'$ is scanned from 0 to 2π. All coincidence events (i, I),(i, II), and (i, III) are recorded. The resulting data is fitted. The 3×36 fits are displayed slice by slice in fig. 6.14 and fig. 6.15. The integration time is 8s with $\approx 600CC/8s$ at maximum and $SNR \approx 10$. The characterization scans 15 measurement points each with 8s integration time meaning an average step size of $\approx 25°$. Data has not been corrected for accidental detection events. As can be seen from fig. 6.14 for a specific set of phases the maximum/minimum coincidence count rate is reached. Note, the characterization of a MZI cannot give any information on a global phase. Setting the inner phase φ_x to a certain value will cause a global offset to the outer MZI. However, this will not be visible, neither in the characterization nor in the resulting fit parameter. The offset of the inner MZI therefore is added manually to the fit parameter.

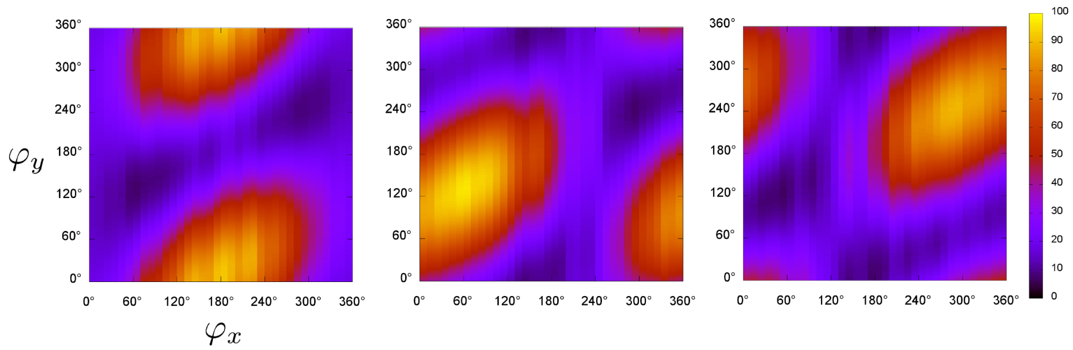

Figure 6.14: Scan of the correlation space for two entangled qutrits. Each picture corresponds to a detector combination (i, I),(i, II), and (i, III). Coincidences are normalized to the maximum value and given in percent (%). The horitzontal (vertical) axis corresponds to $\varphi_x = \varphi_2' - \varphi_2$ ($\varphi_y = \varphi_1 - \varphi_1'$). No accidentals are subtracted. Integration time is 8s with $\approx 600CC/8s$ at maximum. The data points are fitted and the resulting fits are displayed as slices in the image above along the axis of φ_y.

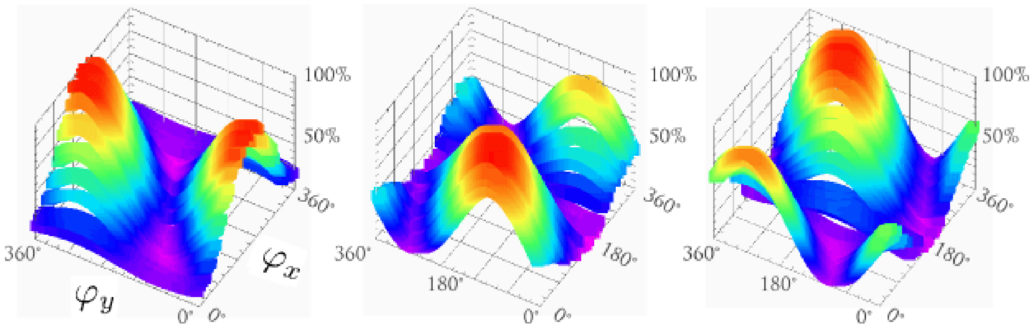

Figure 6.15: 3D plot of the data shown and described in fig. 6.14.

The experimental results (fig. 6.14) can be compared to the theoretic predictions:

$$P_{i,j} = \frac{1}{3}\left|\sum_{k=1}^{3} e^{i\varphi_k} U_{BP} U_{BP}\right|^2$$

with $P_{i,j}$ being the probability of detecting a photon at detector j after detector i has clicked. φ_k are the input phases of the entangled state. Fig. 6.16 shows the theoretical prediction.

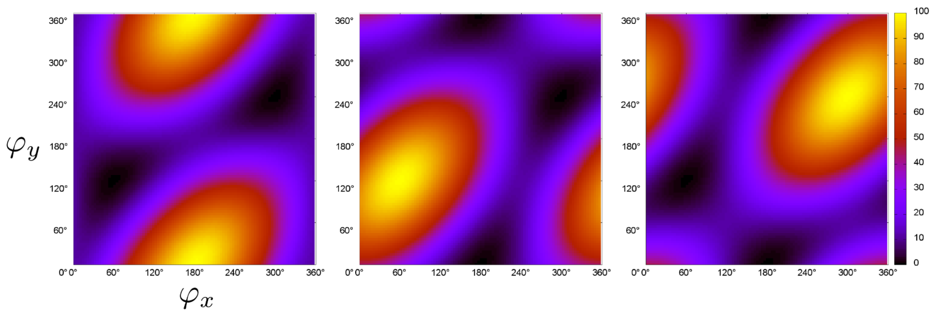

Figure 6.16: Theoretical prediction of the joint detection probability given in percent (%) between the three detector combinations (i, I),(i, II), and (i, III).

Comparing fig. 6.14 to fig. 6.16 reveals excellent agreement between theory and experiment. As expected, the experimental results show a non perfect contrast between maximum and minimum coincidence rates due to experimental flaws.

If one detector combination, for example, (i, I) exhibits maximum coincidences the other two detector combinations (i, II), and (i, III) must show a minimum in detected coincidences. As can be seen in fig. 6.14, if at one phase combination one graph shows a maximum then the other two graphs will be at a minimum as dictated by normalization.

The correlation pattern presented in fig. 6.14 is similar to the classical interference pattern of a three-path MZI as previously observed by G. Weihs, M. Reck, H. Weinfurter, and A. Zeilinger [22]. However, here, the pattern is non-classical and due to the two qutrit entangled state. It only becomes visible in coincidence detection. Local observation of single detection events for only one of the two photons ideally does not exhibit any pattern and a photon will be observed with the same probability $1/N$ at any output of the Multiport.

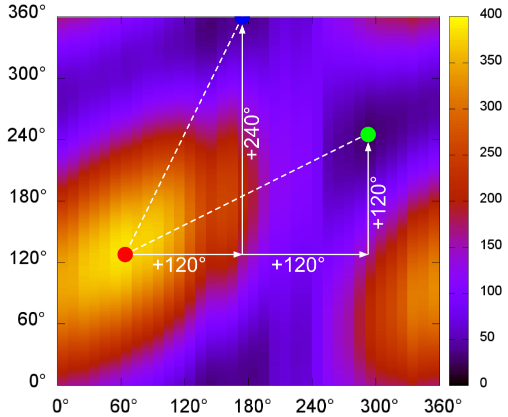

Figure 6.17: Magnified image of the detector correlation (i, I) of fig. 6.14.

Fig. 6.17 presents a closer look at the correlation space between detectors (i, I). The maximum appears at $(60°, 120°)$ while minima appear at $(180°, 360°)$ and $(300°, 240°)$. At each minimum one of the other detector combinations shows a maximum. As expected, The relative distance of the extrema is given by:

$$(0°, 0°)\ ,\ (+120°, +240°)\ ,\ (+240°, +120°) \tag{6.10}$$

Effectively, measuring a certain point (φ_1, φ_2) in correlation space for all possible detector combinations (i, i) ,(i, II),(i, III), (ii, i) ,(ii, II),(ii, III), (iii, i) ,(iii, II),(iii, III) is equivalent to measuring the three points

$$(\varphi_1, \varphi_2)\ ,\ (\varphi_1 + 120°, \varphi_2 + 240°)\ ,\ (\varphi_1 + 240°, \varphi_2 + 120°) \tag{6.11}$$

recording only joint detection events between (i, I),(i, II), and (i, III). Eq. 6.11 is expected due to the period of ω, the N-th root of unity forming the Multiport elements. Fig. 6.18 shows the (theoretic) correlation space for one detector pair with phases ranging from -2π to $+2\pi$. Here, the period and the equivalence between measuring three detectors or 3 points in correlation space with an offset becomes visible.

Fig.6.18 illustrates another feature of the correlation pattern. As stated by Weihs, Reck, Weinfurter, and Zeilinger [22], a three path interference pattern as well as the three mode quantum correlation pattern will exhibit a higher phase sensitivity S defined as

$$S \propto \left|\frac{dI}{d\varphi}\right|.$$

I represents the intensity or the coincidence count rate. The reason for the increased sensitivity is the increasing steepness of the peaks of maximum correlations. Generally, in an N-mode interference pattern there will be $N-2$ side lobes between the two main peaks [22]. Following the white dashed line in fig. 6.18 the one side lobe of the $N = 3$ dimensional system is encountered.

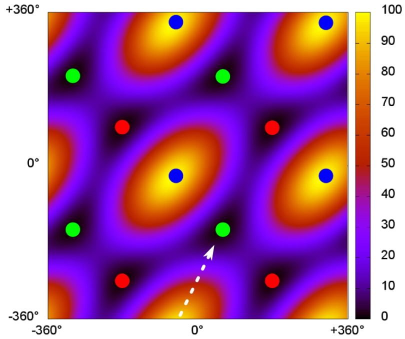

Figure 6.18: Display of the qutrit correlation space. Differently colored points have a distance equal to Eq.6.11 corresponding to the three different detectors measuring one of the entangled qutrits. Following the white line a side lobe (local maximum) can be found between two main peaks. As a consequence, the steepness of the peaks of maximum correlations has increased resulting in a greater phase sensitivity compared to a two qubit correlation pattern.

The same feature is visible in the experimental correlation pattern of fig. 6.14 along the diagonal line and is presented in fig. 6.19. The side lobe between two global maxima is clearly visible. The global maxima are separated by 360°. However, as illustrated in fig. 6.20 compared to the sin^2-function of a $N = 2$ quantum system the maxima are of higher steepness due to the side lobe. Thus, a higher phase sensitivity is achieved.
Every data set of fig. 6.19 was individually fitted. From the resulting best fit parameters the position of the maxima can be calculated:

$$(61.2 \pm 1.0)^\circ \ , \ (179.2 \pm 1.0)^\circ \ , \ (300.7 \pm 1.0)^\circ$$

which is in agreement with the theoretic predictions of Eq.6.11.

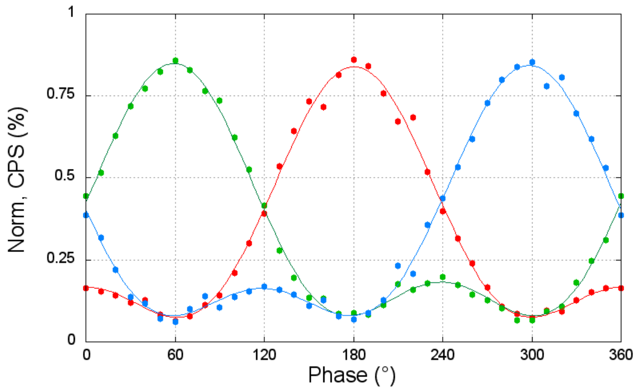

Figure 6.19: Normalized coincidence rates for sets of phases along a diagonal line $(\varphi_x, 2\varphi_y)$ for (i, I),(i, II), and (i, III) as presented in fig. 6.14. Points represent the points of interception between the diagonal line and the fit. The error is a result of different influences such as the accuracy of the fit or the error in setting the phase to the correct value. For simplicity error bars are not shown. The upper bound is estimated to approximately $\delta\varphi_{CPS} \leq 0.035$ and $\delta\varphi_x \leq 2.6$. Accidental coincidence count rates where not corrected for.

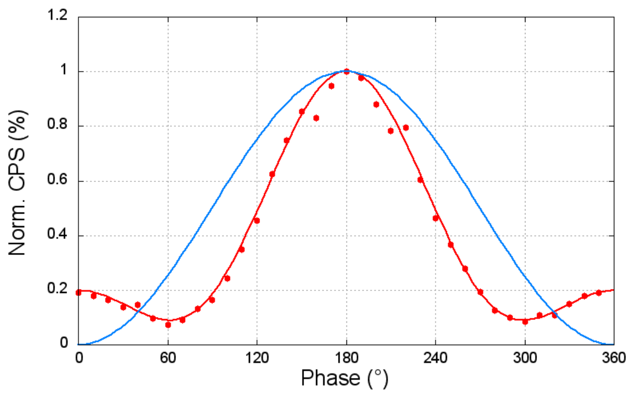

Figure 6.20: Illustration of the increased phase sensitivity. (i, I) is taken from fig. 6.19 and normalized to the maximum value. For comparison to a $N = 2$ system the expected $sin^2(\varphi/2)$ function is plotted.

N=4

Although a 4×4-Multiport has been realized on the chip and the source has been built for ququarts we were not able to complete an experiment revealing entangled ququart perfect correlations in time. However, for completeness, theoretical predictions are briefly presented here. The 4×4 Bellport is assumed. The entangled input state is of the form

$$|\psi\rangle \propto |11\rangle + e^{i\varphi_1}|22\rangle + e^{i\varphi_2}|33\rangle + e^{i\varphi_3}|44\rangle \,.$$

In dimension N the correlation space will be defined by a set of $N-1$ relative phases. For $N=4$ the correlation space therefore is 3-dimensional. Fig. 6.21 presents the expected correlation space.

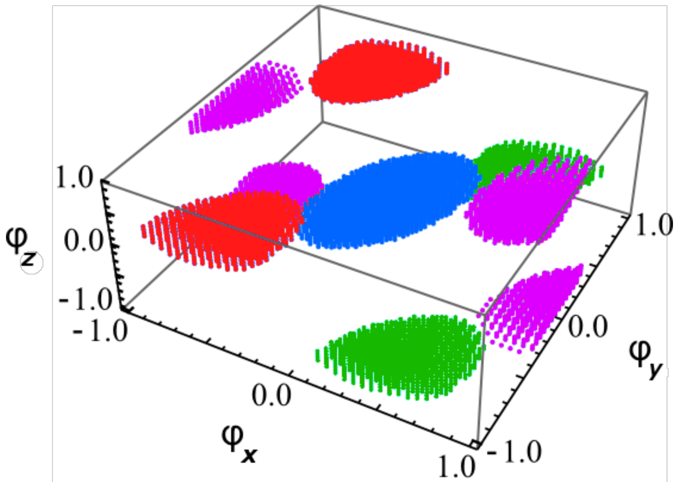

Figure 6.21: The two ququarts correlation space depending on the three relative phases $\varphi_1, \varphi_2, \varphi_3$ of the entangled ququart state. Two 4×4 Bellports are assumed. Plotted in steps of 0.05π, a plotted point represents a joint detection probability of $> 80\%$. The different colors correspond to the four different detectors at the output of ququart A triggered by the same single detector of ququart B.

6.4.2 Perfect correlations

Dimension N=2

In section 3.4 the points of the maximum/minimum correlations have been measured. The results are displayed in fig. 6.22.

Figure 6.22: Perfect correlations of entangled two qubit on a beam splitter. Results taken from section 3.4. Numbers represent the probability of the correlation in percent after accidental subtraction. Error is $\leq \pm 0.5\%$.

Dimension N=3

Following the complete mapping of the correlation (fig. 6.14), the input entangled qutrit state is set to the phase values corresponding to the extreme points and the coincidences are recorded. The resulting perfect correlations are depicted in fig. 6.23.

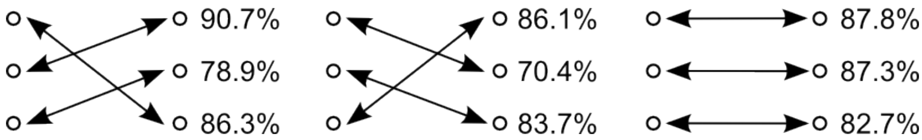

Figure 6.23: Perfect correlations between detectors on each qutrit side. Error is ±2.0%. The reason for the relatively high error is that the triggering detector is connected to different outputs by unplugging and reconnecting the fiber. The source is not realigned after reconnection. The unknown connection loss and polarisation change cause the uncertainty. No correction of accidental coincidences was performed.

6.5 Qutrit state tomography

The corrected density matrix of maximum likelihood is reconstructed. A subset of all possible combinations of Gell-Mann matrices $(\lambda_i \otimes \lambda_j)$ (eq. 2.4) displayed on each of the two Multiports has been used. The remaining set of measurements does not contribute to any interference and thus, the theoretically expected value is assumed. The resulting corrected density matrix ρ is presented in fig. 6.24.

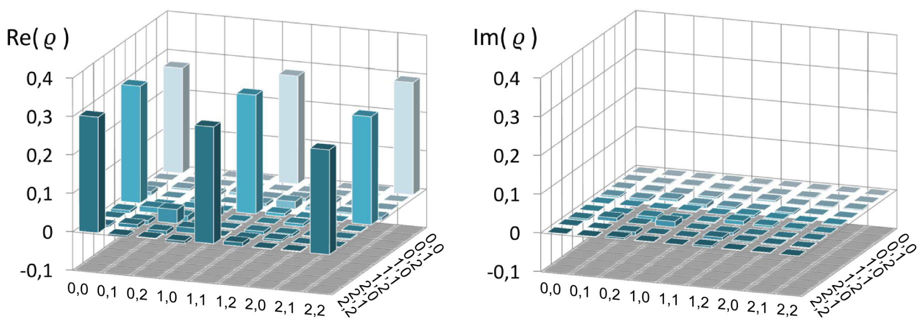

Figure 6.24: Noise subtracted corrected density matrix of maximum likelihood. The labels of the x-axis (y-axis) $[i, j]$ ($[i', j']$) form the element $|i, j\rangle \langle i', j'|$ of the density matrix ρ. $Im(\rho_{i,j}) < 0.02$.

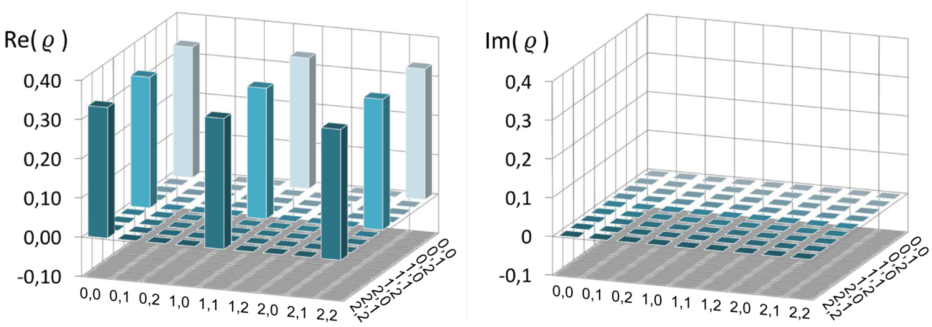

Figure 6.25: Theoretical perfect density matrix ρ. $Im(\rho_{i,j}) = 0$.

Comparing fig. 6.24 and fig. 6.25 the corrected fidelity reaches

$$F_C = (94.73 \pm 0.24)\%. \tag{6.12}$$

The Gell-Mann matrices are equivalent to the Pauli matrices acting on a 2×2 subspace. Therefore, they are not perfectly displayed by the Multiport. The assumption of perfect Gell-Mann matrices causes a reduction in fidelity and quality of the density matrix.

7 Outlook & Proposals

7.1 Further experiments using the qutrit setup

Using the entangled two qutrit source connected to the qutrit Multiports allows for a variety of different experiments without technical/experimental changes to the setup. An incomplete list is presented below:

- **CGLMP inequality**
  Collins, Gisin, Linden, Massar, and Popescu [2] have constructed classes of Bell inequalities (CGLMP inequality) for two entangled quNits of arbitrary dimension. The violation of such an inequality using 3×3 dimensional projection operations has not been observed so far. The inequality is strongly resistant to noise [2] and a violation would be a first step towards applications such as higher-dimensional quantum communication protocols. A first test revealed a violation of the CGLMP inequality of (2.3 ± 0.1) to be compared to the classic limit of 2 and the quantum physical prediction of $2\sqrt{2} \approx 2.83$. Thus, $(2.3 \pm 0.1)/2.83 \approx (81 \pm 4)\%$. No accidentals are subtracted. However, this was only a first test. The phase offsets (eq. 6.11) have been used on the qutrit side B to measure the other outputs on qutrit side A where only one trigger detector is used. Although this is valid within quantum physics for a true test three detectors should be used on both sides.

- **Realization of a SIC-POVM Measurement** From a theoretical perspective symmetrically informational complete (SIC) positive operator valued measurements (POVM) are of fundamental interest due to their generality and connection to MUBs. The current Multiport setup can be used to realize a SIC-POVM measurement [97]. SIC-POVMs are also of interest considering quantum state tomography and communication [98].

- **Stern-Gerlach Simulator**
  The optical analog of a spin-1 Stern-Gerlach device is possible with the current setup as has been proposed by Zukowski, Zeilinger, and Horne [1] along with the introduction of the Multiport.

- **Completeness proof of MUBs via perfect correlations**
  Via a certain entanglement witness a boundary of separability has been connected to the number of mutually unbiased bases for higher-dimensional entangled states as proofen in [99]. An experimental verification of this bound would verify the maximal number of MUBS in dimension N to be limited by $N + 1$.

- **Generalized Measurements**
  The Multiport can be used for realizing a general POVM measurement on a N dimensional system via the use of an additional $N + 1$-th mode. This is of use, for example, for unambiguous state discrimination [100, 101]. Moreover, the generality of this system will be of advantage here. The full parameter space of optimal quantum state discrimination with varying rates of inconclusive outcomes can be completely characterized with the current setup [102].

- **Kochen-Specker type experiment**
  An experimental setup for observing the Kochen-Specker paradox using the Multiport has already been proposed in the initial Multiport publication by Zukowski, Zeilinger, and Horne [1] and is realizable with the current setup. Additionally, a test of state-independent contextuality using entanglement qutrits has been proposed by Cabello, Amselem, Blanchfield, Bourennane, and Bengtsson [103], and Cabello [104]. Here, the bounds on the required visibility are demanding. However, slight variants of the proposed experiments might lead to more experimental friendly tests.

- The coherence length of the single photon could be increased by inserting filters of narrower bandwidth at the Multiport output before entering the triggering detector. Javier Chesterking [105] has started to implement 25GHz in-fiber filters. Initial tests revealed a similar quality of the setup in terms of SNR and count rates. Measurement of the visibility would now be of interest and might show an improvement. A longer coherence length results in higher tolerances towards alignment.

7.2 Direct next steps towards higher-dimensions

- All 4×4 Multiports have been characterized (see 8.1). Additionally, one 4×4 Multiport has already been optically packaged. Thus, only electrical contacts remain to be connected for a fully functioning 4×4 Multiport device. Using the automated programs the coverage of the unitary space could directly be tested leading the first integrated realization of the 4×4 general Multiport.

- Connecting the 4 ppLN crystals through 4 fiber phase shifters directly to the 4×4 Multiport while separating the photon pairs only directly before detection would be an easy experiment with low alignment demands. By applying the 50Hz signal to different phase shifters one would observe correlations of different amplitudes similar to what has been presented in fig. 6.12. This alone is sufficient for proving ququart correlations without stabilizing the signal. We have already implemented and tested a similar step for qubits in our lab (section 8.1).

- A commercial matrix switch could be utilized as a 8×8 general Multiport in an experiment similar to the last to bullet points. Again, the system for characterizing the Multiport is available.

- The 4×4 Multiport could be connected to the already existing entangled ququart source. Here, the loss and fiber length of the arms has to be readjusted meaning it is the most time consuming proposal of this list. A next generation PID has been designed and built. It includes the functions of the VB and has a faster PID loop. It stabilizes up to 8 channels required for stabilization of the ququart source. All control programs can handle any dimension of the system or are extendable.

7.3 Improving the Multiport - Prospects of integrated optics

The used Multiport was a one run prototype. A second generation of the Multiport would therefore greatly improve all specifications. The unnecessary loss of the PDC would be removed reducing a total loss of $\approx 6dB$ from the qutrit Multiport and thereby improving the visibility of the inner MZI by 2dB. Furthermore, the correct sizes of the beam splitter geometry would be chosen resulting in a better extinction ratio of every MZI and a better coverage of the unitary space. The global input and output phase shifters should be removed since they do not serve a purpose. In the following, a new design for the general Multiport will be presented which will be abbreviated "MS" due to its similarity to an existing device called Matrix Switch.

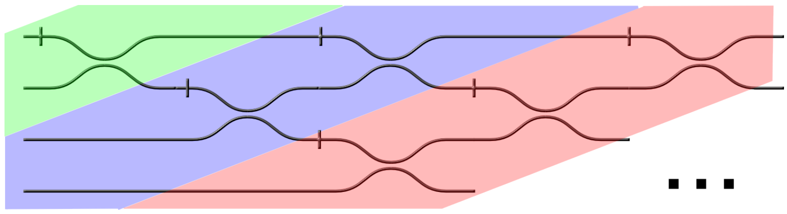

Figure 7.1: The Multiport with the basic SU(2) unit being a single beam splitters and phase shifter. Colors highlight the different stages S_n of the Multiport. The n-th stage consists of n SU(2) transformations.

As given in Eq.2.6 the N-dimensional MP following Recks et al. scheme [1] consists of $1 + 2 + 3 + ... + (N-1)$ $SU(2)$ elements. The Multiport therefore can be decomposed into $N-1$ stages (see fig. 7.1) with the $n-th$ stage S_n consisting of n $SU(2)$ transformations:

$$S_n = BS_{n-1,N} \cdot BS_{n-1,N-1} \cdots BS_{n-1,n},$$

with $BS_{i,j}$ being a MZI acting on modes (i,j) and a phase shifter at input mode i as a realization of a $SU(2)$ transformation. Up to output phases the full Multiport is the results of combining all $N-1$ stages:

$$U_{MP} = \prod_{i=1}^{N-1} S_i.$$

Each MZI ($BS_{i,j}$) consists of two inner phases φ_1 and φ_2. According to Eq.2.15 any reflectivity (depending on the phase difference Δ) and any global phase (proportional to the sum of the phases Σ) can be realized. Δ and Σ are linearly independent functions of the two inner phases φ_1 and φ_2. Therefore, any combination of reflectivity R and global phase φ can be realized using only the inner phases. As illustrated in fig. 7.2 the n-th stage S_n consists of $n-1$ MZIs with reflectivity R and $n-1$ input phase shifters $\varphi_{i,j}$.

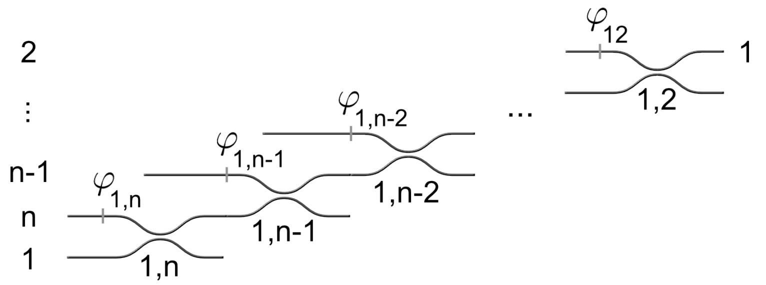

Figure 7.2: The n-th stage of a Multiport following M.Recks scheme of parametrization [1].

We will now consider the general case of a stage S_n inside of a general $N \times N$ Multiport as illustrated in fig. 7.2. The general idea of the new design is that all input phases $\varphi_{i,k}$ with $j \neq n$ of any stage S_n can be absorbed as the global phase produced by the sum Σ of the two inner phases of an MZI. Additionally a global phase along with output phases is introduced. The additional output phases will add to the input phases of the next stage S_{n+1}. As an example, the input phase $\varphi_{1,n-1}$ can be eliminated by the MZI$(1,n)$ producing an appropriate phase shift $\Sigma = -\varphi_{1,n-1}$ onto all modes. The next input phase therefore becomes $\varphi_{1,n-2} \rightarrow \varphi_{1,n-2} - \varphi_{1,n-1}$ which now can be eliminated by the next MZI acting onto modes $(1, n-2)$. The scheme is continued iteratively up to the last phase $\varphi_{1,2}$.

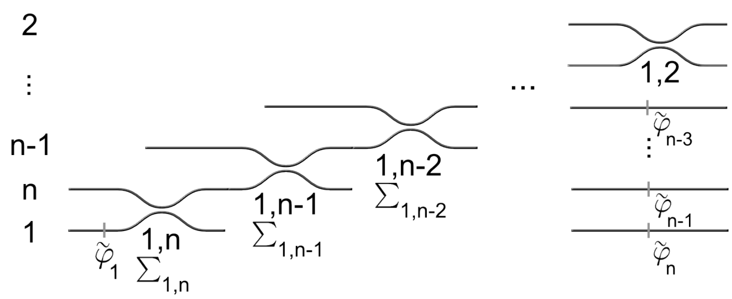

Figure 7.3

Using the following transformation the design shown in fig. 7.2 (right-hand side) becomes equivalent to the design shown in fig. 7.3 with the new parametrization (left-hand side):

$$\begin{aligned}
\varphi_G &= \quad \varphi_{1,2} \\
\tilde{\varphi_1} &= \quad -\varphi_{1,n} \\
\sum_{1,i} &= \quad -\varphi_{1,i-1} + \varphi_{1,i} \quad \forall i = n...(n-1) \\
\tilde{\varphi_i} &= \quad -\varphi_{1,2} + \varphi_{i-1} \quad \forall i = n...(n-3).
\end{aligned} \tag{7.1}$$

Here, φ_G is a global phase shift acting on all N inputs, $\tilde{\varphi_1}$ is a phase shift acting on the lowest mode only (which is always a Multiport input phase), $\sum_{1,i}$ are phase shifts produced by the MZIs, $\tilde{\varphi_i}$ are output phases of the current stage S_n. Therefore, considering a particular Multiport, starting at stage S_1 iteratively up to S_{n-1} every phase shifter outside of a MZI can be removed. The equivalence of the new design may easily be verified in any example of a particular

unitary transformation.
Thus, the scheme of Reck et al. [20] with one phase shifter and one beam splitter as the basic unit is equivalent to one MZI with phase shifts in each arm. This has a crucial effect on the integrated circuit realization: the total length of the circuit and the number of devices is reduced. Assuming the specification and sizes of the fundamental integrated devices given in subsection 4.4 the reduced length L and therefore reduction in insertion loss IL by the following factors:

$$L_{red} = 75\% \;,\; IL_{red} = (N-1)\,0.15dB.$$

However, the main advantage is the existence of an analog design of the circuit in Telecom industry: the (optical) matrix switch.

7.3.1 The Matrix Switch

The switching matrix is an N-input N-output $N \times N$ device used in telecommunication systems. It can be reconfigured to reroute signals from the inputs to any output equivalent to a Multiport setting with only 0% or 100% reflectivity. Indeed, the first integrated realizations of the matrix switch were based on a simple 2×2 MZI switching unit with its reflectivity changing via thermo-optical phase shifters. However, the requirement in telecommunication of little signal cross-talk has led to the success of different designs. Often the basic 2×2 switching unit is now composed out of more than one MZI in a way that increases the complexity but greatly improves the signal cross-talk (multi-stage cross-talk suppression). Hence, the new design cannot be used as a Multiport anymore. Still, the Multiport design is present in older generations of matrix switches. For example, Okuno, Kato, Nagase, Himeno, Ohmori, and Kawachi [106] presented a 8×8 matrix switch usable as a fully functioning general 8×8 Multiport. The particular design has in fact almost the same waveguide sizes and properties as the current Multiport. However, switching matrices have been highly optimized. As a result an optical insertion loss of the full device of only $7.3dB$ and an MZI extinction ratio of $> 30dB$ is achieved.
Modern devices (not usable as a Multiport) even reach 32×32 inputs/outputs a total path length of $0.60m$ and an insertion loss of $< 10dB$ [107] [108],[82]. At this point of optimization the claim that integrated optics is inherently of high loss does not hold anymore. The device is packaged and commercially available from a number of companies. However, although the device is more complex than the 32×32 Multiport it cannot be used as one anymore for the reasons mentioned above.
Therefore, I propose that for a next generation of $N \geq 5$ Multiports on should try to use the commercial (older generations of) switching matrices. Although, they mostly have become obsolete, the designs and prototypes certainly still exist. The switching matrices build in [106, 109, 110], for example, can be used as a general 8×8 Multiport with the new design proposed in the previous section. The devices presented by Kimmich and Oswald [111] and Okuno, Kato, Nagase, Himeno, Ohmori, and Kawachi [106] are equivalent to a 4×4 Bellport of special symmetry excluding the one inner phase.
Other parts of the current experiment also allow great for improvement towards a higher level of integration.

7.3.2 The non-linear crystals

The performance of the nonlinear crystals especially in terms of efficiency does not need improvement towards a setup of higher dimension. However, in the current experiment there are N separately packaged and controlled crystals. It is possible to combine those N crystals onto one crystal with N parallel waveguides. In fact, most crystals contain multiple differently poled parallel waveguides with different phase matching properties. Considering the low requirement and high tolerance on the produced down-conversion spectrum (due to the narrow 100GHz filtering), it seems highly possible to have multiple waveguides of same property on one crystal chip. [1]

7.3.3 Power splitter

There are multiple commercial, integrated, and packaged $1 \times N$ devices splitting a bump beam into N outputs. For fixed splitting ratios PLCs of up to $N = 128$ are available. Otherwise, any combination of cascaded beam splitters is sufficient.

7.3.4 Wavelength filtering and rerouting

Between the Multiports and the down-conversion crystals the single photons need to be split and filtered followed by rerouting. An integrated realization will not require any phase stabilization nor polarization alignment. Loss differences can be adjusted using the input pump beam splitting ratios. For wavelength filtering different integrated realizations are possible such as cascaded MZIs [112] or ring resonators [113]. A device splitting 4 inputs by their wavelength and routing it to the $2N$ outputs (called a router) is presented by Sherwood-droz, Wang, Chen, Lee, Bergman, and Lipson [114].
Generally, re-configurable optical add drop multiplexer (ROADM) realizations [115] are highly similar to what is required for the stage between crystals and Multiports. A ROADM demultiplexes a signal input followed by a mesh of switching devices for "adding" and/or "dropping" a number of wavelengths to a number of drop channels. Eventually, the signal is multiplexed again. For example, Takahashi, Watanabe, Goh, Sohma, and Takahashi [116] reported a ROADM covering 32 wavelengths on a $(24 \times 56)mm^2$ chip with an extinction ratio of $> 70dB$ and an average insertion loss of $0.76dB$. Another example of a 38.5GHz ROADM was presented by Sherwood-droz, Wang, Chen, Lee, Bergman, and Lipson [114]. Additionally, the filtering can also take place after the Multiports before detection, outside of the interferometric region.

7.3.5 Hybrid integration

Since there is a wide availability of different complex devices packaging of two integrated circuits (hybrid packaging) becomes of interest. Packaging between Silica circuits and circuits of highly electro-optic materials such as Lithium Niobate waveguides (12 parallel channel) is possible and has reached the market [117].
Our coupling setup allows coupling of two chips such as a matrix switch to another integrated structure and has been tested to do so. Fig. 7.4 shows an example of two chips containing a

[1] Pers. com. HCPhotonics Corp., F4, No. 2, Technology Rd. V, Hsinchu Science Park, Hsinchu 300, Taiwan

beam splitter and two phase shifters each coupled together to form a MZI. Standard single mode fibers are packaged to the chips.

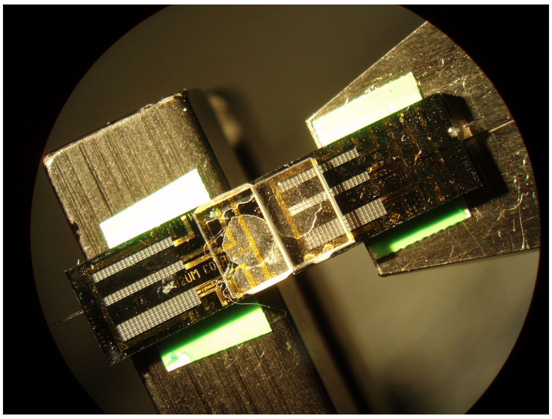

Figure 7.4: Two coupled and packaged PLC chips each containing a beam splitter and phase shifter and connected to optical fiber. Image taken by Sebastian Eckert.

7.3.6 The full setup

Ultimately, a setup where a $1 \times N$ PLC power splitter is coupled to an N-channel ppLN crystal followed by a $N \times 2N$ ROADM type PLC eventually routed into two $N \times N$ matrix switches is imaginable. Commercial fixed ratio PLC power splitter go up to 1×128 channel. An N channel ppLN crystal is not available and would be a custom product. Hybrid packaging between LN and Silica is an industry standard [117]. Although, a router required for the task does not exist, its complexity is comparable to common integrated ROADM devices. Matrix switches of new design go up to 32×32 which is more complex than a 32×32 Multiport in terms of number of devices [107]. The devices in [106, 109, 110] can be used as 8×8 Multiports. A short technical summary of most mentioned devices can also be found in [83].

8 Other

8.1 Supervised projects and theses

During the development of the experiment different students have worked on the setup itself or on side projects. All projects relate to the experiment and have been of importance for decisions along the path leading to the final setup and are shortly listed.

"Direct coupling of a fiber tip to KTP waveguides" by Ilse Krätschmer, project work

Nonlinear KTP crystal waveguides have been coupled to fibers and characterized. The purpose was to learn and gain experience with integrated periodically poled waveguides crystals for SPDC.

"To programme a Microcontroller and in-fiber piezo polarisation controller to monitor and maximize the polarisation dependant intensity of interference in a Mach-Zehnder interferometer" by David Keely ,Bachelor Thesis

Topic of David's thesis was to explore the possibility of using automated piezo controlled polarization controller for the in-fiber quNit source. An automated program was able to automatically optimize the visibility of a MZI. Automated polarization control would be a viable extension of the fiber source.

"Single Photon Detection Using Parametric Up-conversion" by Johannes Anderl, Bachelor Thesis

The aim was to test the feasibility of a detection scheme where the 1550nm photons are up-converted by a nonlinear process and detected in the visible light regime by high-performance detectors. A single photon conversion efficiency of 87% was reached. However, the used crystals turned out to create noise heavily reducing the signal to noise ratio.

"Characterization, coupling and packaging of PIC devices for quantum optical applications and experiments" by Sebastian Ecker, project thesis

Sebastian has characterized the ququart Multiport chips, improved the coupling and packaging setup and wrote a complete guide on how to couple and package integrated circuits using our setup.

"Building an integrated photonic platform for higher dimensional entangled quantum experiments" by Robert Polster, Master Thesis

Robert has developed the first and second generation PID along with the Visibility Board and has been involved in the development of the in-fiber qubit source and Multiport control. Most functions and electric designs can be found in his thesis.

"In-Fiber Multichannel Source of Path Entangled Photons at Telecom Wavelengths" by Juan Javier Sabines Chesterking, Master Thesis

The in-fiber entangled qubits source used in section 3 separates the photon pairs and routes each photon to a separate Multiport. Any local operation is then realized by the Multiport. The main idea in Javiers work [105] was to perform the splitting and filtering outside of the interferometric region, after the beam splitter / Multiport. The complexity of the problem of maximizing the indistinguishability of the down-conversion events is dramatically reduced. Except for the polarization there is no other degree of freedom which could reduce the visibility. In principle PM fibers could be used further simplifying the setup. A PID can be used to stabilize the phase of the entangled state. Furthermore, the crystals produce a quite broad down conversion spectrum. Thus, the produced entangled pairs of photons cover almost the full c-band. As a drawback, both photons enter the same beam splitter. Therefore, the same local transformation is performed on both photons.

9 Conclusion

We have successfully demonstrated a novel, fully fiber integrated source for path-encoded entangled photons. The source is compatible with on-chip path-encoding of integrated photonic circuits which is of great importance for utilizing the advantages of integrated circuits. The good scalability with respect to the dimensionality makes it a well suited design for complex experiments in higher dimensions. The source exhibits high brightness and very high fidelity of the produced entangled state. Moreover, there are no movable parts for alignment resulting in a high robustness and fully automated control. Additionally, the design allows for complete on-chip integration. All in-fiber components of the source have been tested for quantum optical operation with focus on quality reducing features such as the distinguishability. Furthermore, two devices for good estimation of the optical length of any in-fiber component have been developed.

We have realized the first integrated realization of the general Multiport. All components of the Multiport have been tested in detail. Methods of advanced characterization have been developed and were fully specified. An automated characterization and control system has been implemented. Rapid switching to any unitary transformations is possible. The scheme is readily extendable to higher-dimensions. Furthermore, we have introduced a method of estimating the most important property of the Multiport, the coverage of the unitary space, and presented a novel visualization of the property. The Multiport has been proven to exhibit an extremely high coverage of the unitary space meaning virtually any unitary transformation can be realized with the current setup. A complete coupling setup has been developed allowing for complete optical and electrical packaging of integrated devices. All 3×3 and 4×4 Multiports have been fully tested. The similarity of the basic Multiport circuit properties to the highly advanced state-of-the-art integrated matrix switches suggests the correct design choices have been made. Due to the similarity further iterations will therefore lead to even higher quality of the integrated circuit and offer great potential towards more complex circuits.

The dimension of the in-fiber source has been further extended to two entangled qutrits. Two 3×3 Multiports have been interfaced with the entangled qutrit source. A great number of different optical devices have been placed into phase-stable interferometric regions of the system with multiple modes interfering at different points. The high complexity is only possible due to the integrated approach and possibly hardly realizable otherwise. To my knowledge, one of the most advanced phase stabilization mechanism used in in-fiber quantum experiments was developed.

Furthermore, novel single photon detector prototypes have been tested and utilized in order to meet the high demands of the setup.

Using the complete setup different measurements have been performed. The state of all qubit subspaces has been reconstructed. Tomographic state reconstruction of the qutrit state revealed a high quality of the system. The high degree of control and quality of the system has enabled us to perform, a complete scan of the full qutrit-qutrit correlation space and was found to be in agreement with theoretical predictions. Furthermore, we experimentally observed and verified all predicted types of perfect correlations on the entangled qutrit system.

Regarding higher-dimensional realizations, the Multiport scheme has been further developed.

The new realization is similar to an optical matrix switch allowing the use of a standard, highly optimized product as a Multiport. The similarity has been unknown so far and offers great potential. All developed Multiport characterization schemes can be readily applied. In principle, the in-fiber source allows for a full on-chip integration and a possible path towards a complete integration of the current setup has been outlined. All tools for handling such a task have been developed.

Further experiments with the current setup have been proposed. Additionally, the compatibility of the in-fiber source and the Multiport with standard Telecom fiber networks at the Telecom wavelength will be of further interest from an applicational stand point (i.a. advanced quantum communication protocols in higher-dimensional Hilbert spaces).

The complete setup serves as a universal platform for a range of possible quantum optic experiments in a $3 \times 3 = 9$ dimensional Hilbert space. Due to the construction, containing no movable parts, virtually no alignment needs to be performed prior to an experiment. The three amplitudes of the entangled state can directly be set by the pump splitting ratios while all four phases (plus two global phases) of the entangled qutrit state are controlled by the PID controller. Each Multiport realizes any local unitary transformation meaning perfect control of all 8 transformation defining parameters per Multiport. Each qutrit enters a separate Multiport yielding a total of 16 parameters defining the complete two particle local unitary transformation. All parameters are under full control and can be freely set in order to perform a particular experiment. Other than defining the local unitary transformations and phase settings, little knowledge of the details of the system are required for the control of the experiment due to automatization.

We have thus successfully demonstrated a general platform for experiments in higher-dimensional Hilbert spaces opening up the possibility for a variety of novel future quantum experiments with the current platform and possible extensions to higher dimensions. The design is a viable approach towards higher-dimensional quantum systems and offers great potential towards a higher level of integration and complexity of higher-dimensional quantum systems.

References

[1] Marek Zukowski, Anton Zeilinger, and Michael Horne. Realizable higher-dimensional two-particle entanglements via multiport beam splitters. *Physical Review A*, 55(4):2564–2579, April 1997. ISSN 1050-2947. doi: 10.1103/PhysRevA.55.2564. URL `http://link.aps.org/doi/10.1103/PhysRevA.55.2564`.

[2] Daniel Collins, Nicolas Gisin, Noah Linden, Serge Massar, and Sandu Popescu. Bell inequalities for arbitrarily high-dimensional systems. *Physical review letters*, 88(4):040404, January 2002. ISSN 0031-9007. URL `http://www.ncbi.nlm.nih.gov/pubmed/11801097`.

[3] Anthony Laing, Valerio Scarani, and John G Rarity. Reference frame independent quantum key distribution. *arXiv:1003.1050v1*, 2010.

[4] Ingemar Bengtsson. Three ways to look at mutually unbiased bases. *arXiv:quant-ph/0610216v1*, 2006.

[5] Simon Gröblacher, Thomas Jennewein, Alipasha Vaziri, Gregor Weihs, and Anton Zeilinger. Experimental quantum cryptography with qutrits. *New Journal of Physics*, 8(5):75–75, May 2006. ISSN 1367-2630. doi: 10.1088/1367-2630/8/5/075. URL `http://iopscience.iop.org/1367-2630/8/5/075/fulltext/`.

[6] Christoph Spengler, Marcus Huber, Andreas Gabriel, and Beatrix C. Hiesmayr. Examining the dimensionality of genuine multipartite entanglement. *Quantum Information Processing*, 12(1):269–278, February 2012. ISSN 1570-0755. doi: 10.1007/s11128-012-0369-8. URL `http://arxiv.org/abs/1106.5664`.

[7] Jaewoo Joo, Peter Knight, Jeremy OBrien, and Terry Rudolph. One-way quantum computation with four-dimensional photonic qudits. *Physical Review A*, 76(5):052326, November 2007. ISSN 1050-2947. doi: 10.1103/PhysRevA.76.052326. URL `http://link.aps.org/doi/10.1103/PhysRevA.76.052326`.

[8] Marcus Huber and Julio I. de Vicente. Structure of Multidimensional Entanglement in Multipartite Systems. *Physical Review Letters*, 110(3):030501, January 2013. ISSN 0031-9007. doi: 10.1103/PhysRevLett.110.030501. URL `http://arxiv.org/abs/1210.6876`.

[9] Yuan Lim and Almut Beige. Multiphoton entanglement through a Bell-multiport beam splitter. *Physical Review A*, 71(6):062311, June 2005. ISSN 1050-2947. doi: 10.1103/PhysRevA.71.062311. URL `http://arxiv.org/abs/quant-ph/0406047`.

[10] Bao-Sen Shi and Akihisa Tomita. Schemes for generating W state of paths and W state of polarization photons. *arXv:quant-ph/0208170*, August 2002. URL `http://arxiv.org/abs/quant-ph/0208170`.

[11] Thomas Brougham, Vojtech Kost'ak, Igor Jex, Erika Andersson, and Tamas Kiss. Entanglement preparation using symmetric multiports. *arXiv:1010.2367*, October 2010. URL `http://arxiv.org/abs/1010.2367`.

[12] Yuan Liang Lim and Almut Beige. Multiphoton entanglement through a Bell multiport beam splitter. *arXiv:quant-ph/0406047v2*, 2008.

[13] Yoav Sagi. Scheme for generating Greenberger-Horne-Zeilinger-type states of n photons. *Physical Review A*, 68(4):1–4, 2003. ISSN 1050-2947. doi: 10.1103/PhysRevA.68.042320. URL `http://link.aps.org/doi/10.1103/PhysRevA.68.042320`.

[14] Dagomir Kaszlikowski and Marek Zukowski. Greenberger-Horne-Zeilinger paradoxes for N N-dimensional systems. *Physical Review A*, 66(4):1–6, 2002. ISSN 1050-2947. doi: 10.1103/PhysRevA.66.042107. URL `http://link.aps.org/doi/10.1103/PhysRevA.66.042107`.

[15] W Merkel, S Wölk, W P Schleich, I Sh Averbukh, B Girard, and G G Paulus. Factorization of numbers with Gauss sums: II. Suggestions for implementation with chirped laser pulses. *New Journal of Physics*, 13(10):103008, October 2011. ISSN 1367-2630. doi: 10.1088/1367-2630/13/10/103008. URL `http://iopscience.iop.org/1367-2630/13/10/103008/fulltext/`.

[16] S Zhang, C Lei, A Vourdas, and J Dunningham. Applications and implementation of Fourier multiport devices. *Journal of Physics B: Atomic, Molecular and Optical Physics*, 39(7):1625–1637, 2006. ISSN 0953-4075. doi: 10.1088/0953-4075/39/7/006.

[17] N. Cerf, C. Adami, and P. Kwiat. Optical simulation of quantum logic. *Physical Review A*, 57(3):R1477–R1480, March 1998. ISSN 1050-2947. doi: 10.1103/PhysRevA.57.R1477. URL `http://link.aps.org/doi/10.1103/PhysRevA.57.R1477`.

[18] Stefanie Barz, Gunther Cronenberg, Anton Zeilinger, and Philip Walther. Heralded generation of entangled photon pairs. *Nature Photonics*, 4(8):553–556, June 2010. ISSN 1749-4885. doi: 10.1038/nphoton.2010.156. URL `http://dx.doi.org/10.1038/nphoton.2010.156`.

[19] R. Prevedel, G. Cronenberg, M. Tame, M. Paternostro, P. Walther, M. Kim, and A. Zeilinger. Experimental Realization of Dicke States of up to Six Qubits for Multiparty Quantum Networking. *Physical Review Letters*, 103(2):020503, July 2009. ISSN 0031-9007. doi: 10.1103/PhysRevLett.103.020503. URL `http://link.aps.org/doi/10.1103/PhysRevLett.103.020503`.

[20] Michael Reck, Anton Zeilinger, Bernstein Herbert J., and Philip Bertani. Experimental realization of any discrete unitary operator. *Physical Review Letters*, 73:58–61, 1994.

[21] G Weihs, M Reck, H Weinfurter, and a Zeilinger. Two-photon interference in optical fiber multiports. *Physical review. A*, 54(1):893–897, July 1996. ISSN 1050-2947. URL `http://www.ncbi.nlm.nih.gov/pubmed/9913546`.

[22] G Weihs, M Reck, H Weinfurter, and A Zeilinger. All-fiber three-path Mach-Zehnder interferometer. *Opt. Lett*, 21(4):302–304, 1996.

[23] Christoph Schaeff, Robert Polster, Radek Lapkiewicz, Robert Fickler, Sven Ramelow, and Anton Zeilinger. Scalable fiber integrated source for higher-dimensional path-entangled photonic quNits. *Optics Express*, 20(15):16145, July 2012. ISSN 1094-4087. doi: 10.1364/OE.20.016145. URL `http://www.opticsinfobase.org/viewmedia.cfm?uri=oe-20-15-16145\&seq=0\&html=true`.

[24] Michael A. Nielsen and Isaac L. Chuang. *Quantum Computation and Quantum Information (Cambridge Series on Information and the Natural Sciences)*. Cambridge University Press, 2000. ISBN 0521635039.

[25] Dirk Bouwmeester, K Ekert, Artur, and Anton Zeilinger. *The Physics of Quantum Information: Quantum Cryptography, Quantum Teleportation, Quantum Computation*. Springer, 2000. ISBN 3540667784.

[26] Marlan O. Scully and M. Suhail Zubairy. *Quantum Optics*. Cambridge University Press, 1997. ISBN 0521435951.

[27] Bahaa E. A. Saleh and Malvin Carl Teich. *Fundamentals of Photonics (Wiley Series in Pure and Applied Optics)*. Wiley-Interscience, 2007. ISBN 0471358320.

[28] Artur Ekert. Entangled quantum systems and the Schmidt decomposition. *American Journal of Physics*, 63(5):415, May 1995. ISSN 00029505. doi: 10.1119/1.17904. URL `http://scitation.aip.org/content/aapt/journal/ajp/63/5/10.1119/1.17904`.

[29] R. T. Thew, A. G. White, and W. J. Munro. Qudit quantum-state tomography. *Physical Review A*, 66(1):012303, July 2002. ISSN 1050-2947. doi: 10.1103/PhysRevA.66.012303. URL `http://arxiv.org/abs/quant-ph/0201052`.

[30] Michael Reck. *Quantum Interferometry with Multiports: Entangled Photons in Optical Fibers*. PhD thesis, Leopold-Franzens Universität Innsbruck, 1996.

[31] Christoph Spengler, Marcus Huber, and Beatrix C. Hiesmayr. Composite parameterization and Haar measure for all unitary and special unitary groups. *arXiv*, quant-ph, March 2011. URL `http://arxiv.org/abs/1103.3408`.

[32] James W. Cooley, Peter A. W. Lewis, and Peter W. Welch. Historical notes on the fast Fourier transform. *Proc. IEEE*, 55(10):1675–1677, 1967.

[33] Päivi Törmä, Stig Stenholm, and Igor Jex. Hamiltonian theory of symmetric optical network transforms. *Physical Review A*, 52(6), 1995.

[34] P. Torma and I. Jex. Plate beam splitters and symmetric multiports. *Journal of Modern Optics*, 43(11):2403–2408, November 1996. ISSN 0950-0340. doi: 10.1080/09500349608232894.

[35] P Torma, I Jex, and S Stenholm. Beam splitter realizations of totally symmetric mode couplers. *Quantum optics*, 9:1–11, 1995.

[36] J.B. Altepeter, E.R. Jeffrey, and P.G. Kwiat. Photonic State Tomography. *Advances In Atomic, Molecular, and Optical Physics*, 52:105159, 2005. doi: 10.1016/S1049-250X(05)52003-2. URL `http://dx.doi.org/10.1016/S1049-250X(05)52003-2`.

[37] P Rungta, W J Munro, K Nemoto, P Deuar, G J Milburn, and C M Caves. Qudit Entanglement. In *Directions in Quantum Optics*, volume quant-ph, pages 1–14. 2000.

[38] Thomas Durt, Berthold-Georg Englert, Ingemar Bengtsson, and Karol Zyczkowski. On mutually unbiased bases. *arXiv:quant-ph/1004.3348*, April 2010. URL `http://arxiv.org/abs/1004.3348`.

[39] Philippe Raynal, Xin Lü, and Berthold-Georg Englert. Mutually unbiased bases in dimension six: The four most distant bases. *arXiv:quant-ph/1103.1025*, March 2011. URL `http://arxiv.org/abs/1103.1025`.

[40] Robert B. A. Adamson and Aephraim M. Steinberg. Improving Quantum State Estimation with Mutually Unbiased Bases. *arXiv:quant-ph/0808.0944*, August 2008. URL `http://arxiv.org/abs/0808.0944`.

[41] Ingemar Bengtsson, Wojciech Bruzda, Asa Ericsson, Jan-Ake Larsson, Wojciech Tadej, and Karol Zyczkowski. Mutually unbiased bases and Hadamard matrices of order six. *Journal of Mathematical Physics*, 48(5):052106, 2007. ISSN 00222488. doi: 10.1063/1.2716990. URL `http://link.aip.org/link/JMAPAQ/v48/i5/p052106/s1\&Agg=doi`.

[42] Stephen Brierley, Stefan Weigert, Uk-york Yo, and Ingemar Bengtsson. All Mutually Unbiased Bases in Dimensions Two to Five. *arXiv:quant-ph/0907.4097v1*, 2009.

[43] Maurice Robert Kibler. Quadratic discrete Fourier transform and mutually unbiased bases. *arXiv:quant-ph/1010.5964*, October 2010. URL `http://arxiv.org/abs/1010.5964`.

[44] H.O. Kunz. On the Equivalence Between One-Dimensional Discrete Walsh-Hadamard and Multidimensional Discrete Fourier Transforms. *IEEE Transactions on Computers*, C-28 (3):267–268, March 1979. ISSN 0018-9340. doi: 10.1109/TC.1979.1675334.

[45] B.J. FINO and V. Algazi. Unified Matrix Treatment of the Fast Walsh-Hadamard Transform. *IEEE Transactions on Computers*, C-25(11):1142–1146, November 1976. ISSN 0018-9340. doi: 10.1109/TC.1976.1674569. URL `http://ieeexplore.ieee.org/lpdocs/epic03/wrapper.htm?arnumber=1674569`.

[46] Oliver Kern, Kedar S Ranade, and Ulrich Seyfarth. Complete sets of cyclic mutually unbiased bases in even prime-power dimensions. *Journal of Physics A: Mathematical and Theoretical*, 43(27):275305, July 2010. ISSN 1751-8113. doi: 10.1088/1751-8113/43/27/275305. URL `http://iopscience.iop.org/1751-8121/43/27/275305`.

[47] H. F. Chau. Unconditionally Secure Quantum Key Distribution In Higher Dimensions. *arXiv:quant-ph/0212055*, December 2002. URL `http://arxiv.org/abs/quant-ph/0212055v2`.

[48] S. Tanzilli, H. De Riedmatten, W. Tittel, H. Zbinden, P. Baldi, M. De Micheli, D.B. Ostrowsky, and N. Gisin. Highly efficient photon-pair source using periodically poled lithium niobate waveguide. *Electronics Letters*, 37(1):26, January 2001. ISSN 00135194. doi: 10.1049/el:20010009. URL `http://ieeexplore.ieee.org/articleDetails.jsp?arnumber=894344`.

[49] Marco Fiorentino, Sean M. Spillane, Raymond G. Beausoleil, Tony D. Roberts, Philip Battle, and Mark W. Munro. Spontaneous parametric down-conversion in periodically poled KTP waveguides and bulk crystals. *Optics Express*, 15(12):7479, 2007. ISSN 1094-4087. doi: 10.1364/OE.15.007479. URL `http://www.opticsexpress.org/abstract.cfm?URI=oe-15-12-7479`.

[50] IDQuantique SA. Chemin de la Marbrerie, 3 1227 Carouge / Geneva Switzerland.

[51] Toshimitsu Musha, Jun-ichi Kamimura, and Masataka Nakazawa. Optical phase fluctuations thermally induced in a single-mode optical fiber. *Applied Optics*, 21(4), 1982.

[52] A Hati, C W Nelson, and D A Howe. Vibration Sensitivity of Optical Components : A Survey. In *Frequency Control and the European Frequency and Time Forum (FCS), 2011 Joint Conference of the IEEE International. IEEE, 2011*, pages 532–535. IEEE, National Institute of Standards and Technology, 2011.

[53] Robert Polster. Building an integrated photonic platform for higher dimensional entangled quantum experiments, Master Thesis, University of Vienna, 2011.

[54] John Clauser, Michael Horne, Abner Shimony, and Richard Holt. Proposed Experiment to Test Local Hidden-Variable Theories. *Physical Review Letters*, 23(15):880–884, October 1969. ISSN 0031-9007. doi: 10.1103/PhysRevLett.23.880. URL `http://adsabs.harvard.edu/abs/1969PhRvL..23..880C`.

[55] Daniel F. V. James, Paul G. Kwiat, William J. Munro, and Andrew G. White. Measurement of qubits. *Physical Review A*, 64(5):052312, October 2001. ISSN 1050-2947. doi: 10.1103/PhysRevA.64.052312.

[56] Serge Valette. Integrated Optics : The history and the future. In *ECOC*, pages 1–6, 1973.

[57] Alberto Politi, Jonathan C F Matthews, and Jeremy L O'Brien. Shor's quantum factoring algorithm on a photonic chip. *Science*, 325(5945):1221, September 2009. ISSN 1095-9203. doi: 10.1126/science.1173731. URL `http://www.sciencemag.org/content/325/5945/1221.abstract`.

[58] a. Peruzzo, M. Lobino, J. C. F. Matthews, N. Matsuda, A. Politi, K. Poulios, X.-Q. Zhou, Y. Lahini, N. Ismail, K. Worhoff, Y. Bromberg, Y. Silberberg, M. G. Thompson, and J. L. OBrien. Quantum Walks of Correlated Photons. *Science*, 329(5998):1500–1503, September 2010. ISSN 0036-8075. doi: 10.1126/science.1193515. URL `http://www.sciencemag.org/cgi/doi/10.1126/science.1193515`.

[59] Anthony Laing, Alberto Peruzzo, Alberto Politi, Maria Rodas Verde, Matthaeus Halder, Timothy C. Ralph, Mark G. Thompson, and Jeremy L. O'Brien. High-fidelity operation of quantum photonic circuits. *Applied Physics B*, 97(211109), April 2010. URL `http://arxiv.org/abs/1004.0326`.

[60] Alberto Peruzzo, Peter Shadbolt, Nicolas Brunner, Sandu Popescu, and Jeremy L O'Brien. A quantum delayed-choice experiment. *Science*, 338(6107):634–7, November 2012. ISSN 1095-9203. doi: 10.1126/science.1226719. URL `http://www.sciencemag.org/content/338/6107/634.abstract`.

[61] Jonathan C. F. Matthews, Alberto Politi, André Stefanov, and Jeremy L. O'Brien. Manipulation of multiphoton entanglement in waveguide quantum circuits. *Nature Photonics*, 3(6):346–350, May 2009. ISSN 1749-4885. doi: 10.1038/nphoton.2009.93. URL `http://dx.doi.org/10.1038/nphoton.2009.93`.

[62] P. J. Shadbolt, M. R. Verde, A. Peruzzo, A. Politi, A. Laing, M. Lobino, J. C. F. Matthews, M. G. Thompson, and J. L. O'Brien. Generating, manipulating and measuring entanglement and mixture with a reconfigurable photonic circuit. *Nature Photonics*, 6(1):45–49, December 2011. ISSN 1749-4885. doi: 10.1038/nphoton.2011.283. URL `http://dx.doi.org/10.1038/nphoton.2011.283`.

[63] Max Tillmann, Borivoje Dakić, René Heilmann, Stefan Nolte, Alexander Szameit, and Philip Walther. Experimental boson sampling. *Nature Photonics*, 7(7):540–544, May 2013. ISSN 1749-4885. doi: 10.1038/nphoton.2013.102. URL `http://dx.doi.org/10.1038/nphoton.2013.102`.

[64] Alexander Szameit and Stefan Nolte. Discrete optics in femtosecond-laser-written photonic structures. *Journal of Physics B: Atomic, Molecular and Optical Physics*, 43(16):163001, August 2010. ISSN 0953-4075. doi: 10.1088/0953-4075/43/16/163001. URL `http://iopscience.iop.org/0953-4075/43/16/163001`.

[65] Benjamin J. Metcalf, Nicholas Thomas-Peter, Justin B. Spring, Dmytro Kundys, Matthew A. Broome, Peter Humphreys, Xian-Min Jin, Marco Barbieri, W. Steven Kolthammer, James C. Gates, Brian J. Smith, Nathan K. Langford, Peter G. R. Smith, and Ian A. Walmsley. Multi-photon quantum interference in a multi-port integrated photonic device. *arXiv:quant-ph/1208.4575*, August 2012. URL `http://arxiv.org/abs/1208.4575`.

[66] Alexander Szameit, Felix Dreisow, Thomas Pertsch, Stefan Nolte, and Andreas Tünnermann. Control of directional evanescent coupling in fs laser written waveguides. *Optics Express*, 15(4):1579–1587, February 2007. ISSN 1094-4087. doi: 10.1364/OE.15.001579. URL `http://www.opticsinfobase.org/viewmedia.cfm?uri=oe-15-4-1579\&seq=0\&html=true`.

[67] Alberto Politi, Martin J Cryan, John G Rarity, Siyuan Yu, and Jeremy L O'Brien. Silica-on-silicon waveguide quantum circuits. *Science (New York, N.Y.)*, 320(5876):646–9, 2008.

ISSN 1095-9203. doi: 10.1126/science.1155441. URL `http://www.ncbi.nlm.nih.gov/pubmed/18369104`.

[68] Benjamin J Metcalf, Nicholas Thomas-Peter, Justin B Spring, Dmytro Kundys, Matthew A Broome, Peter C Humphreys, Xian-Min Jin, Marco Barbieri, W Steven Kolthammer, James C Gates, Brian J Smith, Nathan K Langford, Peter G R Smith, and Ian A Walmsley. Multiphoton quantum interference in a multiport integrated photonic device. *Nature communications*, 4:1356, January 2013. ISSN 2041-1723. doi: 10.1038/ncomms2349. URL `http://dx.doi.org/10.1038/ncomms2349`.

[69] Alberto Peruzzo, Anthony Laing, Alberto Politi, Terry Rudolph, and Jeremy L O'Brien. Multimode quantum interference of photons in multiport integrated devices. *Nature communications*, 2:224, January 2011. ISSN 2041-1723. doi: 10.1038/ncomms1228. URL `http://dx.doi.org/10.1038/ncomms1228`.

[70] Kevin K. Lee, Desmond R. Lim, Hsin-Chiao Luan, Anuradha Agarwal, James Foresi, and Lionel C. Kimerling. Effect of size and roughness on light transmission in a Si/SiO[sub 2] waveguide: Experiments and model. *Applied Physics Letters*, 77(11):1617, 2000. ISSN 00036951. doi: 10.1063/1.1308532. URL `http://link.aip.org/link/APPLAB/v77/i11/p1617/s1\&Agg=doi`.

[71] J. Merle Elson. Propagation in planar waveguides and the effects of wall roughness. *Optics Express*, 9(9):461, October 2001. ISSN 1094-4087. doi: 10.1364/OE.9.000461. URL `http://www.opticsexpress.org/abstract.cfm?URI=oe-9-9-461`.

[72] Shinji Mino, Hiroshi Yamazaki, and Takashi Goh. R & D of Optical Component Technologies Multilevel Optical Modulator integration Technology. Technical report, NTT, 2011.

[73] Ginés Lifante. *Integrated Photonics: Fundamentals*. John Wiley & Sons Ltd., 2003. ISBN 0470848685.

[74] A. Zhang, R.-Y.; Janiak, K.; Bach, H. -G; Kunkel, R.; Seeger, A.; Schubert, S.; Schell, M.; Matiss, A.; Umbach. Performance of InP-based 90 -hybrids QPSK receivers within C-Band. In *Compound Semiconductor Week (CSW/IPRM)*, pages 1–3. IEEE, 2011.

[75] Lorenzo Pavesi and David J Lockwood. *Silicon Photonics*, volume 94. Springer, 2004.

[76] G. T. Reed, G Mashanovich, F. Y. Gardes, and D. J. Thomson. Silicon optical modulators. *Nature Photonics*, 4(8):518–526, July 2010. ISSN 1749-4885. doi: 10.1038/nphoton.2010.179. URL `http://www.nature.com/doifinder/10.1038/nphoton.2010.179`.

[77] High-performance Ge-on si, Jurgen Michel, Jifeng Liu, and Lionel C Kimerling. High-performance Ge-on-Si photodetectors. *Nature Publishing Group*, 4(8):527–534, 2010. ISSN 1749-4885. doi: 10.1038/nphoton.2010.157. URL `http://dx.doi.org/10.1038/nphoton.2010.157`.

[78] Di Liang and John E Bowers. Recent progress in lasers on silicon. *Nature Publishing Group*, 4(8):511–517, 2010. ISSN 1749-4885. doi: 10.1038/nphoton.2010.167. URL http://dx.doi.org/10.1038/nphoton.2010.167.

[79] Mikko Harjanne, Markku Kapulainen, Timo Aalto, and Päivi Heimala. Sub- s Switching Time in Silicon-on-Insulator. *IEEE Photonics Technology Letters*, 16(9):2039–2041, 2004.

[80] Jared F Bauters, Martijn J R Heck, Demis John, Daoxin Dai, Ming-Chun Tien, Jonathon S Barton, Arne Leinse, René G Heideman, Daniel J Blumenthal, and John E Bowers. Ultra-low-loss high-aspect-ratio Si3N4 waveguides. *Optics express*, 19(4):3163–74, February 2011. ISSN 1094-4087. doi: 10.1364/OE.19.003163. URL http://www.opticsinfobase.org/viewmedia.cfm?uri=oe-19-4-3163\&seq=0\&html=true.

[81] T. Kominato, Y. Ohmori, H. Okazaki, and M. Yasu. Very low-loss GeO2-doped silica waveguides fabricated by flame hydrolysis deposition method. *Electronics Letters*, 26(5): 327, March 1990. ISSN 00135194. doi: 10.1049/el:19900215. URL http://ieeexplore.ieee.org/articleDetails.jsp?arnumber=82641.

[82] T. Shibata, M. Okuno, T. Goh, M. Yasu, M. Itoh, M. Ishii, Y. Hibino, A. Sugita, and A. Himeno. Silica-based 16 16 optical matrix switch module with integrated driving circuits. In *OFC 2001. Optical Fiber Communication Conference and Exhibit. Technical Digest Postconference Edition (IEEE Cat. 01CH37171)*, volume 1, pages WR1–1–3. Opt. Soc. America, 2001. ISBN 1-55752-655-9. doi: 10.1109/OFC.2001.928388. URL http://ieeexplore.ieee.org/lpdocs/epic03/wrapper.htm?arnumber=928388.

[83] Masayuki Okuno, Takashi Goh, and Shunichi Sohma. Recent Advances in Optical Switches Using Silica-based PLC Technology. *Ntt Technical Review*, 1(7), 2003.

[84] Sebastian Ecker. Characterization, coupling and packaging of PIC devices for quantum optical applications and experiments, Project Thesis, Institute for Quantum Optics and Quantum Information, 2012.

[85] Anthony Laing and Jeremy L. O'Brien. Super-stable tomography of any linear optical device. August 2012. URL http://arxiv.org/abs/1208.2868.

[86] Saleh Rahimi-Keshari, Matthew A Broome, Robert Fickler, Alessandro Fedrizzi, Timothy C Ralph, and Andrew G White. Direct characterization of linear-optical networks. *Optics express*, 21(11):13450–8, June 2013. ISSN 1094-4087. doi: 10.1364/OE.21.013450. URL http://www.opticsexpress.org/abstract.cfm?URI=oe-21-11-13450.

[87] S Cova, M Ghioni, a Lacaita, C Samori, and F Zappa. Avalanche photodiodes and quenching circuits for single-photon detection. *Applied optics*, 35(12):1956–76, April 1996. ISSN 0003-6935. URL http://www.ncbi.nlm.nih.gov/pubmed/21085320.

[88] T. Pearsall. GaInAs: A ternary semiconductor for photodetector applications. *IEEE Journal of Quantum Electronics*, 16(7):709–720, July 1980. ISSN 0018-9197. doi: 10.1109/JQE.1980.1070557. URL http://ieeexplore.ieee.org/lpdocs/epic03/wrapper.htm?arnumber=1070557.

[89] Zhizhong Yan, Deny R Hamel, Aimee K Heinrichs, Xudong Jiang, Mark A Itzler, and Thomas Jennewein. An ultra low noise telecom wavelength free running single photon detector using negative feedback avalanche diode. *The Review of scientific instruments*, 83(7):073105, July 2012. ISSN 1089-7623. doi: 10.1063/1.4732813. URL http://arxiv.org/abs/1201.2433.

[90] AIT Austrian Institute of Technology GmbH. Donau-City-Straße 1, 1220 Vienna, Austria.

[91] Chandra M Natarajan, Michael G Tanner, and Robert H Hadfield. Superconducting nanowire single-photon detectors: physics and applications. *Superconductor Science and Technology*, 25(6):063001, June 2012. ISSN 0953-2048. doi: 10.1088/0953-2048/25/6/063001. URL http://iopscience.iop.org/0953-2048/25/6/063001/article/.

[92] Adriana E. Lita, Aaron J. Miller, and Sae Woo Nam. Counting near-infrared single-photons with 95% efficiency. *Optics Express*, 16(5):3032, March 2008. ISSN 1094-4087. doi: 10.1364/OE.16.003032. URL http://www.opticsexpress.org/abstract.cfm?URI=oe-16-5-3032.

[93] B. E. Kardyna, Z. L. Yuan, and A. J. Shields. An avalanchephotodiode-based photon-number-resolving detector. *Nature Photonics*, 2(7):425–428, June 2008. ISSN 1749-4885. doi: 10.1038/nphoton.2008.101. URL http://arxiv.org/abs/0807.0330.

[94] Laser Components USA. 9 River Road Hudson, NH 03051 USA.

[95] Gerhard Humer, Andreas Poppe, Momtchil Peev, Martin Stierle, Sven Ramelow, Christoph Schäff, Anton Zeilinger, and Rupert Ursin. New free running, low noise 1550nm single photon detector for commercial applications. In *QCMC*, 2012.

[96] LaserComponents GmbH. CountQ: Photonen bis 1650 nm zählen, 2013. URL http://www.lasercomponents.com/de/news/count-q-photonen-bis-1650-nm-zaehlen/.

[97] Gelo Noel M. Tabia. Experimental scheme for qubit and qutrit symmetric informationally complete positive operator-valued measurements using multiport devices. *Physical Review A*, 86(6):062107, December 2012. ISSN 1050-2947. doi: 10.1103/PhysRevA.86.062107. URL http://link.aps.org/doi/10.1103/PhysRevA.86.062107.

[98] Christopher A. Fuchs and Masahide Sasaki. Squeezing Quantum Information through a Classical Channel: Measuring the ”Quantumness” of a Set of Quantum States. *arXiv:quant-ph/0302092*, February 2003. URL http://arxiv.org/abs/quant-ph/0302092.

[99] Christoph Spengler, Marcus Huber, Stephen Brierley, Theodor Adaktylos, and Beatrix C. Hiesmayr. Entanglement detection via mutually unbiased bases. *Physical Review A*, 86(2):022311, August 2012. ISSN 1050-2947. doi: 10.1103/PhysRevA.86.022311. URL http://link.aps.org/doi/10.1103/PhysRevA.86.022311.

[100] Masoud Mohseni, Aephraim Steinberg, and János Bergou. Optical Realization of Optimal Unambiguous Discrimination for Pure and Mixed Quantum States. *Physical Review Letters*, 93(20), November 2004. ISSN 0031-9007. doi: 10.1103/PhysRevLett.93.200403. URL `http://arxiv.org/abs/quant-ph/0401002`.

[101] János A. Bergou, Ulrike Futschik, and Edgar Feldman. Optimal Unambiguous Discrimination of Pure Quantum States. *Physical Review Letters*, 108(25):250502, June 2012. ISSN 0031-9007. doi: 10.1103/PhysRevLett.108.250502. URL `http://link.aps.org/doi/10.1103/PhysRevLett.108.250502`.

[102] E. Bagan, R. Muñoz Tapia, G. A. Olivares-Rentería, and J. A. Bergou. Optimal discrimination of quantum states with a fixed rate of inconclusive outcomes. *Physical Review A*, 86(4):040303, October 2012. ISSN 1050-2947. doi: 10.1103/PhysRevA.86.040303. URL `http://link.aps.org/doi/10.1103/PhysRevA.86.040303`.

[103] Adán Cabello, Elias Amselem, Kate Blanchfield, Mohamed Bourennane, and Ingemar Bengtsson. Proposed experiments of qutrit state-independent contextuality and two-qutrit contextuality-based nonlocality. *Physical Review A*, 85(3):032108, March 2012. ISSN 1050-2947. doi: 10.1103/PhysRevA.85.032108. URL `http://link.aps.org/doi/10.1103/PhysRevA.85.032108`.

[104] Adan Cabello. Proposal for revealing quantum nonlocality via local contextuality. *arXiv:quant-ph/0910.5507*, page 4, October 2009. doi: 10.1103/PhysRevLett.104.220401. URL `http://arxiv.org/abs/0910.5507`.

[105] Juan Javier Sabines Chesterking. In-Fiber Multichannel Source of Path Entangled Photons at Telecom Wavelengths, Master Thesis, Institute for Quantum Optics and Quantum Information, 2013.

[106] Masayuki Okuno, Kuniharu Kato, Ryo Nagase, Akira Himeno, Yasuji Ohmori, and Masao Kawachi. Silica-Based 8x8 Optical Matrix Switch Integrating New Switching Units with Large Fabrication Tolerance. *Lightwave*, 17(5):771–781, 1999.

[107] S. Sohma, T. Watanabe, N. Ooba, M. Itoh, T. Shibata, and H. Takahashi. Silica-based PLC Type 32 x 32 Optical Matrix Switch. In *2006 European Conference on Optical Communications*, pages 1–2. IEEE, September 2006. ISBN 978-2-912328-39-7. doi: 10.1109/ECOC.2006.4801113. URL `http://ieeexplore.ieee.org/articleDetails.jsp?arnumber=4801113`.

[108] T. Goh, M. Yasu, K. Hattori, A. Himeno, M. Okuno, and Y. Ohmori. Low loss and high extinction ratio strictly nonblocking 1616 thermooptic matrix switch on 6-in wafer using silica-based planar lightwave circuit technology. *Journal of Lightwave Technology*, 19(3):371–379, March 2001. ISSN 07338724. doi: 10.1109/50.918890. URL `http://ieeexplore.ieee.org/lpdocs/epic03/wrapper.htm?arnumber=918890`.

[109] Ryo Nagase. Silica-Based 8x8 Optical Matrix Switch Module with Hybrid Integrated Driving its System Application. *Journal of Lightwave Technology*, 12(9), 1994.

[110] Masayuki Okuno, Kuniharu Kato, Yasuji Ohmori, Masao Kawachi, Tohru Matsunaga, and I Introduction. Improved 8x8 Integrated Optical Matrix Switch Using Silica-Based Planar Lightwave Circuits. *Journal of Lightwave Technology*, 12(9):1597–1606, 1994.

[111] K Kimmich and M Oswald. Integrated Optical 4x4 star coupler on LiNb=3. *Electronics Letters*, 20:1058–1059, 1984.

[112] Qian Wang and Sailing He. Optimal design of planar wavelength circuits based on Mach-Zehnder Interferometers and their cascaded forms. *Journal of Lightwave Technology*, 23 (3):1284–1290, March 2005. ISSN 0733-8724. doi: 10.1109/JLT.2004.839985. URL `http://ieeexplore.ieee.org/lpdocs/epic03/wrapper.htm?arnumber=1417027`.

[113] Tymon Barwicz, Michael R Watts, Peter T Rakich, Luciano Socci, Erich P Ippen, Miloš A Popovic, Franz X Kärtner, and Henry I Smith. Multistage high-order microring-resonator adddrop lters. *Opt. Lett*, 31(17):2571–2573, 2006.

[114] Nicolás Sherwood-droz, Howard Wang, Long Chen, Benjamin G Lee, Keren Bergman, and Michal Lipson. Optical 4x4 hitless silicon router for optical Networks-on-Chip (NoC). *Opt. Express*, 16(20):1–3, 2008.

[115] B. Grek and K. Schmidt. Monolithically integrated 32 x four-channel client reconfigurable optical add/drop multiplexer on planar lightwave circuit. *IEEE Photonics Technology Letters*, 15(10):1413–1415, October 2003. ISSN 1041-1135. doi: 10.1109/LPT.2003.818220. URL `http://ieeexplore.ieee.org/lpdocs/epic03/wrapper.htm?arnumber=1232975`.

[116] Hiroshi Takahashi, Toshio Watanabe, Takashi Goh, Shunichi Sohma, and Tetsuo Takahashi. PLC Optical Switch that Enhances the Optical Communication Network. *Ntt Technical Review*, 3(7):17–21, 2005.

[117] Shinji Mino, Hiroshi Yamazaki, Takashi Goh, and Takashi Yamada. Multilevel Optical Modulator Utilizing PLC-LiNbO3 Hybrid-integration Technology. Technical report, NTT, 2011. URL `https://www.ntt-review.jp/archive/ntttechnical.php?contents=ntr201103fa8.html`.

10 Appendix

10.1 LabView Code Documentation

A list of the most important programs (LabView VIs) for the control of the experiment is presented. Additionally, most vi's also contain in-code documentation and comments.

- **StartUp_CTRL.vi**
  Connects to the FPGA via LAN. Has to be running constantly during operation.

- **Temp ctrl.vi**
  An Interface for controlling the two temperature PIDs of both Multiports. Constantly measures both temperatures and actively stabilizes the signal to the defined setpoints (SP1 and SP2). No function is accessing this vi. Has to be operated independently.

- **ScanAmp.vi**
  Automatically measures the amplitude of each crystal by changing the Multiport such that only on of the crystals is routed to the detectors. Returns coincidences, accidentials, SNR of each crystal. Precision, of course, depends on the quality of the Multiport setting. Perfect transmission/ reflection of the MZIs on the MP is assumed. This program is used for alignment of the splitting ratios of the pump.

Multiport Phase shifter / Pin control

Handles the control of the phase shifters on the Multiport chips.

- **Pin2Voltage.vi**
  Handles the connection between Pin Name (e.g. a3,B5,b2) and corresponding array of the array variable.

- **SgPinControl.vi**
  Uses SetAllPins and Pin2Voltage

- **SetAllPins.vi**
  Sets every pin of the FPGA to the value (value).

- **File2MP.vi**
  Programs the FPGA such that the Multiport displays what is defined in the file. Uses SgPinControl.

- **File2MP_ListSelector_Separatempsvi.vi**
  The lowest VI for control of single pins on the Multiport. Directly accesses the network variable PWM_Array.

Characterize the Multiport

Programs used to find the neccessary duty cycle values for a certain setting of the Multiport.

- **Find_Max_Min.vi**
  Top-level vi. Interface for characterizing the MP. Uses Find_Max_MultiRn.vi, Find_Min_MultiRn.vi,

Find_IntValMultRUN.vi, FIND MAXIMUM Int in PWM Range.vi. Define PIN and Reflectivity and the program automatically starts measuring and gives the resulting maximum, minimum and reflectivity values.

- **Find_Max_MultiRn.viFind_Min_MultiRn.vi**
  Uses FIND MAXIMUM Int in PWM Range.vi multiple times with increasing precision narrowing down the PWM frequency for Maximum / Minimum transmission of a MZI on the MP.

- **Find_IntVal_MultRUN.vi**
  Uses Find_IntVal_SgRUN.vi multiple times with increasing precision narrowing down the PWM frequency for obtaining a certain Reflectivity.

- **Find MAXMIN Int in PWM Range / Find_IntVal_SgRUN.vi**
  Lowest level vi.

- **Find_all.vi**
  Higest level vi. Takes a list of PINs and Reflectivities and uses Find_Max_Min.vi to find the corresponding reflectivity for each PIN, outputs the results and saves them to a specified file.

PID Control

- **PID Get Data.vi**
  Returns a stream of numbers corresponding to different variables of the PID.

- **StabONOFF.vi**
  Turns the defined channel ch# on/off.

- **SCAN.vi**
  The PID scans the channel ch# and returns the Max/Min of the signal. This takes approx. 1s to 2s.

- **PID READ.vi**
  Reads any incoming message coming from the PID serial communication.

- **50Hz**
  Turns the 50Hz signal at channel ch# on/off.

Visibility Board

Functions of the visibility board (VB).

- **VisiCTRL.vi**
  A simple interface to manually control the VB via serial commands.

- **0123OFF.vi**
  Turns channel ch# off and no signal from the fW detectors (PD) will arrive at the PID.

- **0123Fit.vi**
  Optimizes the visibility of channel ch# appearing at the PID by amplifying and offsetting the signals of the fW detectos.

- **5AllOff.vi**
  Turns off amplification and offsets of all channels.

- Other serial commands ADC up ADC down, DAQ up down

In principle the VB accepts only integer numbers 0...255. The above functions are simply sending integers via the connection. Below in Tab.10.1 all commands are summarized. Using the VisiCTRL.vi one could also send those custom commands.

Command	Function
005	All OFF
00X	Optimize ("Fit") channel $X = 0, 1, 2, 3$
01X	Turn off channel $X = 0, 1, 2, 3$
1XY	Manually amplify channel $X = 0, 1, 2, 3$ by increasing the amplification in steps of -10 ($Y = 0$), -1($Y = 1$), +1 ($Y = 2$), +10($Y = 3$).
1XY	Manually subtract a voltage from channel $X = 0, 1, 2, 3$ in steps of -10 ($Y = 6$), -1($Y = 7$), +1 ($Y = 8$), +10($Y = 9$).

Table 10.1: Commands accepted by the VB.

Advanced Functions

- **PID&VB Man CTRL**
  A interface for manually controlling the PID and VB via serial communication.

- **RunFringe Set FJump&SP.vi**
  Sets the stabilizing PID to a new value of (F#,P%). Performes fringe jumps if necessary. With consecutive calls to this vi the next set of (F# and P%) will be read from a file named FSCAN.txt. This file defines the number and position of each data point to be used for the characterization fringe. If all data points of FSCAN.txt have been used the End? Variable will turn true.

- **Fit Fringe Run.vi**
  Fits the input data (the coincidence signal, F#,P%,) opbtained by running RunFringe Set FJump&SP.vi and returns the best fit values.

- **Find Fringe# and Phase FROM ANGLE.vi**
  Uses the best fit parameters to find the (F#,P%) values for a desired input phase pair and outputs the results. If OffSetAdd is true and one phase value will lie too close to a maximum, the vi will add global phase offsets to all channels and therefore move the phase away from the maximum. If beta is true the vi will use both phases of both channels. Otherwise, the other channel (beta) will not be changed and stay constant. Sym(T)/Anti(F) defines

if the two phases currently used have the same sign or not. For example, if alpha = pi and beta = pi and the configuration is antisymmetric, then alpha+beta=0.

- **SetFandPfromAlphaAndBeta.vi**
  Takes the result(s) from Find Fringe# and Phase FROM ANGLE.vi and sets the phase accoardingly using the PID.

- **PID&VB ManCTRL InnerAutomLoop.vi**
  Uses Fit Fringe Run.vi, Find Fringe# and Phase FROM ANGLE.vi and SetFandPfromAlphaAndBeta.vi. Given a certain pair of modes and desired phases this program automatically characterizes the phases, calculates the corresponding phase values from the fit, sets the phase to the desired one and measures for a certain Meas Time and returns the results. The detectors coincidence delay window as well as the position for measuring the accidentials can be defined here.

- **PID Seq.vi**
  Uses PID&VB ManCTRL InnerAutomLoop.vi. The high-level vi. Measures a list of defined phases (alpha0, beta0, alpha1, beta1) and returns the results to a file. Basically everything is done automatically. Also, everything is written to the corresponding folder in a formatted way. These files can be read later by the data analyzing programs.

IDQuantique Detector Control

- RemoteControlODQ_V2.vi
  Remotely controls all IDQuantique detectors via serial communication.

- RemoteControlODQ_V2_delay scan.vi
  Remotely controls all IDQuantique detectors via serial communication and allows for automatic scanning of a specified or the whole delay interval (025ns) in specified steps (min 0.1ns) for finding the optimal detector delay.

Other trivial functions

- **CCLogic, CC_Init.vi**
  A labview program controlling the coincidence logic.

- **VB beforeAfter OSZI.vi**
  Reads and displays the stream of data coming from an ADC via USB measuring the voltage before and after the VB. It therefore displays the output signal of the fW detectors and the (optimized) signal output of the VB going into the PID.

- **SetPWMFreq.vi / ReadoutPWMFreq.vi**
  Writes the network variable PWMFrequency. This variable defines the PWM frequency and therefore the resolution.

- **ArrayPWMViewer.vi**
  Views the network variable array.

- **RunThroughfileList_MeasCC_ACC.vi**
  Takes two list of files containing MP settings placed in different filters. Every setting of Multiport 1 (in Folder 1) is measured with every setting of Multiport 2 (Folder 2) for an defined integration time.

10.2 Code Example

An example of how to use the above functions to run a full measurement is shown in fig. 10.2, fig. 10.3 and fig. 10.4. Starting at Fig. 10.2 the program opens connections to the PID, VB and FPGA. Then, in this example both Multiports are set to the Bellport setting. Note, that the order in which functions are executed is not uniquely defined in some cases if no logical connection exists. Therefore, the order must be defined actively in the code. For simplicity this is not done in fig.10.2, fig.10.3 and fig.10.4. After initialization and connections are made the program goes on to fig.10.3. Channel 0 and 3 are scanned by the PID and stabilization is turned on. The 50Hz signal is applied to the outer MZI and characterization is performed and the inner MZI is set to the phase defined in the variable "Inner Angles". Then the the VB optimizes the visibility of channel 1 and 2 of the outer MZI, the PID Scans them and starts stabilization. Now the outer MZI is characterized followed by the measurement of the phases defined in the variable "Outer Angles". Eventually, all connections are closed, and the Multiport phases are turned off. All results are written to a Folder defined in the cluster variable "Write" and can be accessed by the analyzation programs. The detection setting (QE, dead-time, etc...) and integration times are defined in the cluster variable "Detection". Fig.10.1 shows a screen shot of the interface. All important parameter can be defined.

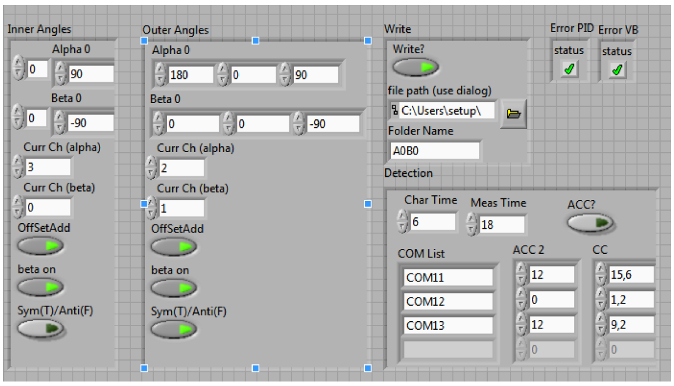

Figure 10.1: Screenshot of the control program

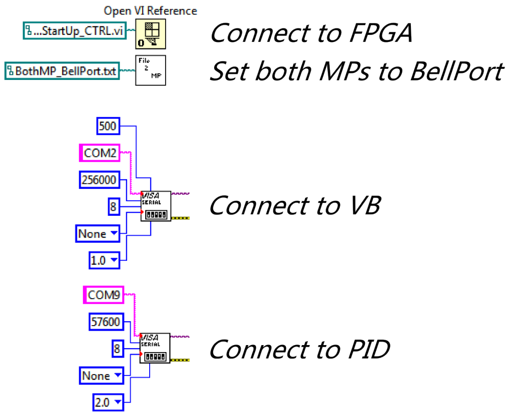

Figure 10.2: Initialization, program step 1 of 3.

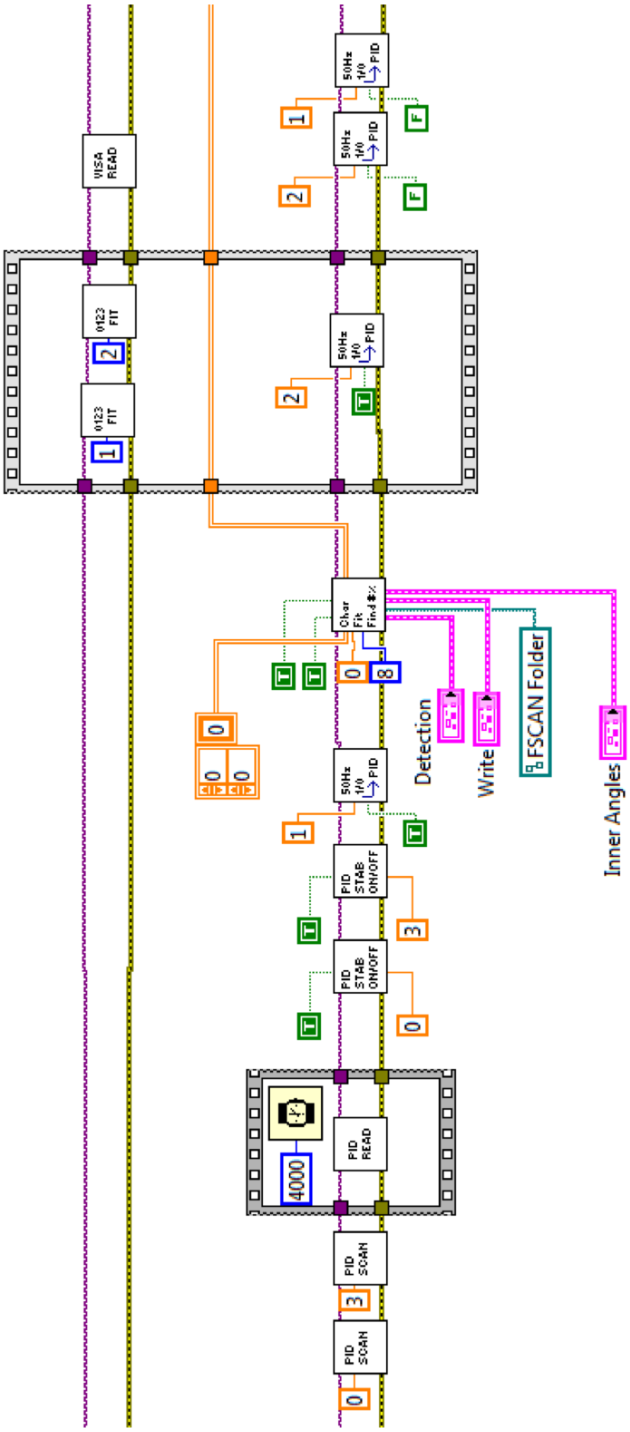

Figure 10.3: Program flow from left (bottom) to right (top). Step 2 of 3.

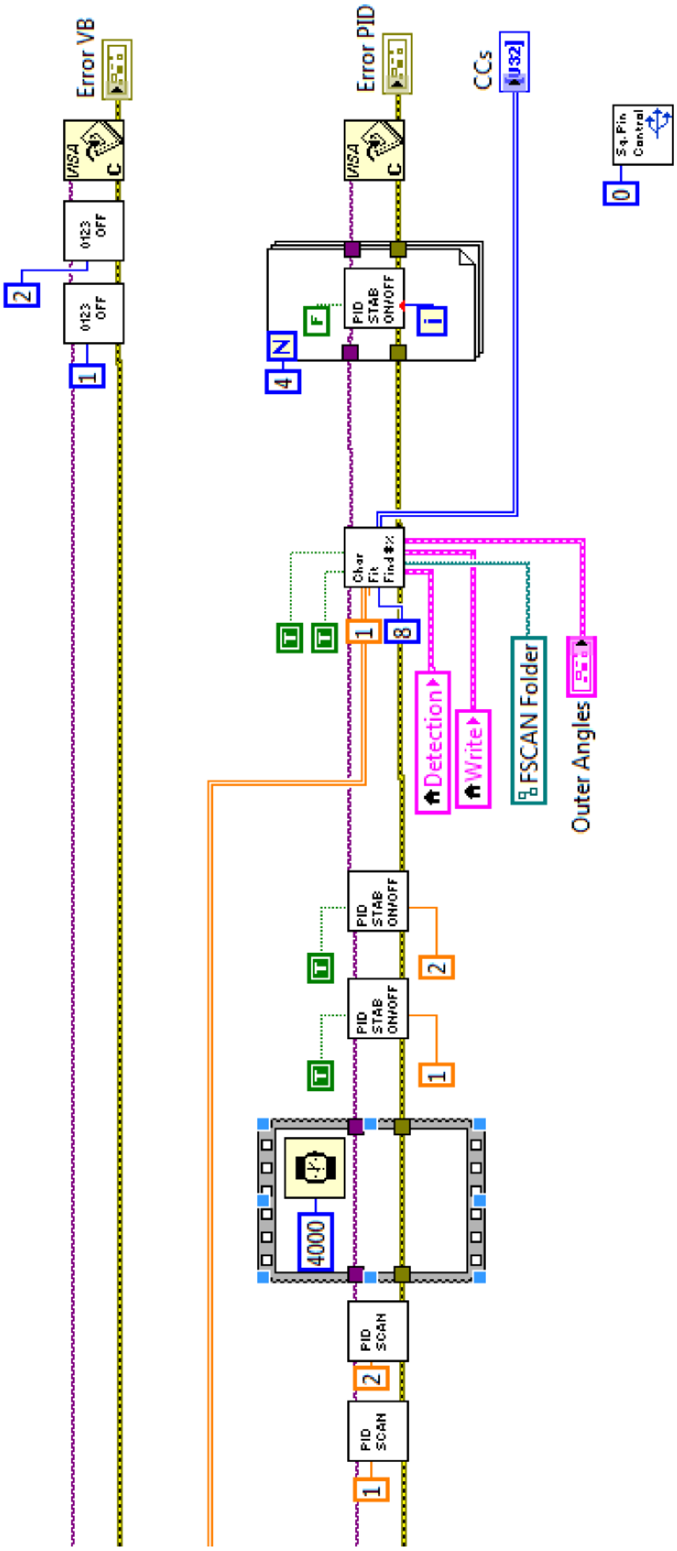

Figure 10.4: Program flow from left (bottom) to right (top). Step 3 of 3.

10.3 Curriculum Vitae

Curriculum Vitae

Christoph Schäff

Name	Jan Christoph Schäff
Nationality	German
Date of birth	June 15th 1984
Place of birth	Erlangen, Germany
Marital status	single
Language	German (mother tongue) English (fluent), Latinum
Permanent Address	Leipziger Str. 13 D-34359, Reinhardshagen, Germany
Phone	+49 151 15 70 65 09
eMail	ChristophSchaeff@gmx.de

06/2009- 10/2010	Member of the European Research Training Network Engineering, manipulation and characterization of Quantum Systems of matter and light (EMALI)
06/2009	Member of Vienna Doctoral Program on Complex Quantum Systems (CoQuS)
06/2009	Begin of PhD studies in the Group of Prof. Dr. Anton Zeilinger Institute for Quantum Optics and Quantum Information University of Vienna, Vienna, Austria
12/2008	Awarded M.A. in Physics from the University of Texas at Austin
09/2007- 05/2008	Foreign exchange scholarship from the German Academic Exchange Service (DAAD)
06/2007	Research member of the Atom Optics Group under Prof. Mark G. Raizen Center for Nonlinear Dynamics University of Texas at Austin, Tx, USA
10/2006	"Vordiplom" in Physics Julius-Maximilians University of Wuerzburg, Germany
10/2004	Study of physics Julius-Maximilians University of Wuerzburg, Germany Minor fields of study: chemistry, business studies
06/2004	High school graduation (Abitur) Grotefend-Gymnasium, Hann.Muenden, Germany

10.4 Thesis Summary (German)

Die Entwicklung einer Platform zur Ermöglichung von Experimenten an höherdimensionalen verschränkten Quantensystemen wird beschrieben. Statt der Realisierung eines spezifischen Experiments wird ein allgemeiner Ansatz mit einem möglichst hohem Grad an Universalität gewählt. Entscheidende Schritte hin zum kompletten Aufbau werden aufgezeigt. Die Entwicklung einer vollständig in Glassfasern integrierten Quelle zur Erzeugung höherdimensionaler wegverschränkter Zustände wird beschrieben. Des Weiteren wird die Entwicklung eines so genannten Multiports zur experimentellen Realisierung jeder beliebigen unitären Transformation von jeglicher Dimension aufgezeigt. Die Vorteile integrierter Lichtwellenleiter wurden zur Realisierung des Multiports verwendet. Methoden zur Charakterisierung und Bestimmung der Qualität des so realisierten Multiports wurden entwickelt und angewendet. Die notwendigen Schritte hin zu einem vollständigen System bestehend aus Quelle und Multiport werden dargelegt, die entwickelten automatisierten Kontrollmechanismen werden beschrieben. Dies führt zu einem universellen auf verschiedene Arten einsetzbaren System. Die Einstellung bestimmter Parameter erlaubt eine direkte Kontrolle der erzeugten verschränkten Zustand, sowie die Einstellung beliebiger lokaler unitären Transformationen. U.a. wurden ein verschränktes qutrit-qutrit $3 \times 3 = 9$ dimensionales System erzeugt, sowie der komplette verschränkte Korrelationsraum vermessen. Übereinstimmung mit den theoretischen Erwartungen konnte festgestellt werden. Weitere mögliche Schritte hin zu höherdimensionalen Systemen werden beschrieben u.a. wurde eine neue Realisierung des Multiports entwickelt, welche aufgrund ihrer Ähnlichkeit zu existierenden Systemen eine vielversprechende Möglichkeit zukünftiger Quantensysteme darstellt.